# Functionalized Multilayer Thin Films for Protection against Acutely Toxic Agents

by

Kevin Christopher Krogman

B.S., University of Louisville (2003)
M.Eng., University of Louisville (2004)

Submitted to the Department of Chemical Engineering
in partial fulfillment of the requirements for the degree of:

Doctor of Philosophy

at the

MASSACHUSETTS INSTITUTE OF TECHNOLOGY

June 2009

Signature of Author..................................
Kevin Christopher Krogman
Department of Chemical Engineering
May 5, 2009

Certified By............................................
Paula T. Hammond
Professor of Chemical Engineering
Thesis Supervisor

Accepted By...........................................................
William M. Deen
Professor of Chemical Engineering
Chairman, Committee for Graduate Students

# Functionalized Multilayer Thin Films for Protection against Acutely Toxic Agents

by

Kevin Christopher Krogman

Submitted to the Department of Chemical Engineering
on May 5, 2009, in partial fulfillment of the
requirements for the degree of
Doctor of Philosophy

## Abstract

The recently developed practice of spraying polyelectrolyte solutions onto a substrate in order to construct thin films via the Layer-by-Layer (LbL) technique has been further investigated and extended. In this process a fully automated system capable of depositing thin polymer films from atomized mists of solutions containing species of complementary functionality has been created. The versatility of the spray-assisted LbL (Spray-LbL) technology is demonstrated by depositing both weak and strong polyelectrolyte films, hydrogen bonded films, dendritic compounds and nanoparticles, broadening its range of future applications. This platform technology is then applied to generate three novel electrostatically assembled coatings for protection against a range of acutely toxic chemicals, including several chemical warfare agents and toxic industrial compounds.

First, Spray-LbL is used to deposit colloidally stable titanium dioxide nanoparticles versus several traditional synthetic polycations. The resulting coatings are mechanically stable and offer selective protection when the wearer is exposed to UV radiation (e.g. sunlight); whereas the inherent water transmissive nature of the multilayers allows for much greater water vapor transport rates as compared to an inert rubber barrier material. Second, the physics of sprayed deposition are investigated to generate metal-ion doped polymeric coatings which are shown to be effective treatments for air filtration, functionalizing existing filters with the ability to strongly bind toxic industrial compounds such as ammonia or cyanide gases, as well as chemical warfare agent simulants such as chloroethyl ethyl sulfide. Finally, the Spray-LbL technique is used to asymmetrically functionalize electrospun materials with multiple coatings. By simply varying the flow rate of charged species passing through an electrospun material during Spray-LbL deposition, individual fibers within the matrix can be conformally functionalized for ultra-high surface area catalysis, or bridged to form a networked sublayer with complimentary properties. Exemplified here by the creation of selectively-reactive gas purification membranes, the myriad applications of this technology also include self-cleaning fabrics, water purification, and protein functionalization of scaffolds for tissue engineering.

Thesis Supervisor: Paula T. Hammond

Title: Bayer Chair Professor of Chemical Engineering and Executive Officer

*For my grandfather, Harry G. Truman,*

*the consummate engineer*

# Acknowledgements

*Science is the belief in the ignorance of the experts.*
-Richard Feynman

*The person who is waiting for something to turn up*
*might start with their shirt sleeves.*
-Garth Henrichs

As you'll see from the following list, it takes a lot of people to make me look like a good engineer. On the surface the development of a finished body of research like this is, by necessity, an individual accomplishment. At a deeper, perhaps even more significant, level the development of me as an engineer has been a team effort. Allow me to introduce the team…

I'd like to first thank my advisor, Professor Paula Hammond, and committee members, Professor Bill Deen and Professor Greg Rutledge. I feel very fortunate to have had the opportunity to work under the watchful eyes of such a distinguished group. I'd also like to thank my wife Rachel, my team's captain and support group, without whose constant vote of confidence I would not have even set out on such a challenging path.

I would like to draw attention to two fellow researchers in particular who have played distinct roles in my progress. Nicole Zacharia, my mentor for the first two years of my time here, and Joe Lowery, whose contributions were crucial to the research discussed in Chapter 4. I am grateful as well to Mara Macdonald and Anita Shukla, who have supported the concept of Spray-LbL and encouraged its acceptance into the world of Layer-by-Layer. I would be remiss if I did not also acknowledge the support of several Hammond group members over the years as well, including Nathan Ashcraft, Ryan Waletzko, Kris Stokes, Kris Wood, and Amanda Engler.

Experimentally I would like to acknowledge and thank Dr. Jodie Lutkenhaus (for ESEM work shown in Chapter 1), Dr. Piljin Yoo (for AFM work in Chapter 1), Dr. Jung Ah Lee (for XPS in Chapter 3), Dr. Erik Allen (for molecular dynamics simulations in Ch. 3), and Dr. Phil Gibson and Dr. Heidi Schreuder-Gibson of the Natick Soldier Systems Center (for water permeation tests in Chapter 4 and countless discussions and advice). You can imagine how difficult it is to work with chemicals of this nature in a busy lab setting, and I would like to thank ISN lab management both past (Cathy Byrne) and present (Amy Tatem) for their faith in my ability not to accidentally gas the facility. Without their patience and oversight, this research would never have left the starting gate. I was also incredibly fortunate to be able to work with three undergraduate researchers, Stacey Schroeder of Michigan State University, Doris Grillo of MIT, and Kate Lyon of

Clemson University, whose fresh perspective and energy always proved to come at the ideal time in a long and often tedious process. Evidence of their hard work can be seen throughout this thesis, and I thank each of them for their time and effort.

Finally, I thank my parents and grandparents, particularly my grandfather, who gave me an interest in how things worked from a very young age. Most importantly, they have taught me the value of an honest day's work, and to never shrink from a challenge.

From the bottom of my heart, thank you all.

This work made use of the Shared Experimental Facilities at MIT's Center for Materials Science and Engineering, supported in part by the MRSEC program of the National Science Foundation under award number DMR 02-13282. It was financially supported by the U.S. Army through the Institute for Soldier Nanotechnologies, under contract DAAD-19-02-D-0002 with the U.S. Army Research Office. The content does not necessarily reflect the position of the government, and no official endorsement should be inferred.

# Table of Contents

# List of Figures

# List of Tables

# Introduction

## The Layer-by-Layer Technique

The Layer-by-Layer (LbL) electrostatic deposition technique can quite generally be described as the serial exposure of an innately charged substrate to alternating solutions of species exhibiting a complementary functionality. While the technique has enjoyed a significant increase in exposure during recent years, its roots can be traced back to the self-assembled monolayer work pioneered by Langmuir[1] and Blodgett[2] in the first half of the 20th century to deposit one or more monolayers of organic molecules on glass by exploiting favorable interfacial interactions. The first application of electrostatic alternation to deposit multilayer films, however, did not occur until the 1960s when Iler demonstrated the sequential deposition of two alternately charged metal-oxide particles from solution.[3] With the observation in the 1970's that polyelectrolytes could also be adsorbed to glass by electrostatic interactions[4], the door was opened for wide-spread future developments. In the late 1980's Decher and co-workers first introduced the concept of sequential electrostatic deposition using polyelectrolytes[5,6]. The application of polyelectrolytes, or molecules that carry more than one charge, is crucial to the LbL technique because it allows for charge reversal on the surface. Charge reversal provides self-limiting regulation to the process, as adsorbed molecules build up a repulsive layer restricting further growth, and prepares the surface for the next adsorption step in the process. As a result pioneering work was conducted in the 1990s by Rubner[7,8], Lvov[9], Tsukruk[10], Fendler[11,12], Schlenoff[13], Caruso[14] and others[15,16] evolving and developing the LbL field as we know it today.

As mentioned previously, the LbL technique is applicable to any two multivalent species exhibiting a complementary functionality. While this functionality is typically chosen to be the electrostatic interaction between two oppositely charged ions, LbL assembly has also been demonstrated using molecules which can undergo hydrogen-bonding.[17] LbL electrostatic assembly has been used to create films from solutions of flexible polyelectrolytes[7] and dendrimers[10], rigid nanoparticles[12], and even biological proteins[9]. It is the incredible flexibility and versatility of the technique which has allowed LbL to find wide-spread applications in fields such as electrochemistry[18], biological engineering[19], nanoparticle surface functionalization[14,20,21], optical coatings[22], and many more[23]. Initially proposed for the work presented here as a means to incorporate large amounts of amine-containing compounds into an ultrathin film for nucleophilic substitution reactions with mustard agents[24], the Layer-by-Layer technique has proven extremely valuable as a route to introduce multiple reactive functionalities into a single uniform coating held together by these amine-containing polymers.

## Application to Chemical Protection

Chemical warfare agents (CWAs) can be broadly classified into three categories based on route of entry and toxicity in the body[25]; (1) Nerve agents, such as Sarin, Tabun, Soman or VX, (2) Blister/vessicants, such as sulfur and nitrogen mustard, or Lewisite, and (3) choking agents, such as phosgene or chlorine. Nerve agents are by far the most toxic of the three categories, and function principally as cholinesterase inhibitors. Once introduced into the body via inhalation, skin/eye contact, or ingestion, nerve agents inhibit the ability of the acetylcholinesterase enzyme (AChE) to degrade the neurotransmitter acetylcholine (Ach). Nerve agents are easily produced and readily available. Their synthesis is relatively simple and inexpensive, and they are able to cause morbidity and mortality at extremely low doses. Blister/vesicants are aerosolized by bomb or shell blast, after which they vaporize slowly thereby demonstrating longer persistence times. Able to alkylate DNA, contributing to cellular damage and dermal blister formation, this category of CWAs make potentially effective terrorist weapons. Sulfur mustard, for example, is widely available, with over a dozen countries harboring known stockpiles, and is easy to manufacture. Of further importance to the chemical-protective community, there is no known antidote for sulfur mustard exposure. Choking agents attack lung tissue, but in the years since World War I have been treated more as nuisance chemicals, producing mainly irritant symptoms. Toxic Industrial Compounds (TICs) can logically be added as a fourth category to incorporate all acutely toxic chemicals. TICs have received increased military interest and concern over the ease with which they can be obtained and deployed. Of the 4,000 high production TICs, only 2100 are volume regulated in the United States, more than 1700 of which were recently categorized as priority concerns by the US Center for Health Promotion and Preventive Medicine. Compared to the 34 internationally recognized CWAs, this presents a daunting task in chemical-protection.

Whether acutely toxic chemicals are employed to induce casualties or fear, the most debilitating side effect may be to force opposing troops to wear full protective equipment, thus degrading fighting efficiency. Any progress to enhance efficiency in chemical-protective measures while preserving or increasing user comfort is of utmost utility to the military and HAZ-MAT first responders expected to function in the presence of these compounds. In recent years, efforts to decontaminate and detoxify compromised materials during post-treatment or eliminate stockpiled agents have escalated[26-28], but point-of-use chemical protective measures continue to rely on bulky, uncomfortable suits containing layers of porous carbon.[29] The LbL technique of creating thin films allows us to nano-engineer the contents and architecture of ultra-thin, yet uniform, coatings to prevent the passage of acutely toxic chemicals while allowing water vapor through.

In the work presented here the LbL technique will be applied to toxic chemical protection in a variety of ways. First, a variation on the traditional LbL technique will be described to facilitate the deposition of LbL coatings onto large areas of cotton textile for soldiers' uniforms, and conformally onto micro-porous materials for highly effective air filtration[30]. This technique will then be used to apply three novel chem-protective strategies including a photocatalytically active coating capable of degrading blister/vesicant agents using ambient sunlight[31], a metal-ion doped polymeric coating capable of selectively binding toxic industrial compounds and blister-vessicants[32], and a nano-engineered, asymmetrically functionalized composite capable of restricting mass transfer of toxic agents to facilitate photocatalytic degradation while promoting water vapor transport[33].

# 1. The Spray-assisted Layer-by-Layer Technique

## Abstract

The recently developed practice of spraying polyelectrolyte solutions onto a substrate in order to construct thin films via the Layer-by-Layer technique has been further investigated and extended. Here we describe a fully automated system capable of depositing thin polymer films from atomized mists of solutions containing species of complementary functionality. Film growth is shown to be similar to conventional "dipped" LbL assembly, while the reported technology allows us to realize upwards of 25-fold decreases in process times. Furthermore, complete automation removes human interaction and the possibility of operator induced nonuniformities. We demonstrate the versatility of the Spray-LbL technology by depositing both weak and strong polyelectrolyte films, hydrogen bonded films, dendritic compounds and nanoparticles, broadening its range of future applications. Finally, we show Spray-LbL technology can be used to uniformly coat an otherwise hydrophobic substrate from aqueous solutions. ESEM images indicate that the atomization process produces a conformal coating of individual nanofibers within the substrate, dramatically changing the hydrophilicity of the macroscopic surface. Such an automated system is easily converted to an array of nozzle banks, and could find application in the rapid, uniform coating of large areas of textile materials.

## 1.1 Introduction

Over the past two decades, the technique of polymer thin film deposition known as "Layer-by-Layer" has proven its versatility in creating very uniform films of precisely controllable thickness even on the nanometer length scale.[5] This process is commonly used to assemble films of oppositely charged polyelectrolytes, but other functionalities such as hydrogen bonding can also be the driving force for film assembly. Typically this deposition process involves the submersion of a substrate having an inherent surface charge into a series of liquid solutions of alternately charged species. Each submersion causes nearby polyions to adsorb rapidly to the oppositely charged surface, establishing a concentration gradient between the surface and the bulk solution. More distant macromolecules, sometimes more then 500 kDa in molecular weight, must then diffuse across this gradient to reach the surface. While this self-assembly mechanism is able to produce extremely uniform films as thin as one nanometer per polycation/polyanion cycle, due to the diffusive time scale it is not uncommon for a twenty five layer pair film to require more than twelve hours to complete, and thus is typically carried out by a computer controlled slide-stainer.[34]

Furthermore, as LbL is typically based on an electrostatic phenomenon, the degree of ionization of each polyelectrolyte in solution, determined by solution pH[7] or ionic strength[35-37], has a profound effect on the strength of interaction felt with the surface and in turn the thickness of the adsorbed layer.[38] In the case of an absorbent substrate such as fabric, the cyclic nature of the dipping process can lead to carryover from the rinse baths to the proceeding polyelectrolyte solutions inducing an unacceptable change in solution pH. In an effort to eliminate rinse water contamination, robotic modifications have been made to dipping systems[39], unfortunately the user is still confronted with process times on the order of days if high bilayer films are desired. This presents an unacceptable constraint if this technology is to evolve into industrial applications.

As one possible solution, modifications have been proposed to eliminate the diffusion time inherent to the traditional LbL process, and convectively spray the polymer solutions toward the substrate.[40] Several groups have reported using homemade 'spray-paint can' assemblies to deposit LbL systems,[40-42] and have deposited films in 60 s per layer that are of comparable quality to those developed at a rate of 25 minutes per layer via the dipping method.[41] This drastic decrease in process time can be attributed to the means of mass transfer of the polyelectrolyte from the bulk solution to the substrate surface, making this a valuable advancement in the LbL field. Atomization during the process may also reduce agglomeration in solutions of nanoparticles broadening the range of materials which can be electrostatically deposited. Unfortunately the scope of compatible solutions and substrates applicable to this spraying technology has gone relatively unexplored.

The purpose of the research described in this chapter was to develop an automated apparatus capable of spray depositing LbL films of several well understood polyelectrolyte systems in order to compare the uniformity and physical properties of the sprayed films with that of conventional dipped films, and to investigate the implications of the two techniques on the structure of low-bilayer films. Upon demonstration that the system could create films of comparable quality, the technology was extended to deposit hydrogen bonded films, dendritic compounds and colloidal nanoparticles. Finally the spray-LbL technology was used to conformally coat a hydrophobic textile material from aqueous solutions of polyelectrolytes, demonstrating a novel application of this developing technology.

## 1.2 Experimental

### 1.2.1 Materials

Poly(sodium 4-styrene sulfonate) (SPS, MW = 1,000,000), poly(dimethyldiallylammonium chloride) (PDAC, MW = 100,000, and sodium chloride were purchased from Aldrich. Poly(ethylene imine) (LPEI, MW = 25,000), poly(acrylic acid) (PAA, MW = 20,000), and polyethylene oxide (PEO, MW = 100,000) were purchased from Polysciences. Poly(amido amine) dendrimer (PAMAM G4, $NH_2$ surface, 22 wt% in methanol) was purchased from Dendritech. Polymer solutions were made using DI water at a concentration of 20 mmol with respect to the repeat unit, and adjusted to the required pH using HCl or NaOH. The ionic strength of the PDAC and SPS solutions was 0.1 mol NaCl. The hydrogen bonded nature of the PEO/PAA films requires careful attention to the pH of both solutions which must not vary more than 0.05 from the desired value. Spray-LbL tests were conducted on three and four inch diameter silicon wafers (Silicon Quest International), while dipped LbL tests were conducted on similar wafers which had been broken into 1cm by 5cm pieces. All silicon was cleaned with methanol and Milli-Q water, followed by five minutes of oxygen plasma etching (Harrick PCD 32G) to clean and hydroxylate the surface, although it has since been found that plasma etching is not necessary to achieve uniform coatings via sprayed deposition. 10

cm diameter Tyvek swatches were cut from unused laboratory coats (VWR) and were used as received.

### 1.2.2 Deposition

Dipped film assembly was automated with a Carl Zeiss HMS DS-50 slide stainer. The silicon substrates were first exposed to the polycation solution for 10 min. followed by three rinse steps in Milli-Q water for a total of 2 minutes. For the PAMAM/PAA and LPEI/PAA depositions the Milli-Q water was titrated to pH 4.0 using hydrochloric acid, otherwise the Milli-Q water was used at its default pH. The substrate was then exposed to the corresponding polyanion solution and rinsed similarly. The cycle was repeated for the required number of layer pairs requiring approximately 11.5 hours to complete a 25 layer pair film. Sprayed films were deposited using the automated spray system shown in Figure 1 from identical solutions and rinse pH values. All solutions were delivered by ultra high purity Argon (AirGas) regulated to 50 psi. The polycation was sprayed for 3 seconds and allowed to drain for 17 sec. before spraying with water for 10 sec. After a 10 second draining period the polyanion was sprayed and rinsed similarly. The cycle was then repeated for the desired number of layer pairs resulting in a 33 minute process to deposit a 25 layer pair film.

### 1.2.3 Analysis

Thickness measurements for growth curves were performed on a Woolam XLS-100 Spectroscopic Ellipsometer, and checked using a Tencor P10 profilometer with a stylus tip force of 6 mg. ESEM analysis was performed on a FEI/Phillips XL30 FEG ESEM at operating pressures between 0.9 and 1.5 mbar with a spot size of 3.0 μm. Atomic Force Microscopy was conducted using a Digital Instruments Dimension 3100 in tapping mode at an amplitude set point of 0.8 V under dry conditions. Height and phase images were taken at scanning rates of approximately 1.5 Hz. Contact angle measurements were performed by the standard sessile drop technique on an Advanced Surface Technology (AST) device. The contact angles presented in this paper are advancing contact water angles, and were made by moving the substrate vertically until contact was made between a water drop on the tip of a syringe and the sample. The subsequent addition of a small amount of water to the water drop on the surface produced the static advancing angle with the surface in a few seconds.

## 1.3 Results and Discussion

### 1.3.1 Automated System

The automated spray system shown schematically as well as graphically in Figure 1 consists of three identical solenoid valves, each supplied with a constant head of fluid from either of two polyelectrolyte vessels or a rinse water vessel. Spray is then controlled by sequentially closing and opening the solenoid valves with a logic relay capable of 10 ms accuracy in response time. The logic relay is programmable using standard ladder logic which is common to the Programmable Logic Controller (PLC) field. A sample ladder diagram for the deposition of a typical LbL film has been written using the ZelioSoft program available from Schneider Electric and included in the Appendix for reference. Fluids then pass through atomizing nozzles which are each equipped with a prefilter, impact the vertically oriented substrate which is mounted on a sliding post to allow larger substrates to be placed further from the nozzle bank, and fall into a collection pan in the base of the sprayer. To avoid drip patterns in the cascading film, the substrate is also rotated at 10 RPM. However, the reader should note that this speed is far too low to impart any centrifugal force to the liquid on the substrate. As all three nozzles are co-aligned to cover a common circular target the rotation is simply to minimize the effects of gravity as well as any irregularities in the pattern developed by the nozzles. Finally, to avoid contamination, all plumbing, including valve bodies, was constructed of poly(propylene).

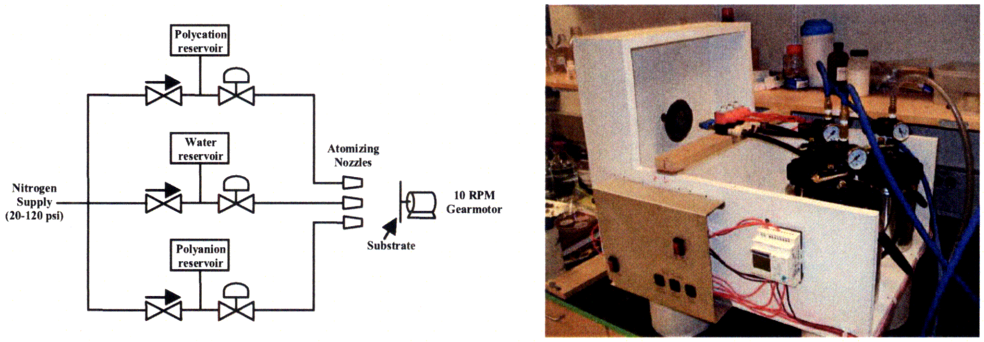

**Figure 1. Automated spray system**

(a) Schematic and (b) graphical representation of the automated Spray-LbL system on which this research was conducted.

### 1.3.2 Traditional Polyelectrolytes

For initial tests of the apparatus, (SPS/PDAC) films, both strong polyelectrolytes, and (PAMAM/PAA) films, both weak polyelectrolytes, were constructed. PAMAM was specifically selected to test the capabilities of spraying a dendritic macromolecule as well. The growth trend of $(SPS/PDAC)_n$ films constructed by dipping as well as by spraying can be seen in Figure 2(a), and demonstrate that the linear rate of growth developed by traditional dipped methods can be reproduced by the automated technology. However, noteworthy differences in the initial growth regime were observed. It is common in solution based LbL deposition to observe an initial non-linear growth regime, which typically lasts through the first three to five layer pairs[5,43,44] at which point a steady-state, linear growth phase is reached. This initial regime is generally explained by roughness or uneven charge distribution of the substrate, and as a result substantial growth does not appear to commence until several cycle repetitions have been completed.[45]

This phenomenon can be clearly seen in the growth trend of the dipped $(PDAC/SPS)_n$ films, which appear to begin growing steadily by the time the process has completed 5 cycles, but not in the sprayed films. Inspection of the substrate surface by AFM after the first application of polycation and polyanion via both the spray and the traditional dipped methods reveals the cause. In Figure 2(c), the dipping process appears to have initiated formed uneven 'island growth' on the substrate surface, leading to partial coverage during the initial growth regime. Alternatively, during the spraying process polyelectrolyte is atomized and introduced uniformly and simultaneously to the entire substrate, before quickly draining away. Thus the polymer chains are kinetically pinned to the point of contact with the substrate, whereas during dipping the chains arrive at the substrate surface much more slowly via diffusion, and have the freedom to complex with microscopic regions of higher charge density on the surface. The resulting film, shown in Figure 2(b), immediately exhibits uniform growth rates, eliminating the introductory growth period. This suggests that the spray method is preferable for creating ultra thin (less than 5 bilayer pairs) uniform layers of strong polyelectrolytes.

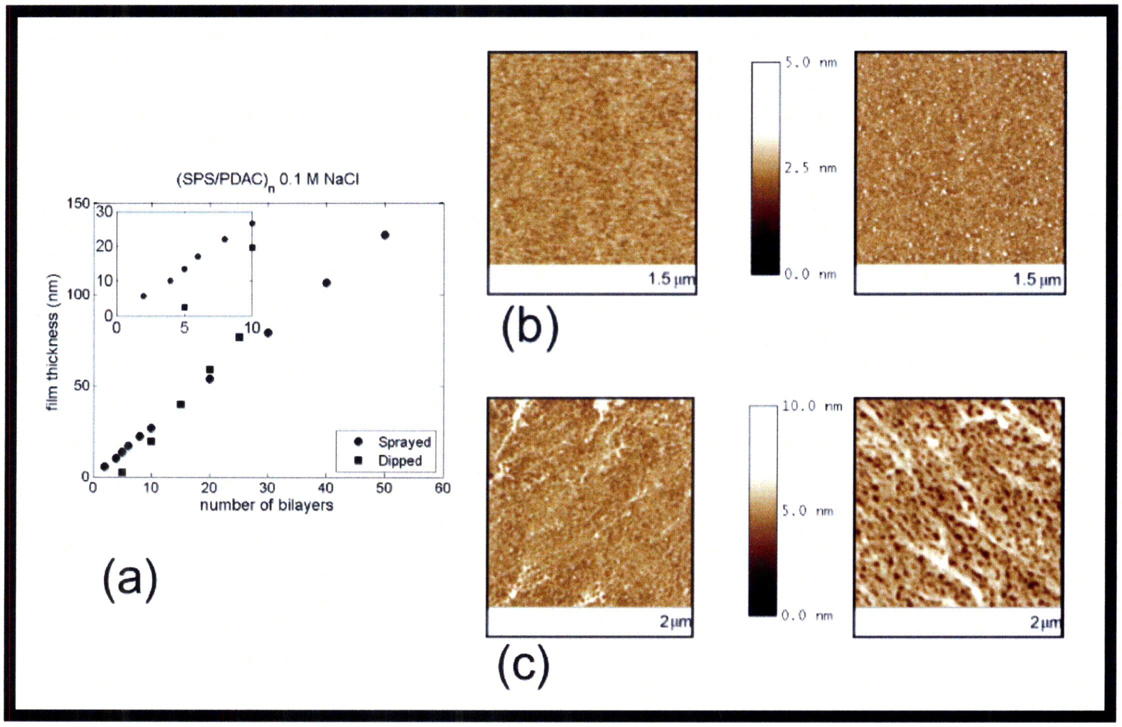

**Figure 2. Introductory growth of strong polyelectrolyte system**

**(a)** Correlation of total film thickness to layer pair number for the (SPS/PDAC)$_n$ system, both by spray deposition and dipping. Thickness was evaluated using ellipsometry and checked using profilometry. Reported values are averages taken from several data points on a silicon wafer and vary by less than ± 2 nm. Both dipped and sprayed films exhibit linear growth rates above 5 layer pairs, but the <u>sprayed</u> films have no initial non-linear growth regime. **(b)** AFM height images of sprayed (SPS/PDAC)$_n$ (i) 0.5 layer pair; PDAC surface and (ii) 1.0 layer pair; SPS surface. Coverage is thin but uniform. **(c)**

AFM height images of dipped (SPS/PDAC)n (i) 0.5 layer pair and (ii) 1.0 layer pair. Initially, “islands” form on the silicon substrate.

Similarly, the growth trends of both dipped and sprayed films containing $(PAMAM/PAA)_n$ assembled at pH 4 can be seen in Figure 3(a). In this case an introductory non-linear growth period is observed using either deposition method. Interactions of the weak polyelectrolyte PAA are more complicated[46,47], while the branched geometry and the Van der Waals forces between the interiors of the PAMAM molecules tend to cause them to aggregate on a weakly charged surface thus minimizing the kinetic pinning effect seen in the previous system of strong polyelectrolytes. AFM height images in Figure 4 of (b) the first layer pair of sprayed PAMAM/PAA and of (c) dipped PAMAM/PAA show similar topologies. Figures (b)-i and (c)-i indicate that in both cases the initial PAMAM layer deposits in aggregates of dendrimers. These aggregates are smaller in the sprayed case, again most likely because of atomization immediately prior to exposure to the substrate. The surface after the first exposure to PAA in both cases shows more complete coverage. Spraying therefore can be used to create a denser, albeit still incomplete, monolayer of dendrimer aggregates.

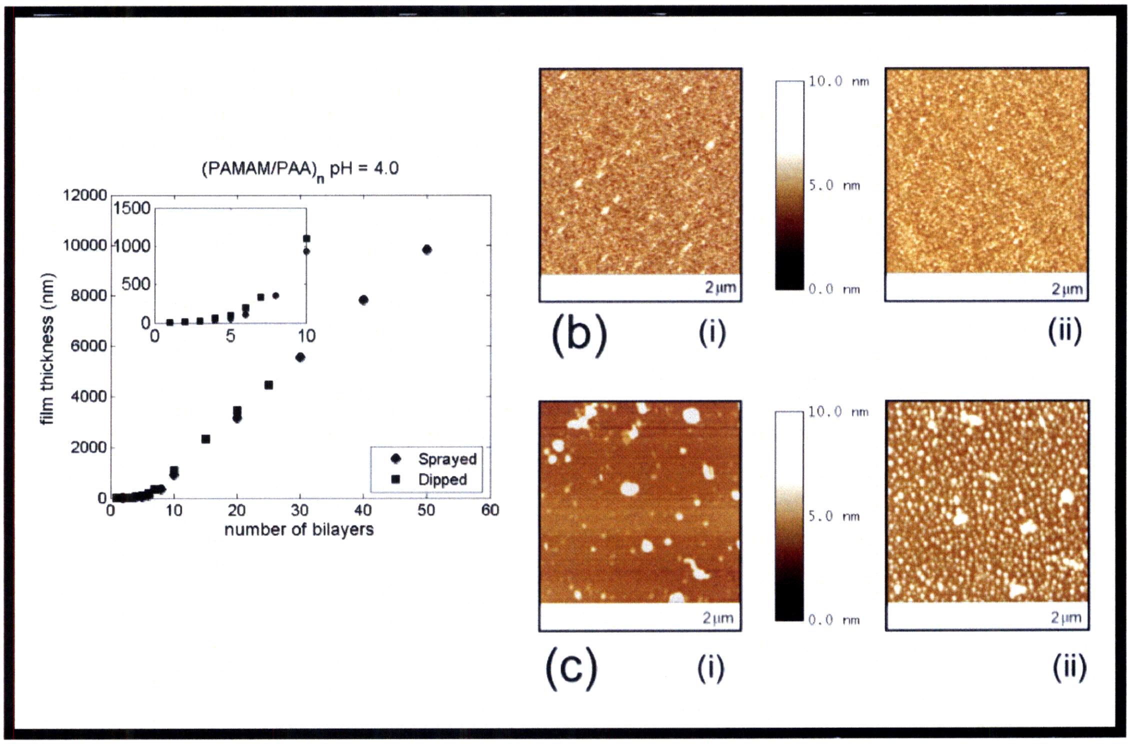

**Figure 3. Introductory growth of weak polyelectrolyte system**

**(a)** Correlation of total film thickness to layer pair number for the (PAMAM/PAA)$_n$ system, both by spray deposition and dipping. Thickness was evaluated using ellipsometry and checked using profilometry. Reported values are averages taken from several data points on a silicon wafer and vary by less than ± 100 nm. Both dipped and sprayed films exhibit linear growth rates above 5 layer pairs, with an initial non-linear growth regime. **(b)** AFM height images of sprayed (PAMAM/PAA)$_n$ (i) 0.5 layer pairs; PAMAM surface and (ii) 1.0 layer pairs; PAA surface. Coverage is low but uniform. **(c)** AFM height images of dipped (PAMAM/PAA)n (i) 0.5 layer pairs and (ii) 1.0 layer pairs. Initially, aggregates of PAMAM dendrimer deposit, although the aggregates are smaller in the case of spray deposition.

Finally, it was confirmed by atomic force microscopy (Figure 4) that no directional order has been developed in the coating as a result of the draining thin-film of polyelectrolyte solution, nor via the centrifugal motion imparted by the slow rotation of the substrate during deposition. The rotation simply serves to eliminate any incidental pattern developed by slight misalignment of the three nozzles during spraying. It should be noted that in future tests discussed in the remaining chapters of this manuscript no rotation was imposed on the substrate during spraying. It was found that rotation of the substrate simply widens the usable area of film on the substrate as more of the substrate can make its way into the overlapping paths of all three nozzles if it is rotating. Nozzles with adequately large spray cones can alleviate this issue and extend the coverage of quality film over the entire substrate.

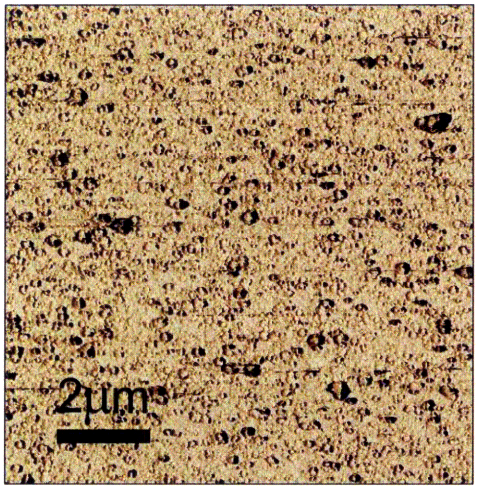

**Figure 4. AFM of Layer-by-Layer film**

10 micron by 10 micron AFM phase image of silicon wafer coated with $(LPEI/PAA)_{50}$ film. RMS roughness over the entire imaged area is 17.6 nm as measured through AFM.

### 1.3.3 Extension beyond Traditional Polyelectrolytes

If the Spray-assisted LbL technique were to have a shortcoming, it is reasonable to expect it would occur in systems where weaker substrate-polyion interactions are involved. In these cases interactions which would be strong enough to facilitate deposition during a prolonged stagnant soak may not be sufficient to initiate assembly during a turbulent spray. To test the flexibility of the Spray-LbL as a valid alternative to the traditional dipped technique we have selected several systems that assemble via non-traditional polycation-polyanion electrostatic interactions. For example, whereas Coulombic forces drive electrostatic LbL formation, hydrogen bonding can foster multilayer formation when a hydrogen-bond donor and acceptor are used.[17,48] Deposition of this sort is extremely sensitive to variations in solution pH. Thus the closed vessels and short deposition times inherent to the spray-LbL process, which are ideal for minimizing evaporation and controlling solution pH and consistency, make the process well suited for hydrogen bonded systems. Although hydrogen bonding interactions are significantly shorter range and less stable than the electrostatic interactions discussed up to this point, $(PEO/PAA)_n$ films can be deposited via the spray method yielding linear growth as shown in Figure 5. Again the presence of an introductory growth period, similar to that shown for PEO hydrogen bonded systems by Sukhishvili[17] is observed. After eight cycles have completed however, growth occurs at a constant rate of 30 nm per layer pair uniformly coating the substrate.

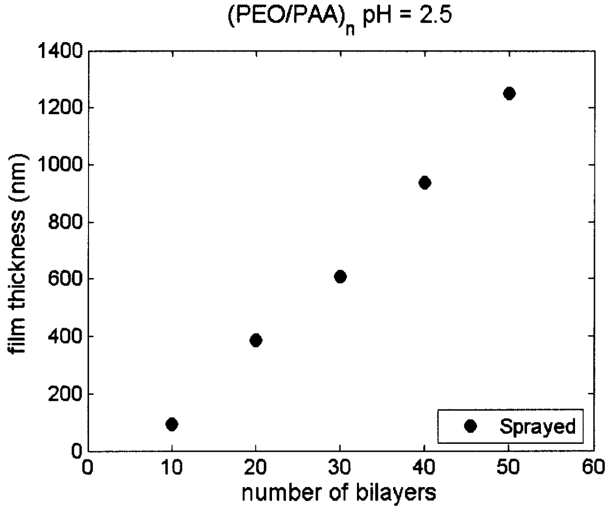

**Figure 5. Growth curve for a hydrogen-bonded LbL system**

Correlation of total film thickness to layer pair number for the $(PEO/PAA)_n$ system. Indicates that even hydrogen bonded films grow linearly, as well as uniformly, via the spray-LbL technology. Reported values are averages taken from several data points on a silicon wafer and vary by less than ± 20 nm.

Spray-LbL also proves convenient for the deposition of rigid colloidal nanoparticles, which are unable to strengthen their interaction with the developing film by bending and inter-penetrating the underlying layers. Success was demonstrated by alternating negatively charged titanium dioxide nanoparticles with positively charged PDAC. Colloidal $TiO_2$ nanoparticles were synthesized via the controlled hydrolysis of titanium isopropoxide in an absolute ethanol solution of tetrabutyl ammonium hydroxide. Upon refluxing at 100°C for three days, the TBA stabilized particles had mean diameter of 7 nm and Zeta-potential of roughly -34 mV. In this case contact time between sprayed solution and substrate was more than sufficient to adhere particles and develop constant linear growth, detailed in Figure 6. X-ray diffraction of a $(TiO_2/PDAC)_{50}$ film, the results of which are shown in Figure 7, confirms that anatase phase nanoparticles have in fact been deposited in the film. Atomization immediately prior to contact with the substrate insures deposition of particles instead of agglomerated clusters.

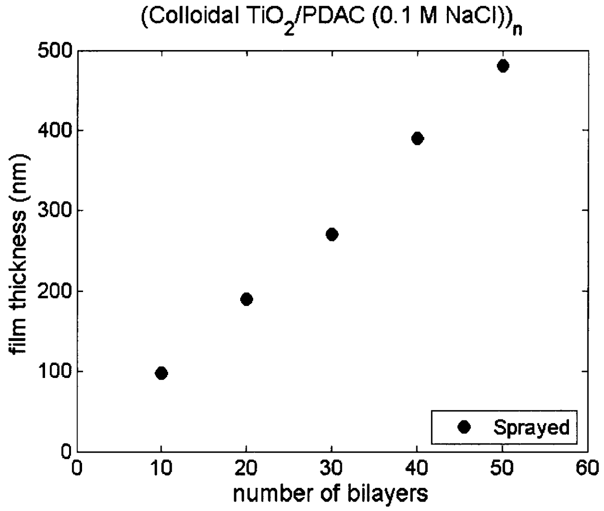

**Figure 6. Growth curve for a nano-particle containing LbL system**

Correlation of total film thickness to layer pair number for the (colloidal $TiO_2$/PDAC)$_n$ system. Profile demonstrates constant rate of growth when one charged species is replaced by charged nanoparticles. Reported values are averages taken from several data points on a silicon wafer and vary by less than ± 10 nm.

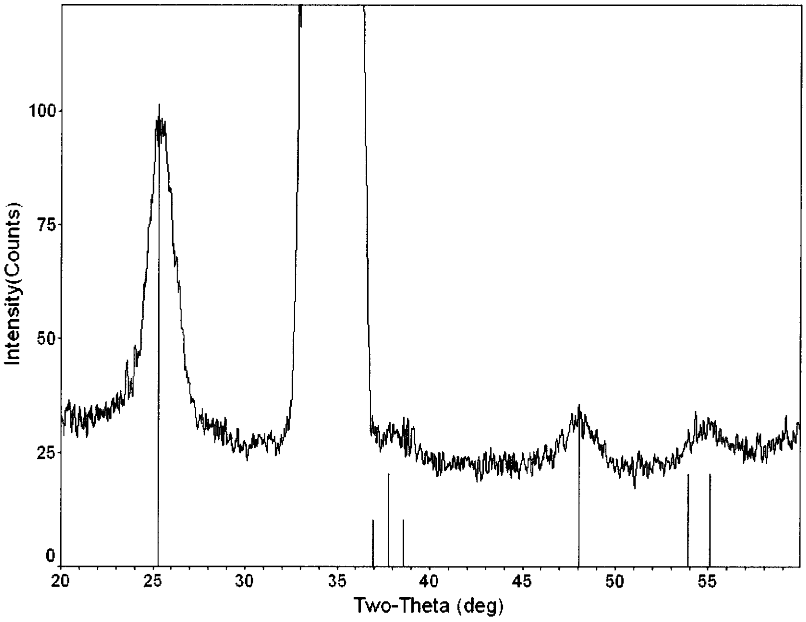

**Figure 7. XRD spectrum of $(PDAC/TiO_2)_n$ film**

X-ray diffraction spectrum confirming the presence of anatase phase $TiO_2$ particles in the film. No rutile or brookite appears to be present. Anatase diffraction lines have been overlaid for reference, and the spectrum was stopped at 65° to eliminate detector damage from the <100> silicon peak during an extended scan.

### 1.3.4 Extension to New Substrates

Similarly, weakened substrate-polyion interactions can be caused by the underlying substrate as well. For example, as a challenging test of the spray-LbL technique's ability to coat textile materials DuPont Tyvek, composed of spunbound high density polyethylene fibers, was selected as a substrate. Uncoated Tyvek is quite hydrophobic, as indicated in Figure 8(a), where it exhibits an advancing contact angle slightly greater than 150°. The three dimensional texture of uncoated Tyvek is readily seen in Figure 9(a) allowing one to see individual poly(ethylene fibers). Interestingly, the ultra-fine mist generated as the solution exits the atomizing nozzle is capable of delivering charged species uniformly, even to a hydrophobic surface.

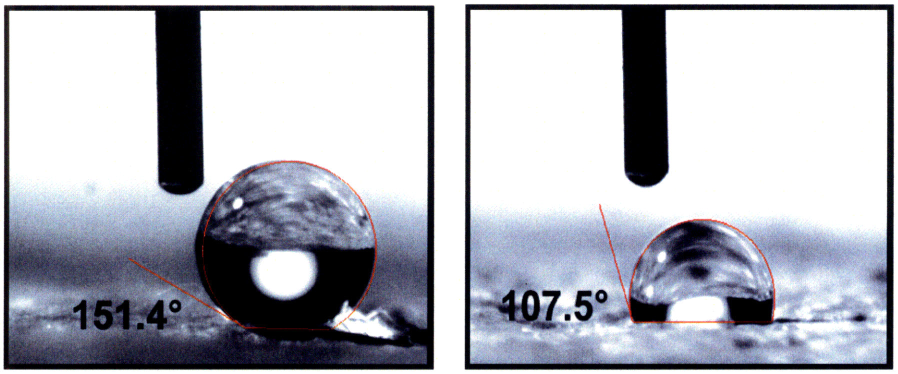

**Figure 8. Wetting contact angle analysis**

Wetting contact angle observed between water and (a) uncoated DuPont Tyvek. Observed advancing contact angle is 151 degrees. Part (b) shows the wetting contact angle observed between water and Tyvek coated with $(LPEI/PAA)_{100}$ film. The observed advancing contact angle is 107 degrees, which is significantly more hydrophilic than uncoated Tyvek.

Figure 9(b) shows macro scale uniformity of the same Tyvek swatch, now coated with 100 layer pairs of (SPS/PDAC) containing 0.10 M NaCl, typically added to screen ionic interactions and increase deposition thickness. As ionic crosslinks form between the polymer chains, salt ions are ejected, forming crystals on the surface. The short rinse time is intentionally insufficient to dissolve and rinse away the crystals, which are visible in the image. The salt is later removed by soaking the coated Tyvek $(SPS/PDAC)_{100}$ in neutral pH water for a period of 15 minutes. The same film can be seen after soaking in Figure 9(c) at higher magnification. Further magnification of the image shows that soaking has only removed the salt crystals, leaving individually coated fibers behind in Figure 9(d). Roughness of the LbL film can be seen which is a result of salt crystallization during the deposition process (the salt crystals increase the surface roughness seen by each successive exposure of polyion). Longer rinse cycles (on the order of 1 minute) can eliminate the salt crystals, if surface roughness is not desirable. By soaking to remove the salt after deposition, however, we are able to achieve much shorter cycle times.

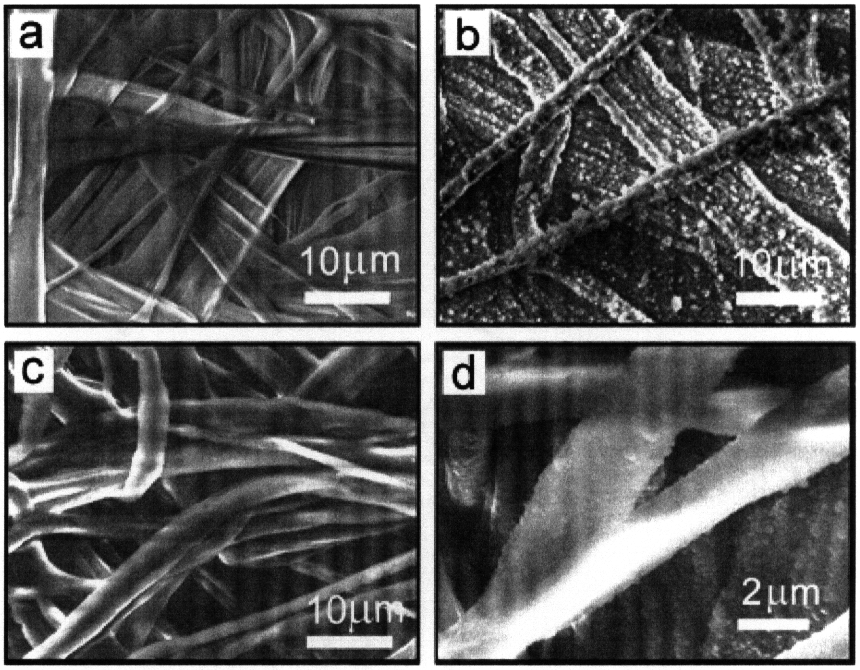

**Figure 9. LbL on hydrophobic substrate**

**(a)** ESEM image of uncoated Tyvek. Magnification of 2000x shows individual fibers forming a three-dimensional mesh. **(b)** ESEM image of Tyvek coated with $(SPS/PDAC)_{100}$ film using the automated spray system. 2000x magnification reveals salt crystals remaining on the fibers in the absence of an extended soaking period in water. **(c)** ESEM image of Tyvek coated with $(SPS/PDAC)_{100}$ film followed by a 15 minute soak period in fresh water, similar to the rinse step in the dip process. All salt crystals have been removed. (2000x magnification) **(d)** 8000x magnification of Tyvek coated with $(SPS/PDAC)_{100}$ and then soaked in water. Salt crystals have been washed away, and individual fibers have been conformally coated by automatic spraying process.

The process appears to have conformally coated the polyethylene fibers even at varying depths within the surface of the material itself. Again, the ultra fine mist allows very small droplets to transport the charged species, effectively wetting an otherwise hydrophobic material. We are able to treat the macroscopic material with a hydrophilic coating, which can be seen in Figure 8(b). Contact angle can then be used to examine the hydrophobic or hydrophilic nature of the coating's surface, that it is uniform and that the surface properties of the substrate have been macroscopically changed.[49] Here, a coating of $(LPEI/PAA)_{100}$ reduces the advancing contact angle of a droplet of water from ~150° on uncoated Tyvek to less than 110°, a change of more than 40° in wetting contact angle. According to the Cassie-Baxter Law the apparent contact angle for a liquid droplet on a porous or rough surface which can be modeled as cylinders, $\theta^*$, can be calculated using

$$\cos\theta^* = \frac{x(\pi-\theta)}{x+1}\cos\theta + \frac{x\sin\theta}{x+1} - 1 \qquad \textbf{Eqn. 1}$$

where $\theta$ refers to the contact angle observed when the liquid interacts with a smooth surface of the material in question, and $x = d / s$, the ratio of average cylindrical diameter to separation distance between adjacent cylinders.[50] Tyvek is composed of flashspun high density polyethylene fibers ($\theta_{HDPE} = 93°$ [51]), while the observed value of $\theta^* = 151.4°$ for the untreated sample shown in Figure 8a. In this example

$$\cos(151°) = \frac{x\left(\pi - \frac{93}{180}\pi\right)}{x+1}\cos(93°) + \frac{x\sin(93°)}{x+1} - 1 \qquad \textbf{Eqn. 2}$$

and x can be calculated as 0.158. The $(LPEI/PAA)_{100}$ treated sample shown in Figure 8b can be analyzed in a similar fashion. The experimentally determined wetting contact angle for smooth $(LPEI/PAA)_n$ films is approximately 40°, whereas the contact angle observed for the treated Tyvek sample, $\theta = 107.5°$, indicates it is less hydrophobic than the virgin Tyvek. Proceeding as before

$$\cos(107°) = \frac{x\left(\pi - \frac{40}{180}\pi\right)}{x+1}\cos(40°) + \frac{x\sin(40°)}{x+1} - 1 \qquad \textbf{Eqn. 3}$$

indicating x has increased to 0.392. As expected the average fiber diameter has been increased while the separation distance between neighboring fibers has slightly decreased, leading to a 2.5 fold increase in x. A sufficiently uniform coating of (LPEI/PAA) has been deposited from aqueous solutions onto an otherwise hydrophobic substrate to affect the macroscopic properties of the surface. While the hydrophobicity of Tyvek provides a particularly challenging test of the Spray-LbL technology, similar results have been obtained in coating cotton textile, thus demonstrating the versatility of the technology toward a variety of absorbent or even hydrophobic substrates.

## 1.4 Conclusions

The layer-by-layer method can be successfully utilized to deposit thin, uniform multilayered films, but can require lengthy process times. Spray-LbL has been developed to drastically reduce process times by eliminating diffusion from the mechanism. We have successfully demonstrated the utility of the Spray-LbL technology by showing films of traditional polyelectrolytes can be made of comparable quality in 25-fold shorter process times, and then extending the range of applications to include systems with weaker substrate-polyion interactions such as hydrogen bonded films, dendritic compounds and colloidal nanoparticles. Finally, the Spray-LbL technology was used to conformally coat individual fibers within the textured surface of a hydrophobic textile, dramatically affecting its macroscopic properties through microscopic fiber modifications. The work here lays the groundwork for scale-up and future development of an array of such systems capable of coating much larger substrates as well as three dimensional ones, making spray-LbL technology attractive on an industrial scale.

## Further Developments on Spray-LbL

Since the publication and disclosure of the material contained in this Chapter, there has been significant interest generated in the Spray-assisted LbL technique. Most notably, the number of publications investigating sprayed variations of electrostatic assembly has jumped from two, prior to these results, to more than 20 today. Spray-LbL has been attempted using home-made systems ranging in complexity from hand-operated plant sprayers[40] or air-pump spray cans[41,52-55], to an automated system equipped with nebulizers and syringe pumps[42,56-58]. Even the automated system used to spray films in our laboratories has evolved through several revisions (see Figure 10)[31-33]. Detailed engineering specifications for the most recent revision (Figure 10d), including mechanical and electrical design drawings, parts list, and operating limits, can be found in the Appendix. Two variations on the Spray-LbL technique have been developed; Spin-spray-LbL (SSLbL)[59,60] offers similar improvements over dipped-LbL in process time to those observed using Spray-LbL, however by blending the spin-coating and spraying techniques SSLbL suffers the shortcomings of spin-LbL. In this case significant amounts of material are thrown from the substrate during spinning and wasted, while the physics of the spinning process places severe limitations on the size and geometry of substrate which can be coated. Effectively SSLbL appears to defeat the purpose of Spray-LbL by invalidating the scalability advantages. Second, reactive-LbL spray deposition[54,56], which allows charged complexes to react in the coating during spraying, a phenomena which was previously unavailable using the dipped procedure, presents an interesting modification of Spray-LbL. Processing can be simplified by reactively generating nanoparticles in a developing film, rather than synthesizing them prior to deposition, however the most recent developments using this technique have shown very low concentrations of particles incorporated via reactive-LbL. For the time being Spray-LbL of colloidal nanoparticles remains the most promising technique to engineer nanoparticle composites.

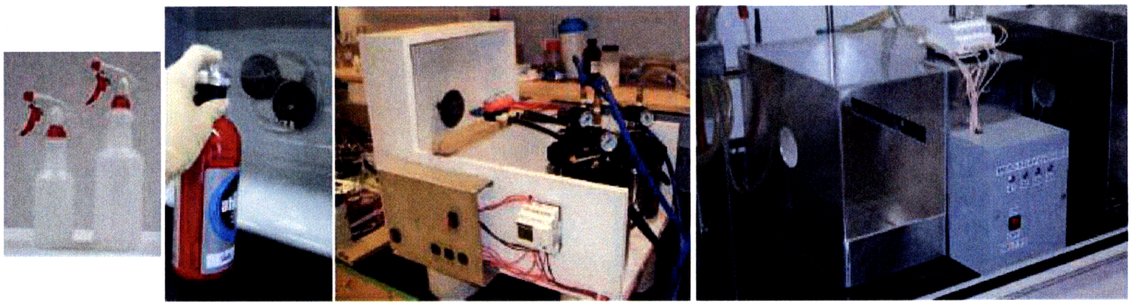

**Figure 10. Spray platform development**

Development of the automated Spray-LbL system in the Hammond group over the years has progressed from (a) hand-operated plant sprayers, to (b) hand-operated pressurized cylinders, to (c) an automated, micro-relay controlled, pressure tank system, and finally to (d) an automated, micro-relay controlled, fully enclosed Venturi type system. The most recent version minimizes wasted solution due to substrate overshoot, and speeds clean-out by minimizing dead-volume in the fluid handling system. It can also be fitted with a vacuum attachment to conformally coat porous substrates.

Sprayed films have been shown to be significantly more stratified than dipped films of the same materials [52,54], and can be deposited as much as 500 times more rapidly[52]. Researchers have also had success spraying films containing intact vesicles[61]. The value and duration of the rinse cycle remains a topic of ongoing research. Some results indicate that films can be dried and re-hydrated in between layers with little effect on film quality[57], while others demonstrate techniques to simultaneously spray polycation and polyanion solutions eliminating entirely the need for a water rinse[42]. Sprayed growth rates appear to be independent of molecular weight[58], but much debate still exists as to whether sprayed growth is faster[53], slower[52,57], or identical[41] to dipped growth. Similarly, sprayed films have been reported to be rougher[53], smoother[52], or identical[41] to dipped films of the same chemistry. Indeed, the art of spraying is still relatively unexplored, and conflicting reports as to film quality will continue to appear until a standardized method and apparatus are universally adopted. At the forefront of this exploration will be work to understand the physical differences between sprayed and dipped films, which should simultaneously bring a greater understanding to the Layer-by-Layer technique in general.

# 2. Photocatalytic Layer-by-Layer Coatings

## Abstract

Highly reactive Layer-by-Layer (LbL) films have been developed as protective coatings intended for application on fibers worn by military personnel. In this chapter, the previously discussed Spray-assisted LbL (Spray-LbL) technique is used to electrostatically assemble an anionic species, titanium dioxide nanoparticles ranging from 5 to 10 nm in size which are prepared in a stable colloidal solution specifically designed for this application, and a cationic species, which can be one of several traditional synthetic polycations, including weak and strong polyelectrolytes. The resulting coatings are mechanically stable and offer selective protection when the wearer is exposed to UV radiation (e.g. sunlight); whereas the inherent water transmissive nature of the multilayers allows for much greater water vapor transport rates as compared to an inert rubber barrier material. Permeation tests of coated materials were conducted in a specially engineered cell by exposing the materials to a CWA simulant, and demonstrate a 95% decrease in toxic agent permeation when subjected to UV exposure.

## 2.1 Introduction

Increasing concern over the use of chemical warfare, combined with more frequent potential exposure to toxic chemical environments faced by soldiers and emergency care providers, has heightened the need for new protective measures. While traditional protective gear for toxic cleanup or exposure has relied on thick layers of dense rubber and/or activated charcoal liners, which act primarily as diffusive barriers to resist mass transfer, this strategy is not tenable for routine daily duty. Reactive coatings, which are able to selectively degrade toxic chemicals, including chemical warfare agents (CWAs) and environmental toxins such as $NO_x$ and $SO_x$, while still affording the wearer a high degree of water vapor permeability and thus greater comfort, are an interesting strategy for protection against low to moderate level exposure. Such coatings could also provide a route to self-cleaning or decontaminating surfaces or fabrics for military or commercial use.

According to military specification MIL-DTL-32102, the Joint Services Lightweight Integrated Suit Technology (JSLIST) suit must provide protection against 10 $g/m^2$ of agents HD (mustard), GD (soman) and VX after 720 hours of wear and 6 launderings. In this case protection is defined as less than 10 μg of vapor permitted to penetrate over 24 hours (i.e. less than 1%). Assuming a 1 $cm^2$ sample at ambient temperature and pressure is subjected to 100 ppm of toxic agent, the steady state permeance must be less than $5.5 \times 10^{-8}$ $cm^3(STP)/s \cdot cm^2 \cdot cmHg$ over the duration of the test. Simultaneously, the specification requires water vapor transport to be at least 1 $kg/m^2 \cdot day$ which translates to a steady state permeance greater than 6.1 $cm^3(STP)/s \cdot cm^2 \cdot cmHg$ and a water vapor to toxic agent selectivity of more than 8 orders of magnitude. No material exists which is able to maintain the necessary high water vapor transport rate while achieving an 8 order of magnitude selectivity simply as a selectively permeable barrier. Materials must be developed which are selectively reactive toward toxic agents to increase their affinity toward water vapor transport. One means of reactively eliminating airborne toxins which has received attention involves the photocatalytic degradation of toxic organic compounds using titanium dioxide[62-65] to generate superoxide anions, or mixed $TiO_2/SiO_2$ catalysts[63,66,67] to increase the material's bandgap and aid in volatile compound adsorption. While these strategies exhibit excellent degradative capabilities, the technique of depositing unbound powders or nanoparticles on a surface does not form a sufficiently robust coating for application on personal protective equipment. Titania has also been introduced directly into fibers via electrospinning[68], or into bulk films via traditional sol-gel routes[69]. Unfortunately as the size of the titania entity increases, it becomes more difficult to introduce the particles into a mechanically stable polymer film. The work reported in this chapter presents a strategy to achieve the success demonstrated by prior titania based systems from an ultrathin, transmissive, and mechanically stable coating which can be readily deposited on traditional military clothing and packaging, as well as a variety of other substrates including electrospun materials which will be discussed further in Chapter 4. Such a coating can be tuned for its mechanical and chemical properties via the choice of polyamine and the incorporation of other polyelectrolytes so as to achieve the reactive protection described above, while existing in a form which is durable enough to withstand the rigors of daily activity and sufficiently discrete so as not to hinder the performance of the underlying material. We have developed a coating which can be readily deposited by the versatile Layer-by-Layer

(LbL) deposition method[5], and provides a reactive barrier of more than 99% efficiency against a saturated environment of the sulfur mustard simulant compound chloroethyl ethyl sulfide (CEES) when exposed to ultraviolet radiation. While similar recent approaches have been taken to introduce titania nanosheets into photocatalytic LbL films[70-72] the resulting coatings were shown to degrade organic hydrocarbons at relatively low quantities over time scales on the order of days; personal protective equipment on the other hand must have degradative properties on the time scale of minutes, at most, to be of any practical use. Furthermore, there is general concern that titania containing coatings suffer decreased chemical stability on exposure to UV. However, we have found the systems reported here to remain intact even after high yield conversions of simulant agent.

The LbL method typically employs polyelectrolytes adsorbed from dilute aqueous solutions; however, charged colloidal species can also be incorporated into the films.[3,73] In some instances charged rigid nanoparticles can take the place of one[12] or even both[74] of the charged polyelectrolytes. It is in this manner that we have been able to incorporate reactive titanium dioxide nanoparticles of very small diameter, and therefore large reactive surface area, into a mechanically cohesive film coating. In our approach the previously discussed Spray-LbL technique is used,[30,40,41] allowing us to rapidly coat a variety of complex substrate geometries and materials including, but not limited to, cotton textile and protective plastic film.

## 2.2 Experimental

*LbL Solutions:* Poly(dimethyldiallylammonium chloride) (PDAC, MW = 100,000), and sodium chloride were purchased from Aldrich and used to make a solution of 20 mM concentration with respect to the repeat unit of PDAC, and 10 mM with respect to NaCl, in DI water. Colloidal titania nanoparticles were initially synthesized via the extremely rapid hydrolysis of titanium tetrachloride. $TiCl_4$ was diluted in methanol and chilled in an ice bath before addition of excess water according to

$$TiCl_4 + 2H_2O \rightarrow TiO_2 + 4HCl \qquad \textbf{Eqn. 4}$$

The resulting solution of 5-10 nm $TiO_2$ particles was transparent and colloidally stable with a Zeta potential of approximately +46 mV. Upon Spray-LbL deposition versus a suitable polycation the coatings were not found to exhibit appreciable photocatalytic activity toward CEES. As shown in Figure 11, the titania particles were stabilized by the chlorine counter-ions in solution after the hydrolysis reaction. Upon deposition, some of these chlorine ions remained on the titania surface as part of the Stern layer effectively fouling the catalytic sites with a bound byproduct of the proposed photocatalytic reaction. This synthetic scheme was abandoned in favor of the modified sol-gel reaction described in Figure 12. Here titania nanoparticles were synthesized by slowly combining a solution of 1 part tetrabutyl ammonium hydroxide and 50 parts absolute ethanol with a solution of 1 part titanium (IV) isopropoxide and 6 parts absolute ethanol by volume. The combined solution was then slowly diluted with DI water to 4 times its original volume under rapid stirring, and refluxed for 3 days at 100°C. All chemicals were used as purchased from Aldrich. The resulting colloidal solution was analyzed using a Brookhaven Instruments

Corp. ZetaPALS Zeta-potential analyzer and, upon evaporation, a Rigaku Powder X-ray Diffractometer.

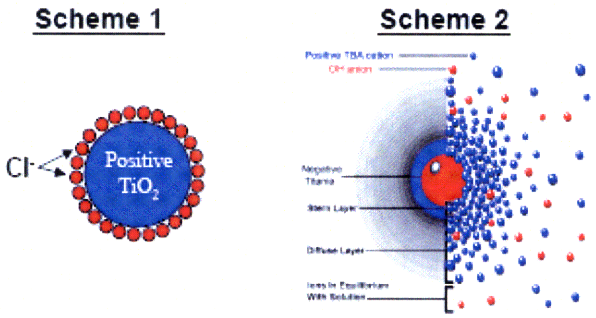
Scheme 1

Scheme 2

**Figure 11. $TiO_2$ nanoparticle synthetic results**

Positive titanium dioxide nanoparticles were synthesized via Scheme 1 (left) which were stabilized by the chlorine counterion. Alternatively, negative titania nanoparticles were synthesized via Scheme 2 (right) which were stabilized by the larger tetrabutyl ammonium cation.

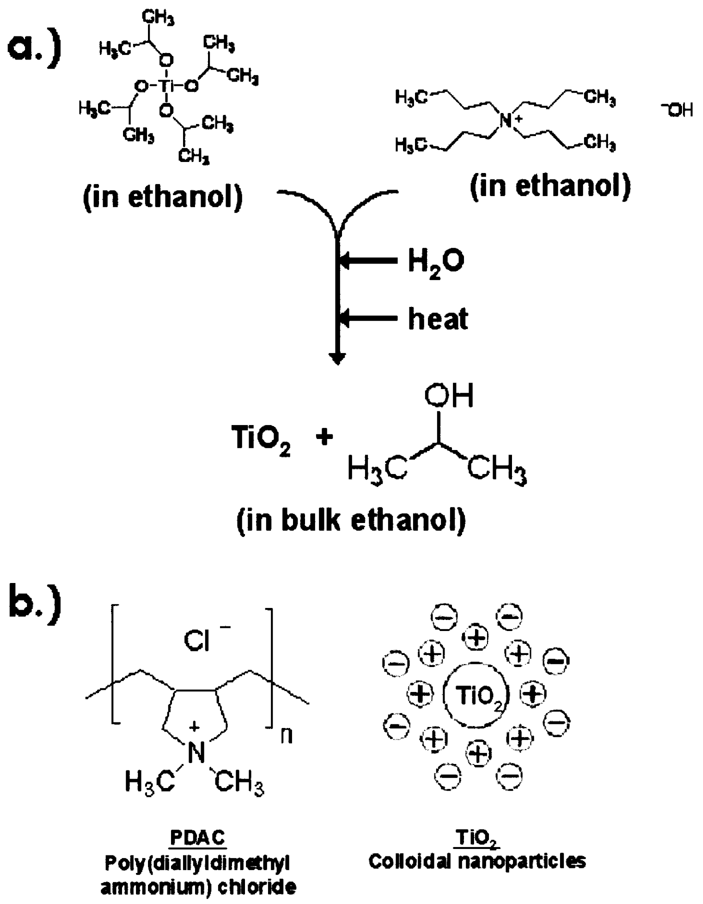

**Figure 12. Modified sol-gel procedure for $TiO_2$ synthesis**

**(a)** Reaction scheme by which colloidal titania solution is created. Upon generation of the stabilized nanoparticles in a solvent mixture of water, ethanol and isopropanol, the alcohols can safely be removed by continued heating resulting in a stable aqueous solution of colloidal particles. **(b)** Charged species deposited alternately in film construction.

*Coating Deposition and Analysis:* LbL deposition was conducted on Saran 8 plastic sheeting (12.7 micron thickness) used as purchased from Dow Chemical. Prior to deposition the plastic sheeting was rinsed with methanol and exposed to an oxygen plasma (Harrick PCD 32G) for 5 minutes to clean and hydroxylate the surface. Both solutions as well as rinse water were titrated to pH = 10 using HCl. Deposition was conducted using an automated Spray-LbL system.[30] All solutions were delivered by ultrahigh purity Argon gas regulated to 50 psi. PDAC was sprayed for 3 s and allowed to drain for 17 s, before spraying with water for 10 s and allowing it to drain for 10 s. The half cycle was repeated for the colloidal titania solution resulting in an 80 s cycle, while the full cycle was repeated 50 times to create the final coating tested here. Film thickness was determined on a Woolam XLS-100 spectroscopic ellipsometer and checked using a Tencor P10 Profilometer, while titania composition was determined using a TA Instruments TGAQ50 thermogravimetric analyzer.

*Permeation Testing:* Permeation testing was conducted in a stainless steel cell using ultrapure compressed air for the sweep gas. The contaminated stream was analyzed using a Gow-MAC Instrument Co. Series 23-550 Total Hydrocarbon Analyzer equipped with a flame ionization detector. The detector was calibrated for CEES using a certified working class calibration standard 100 ppm mixture of chloroethyl ethyl sulfide in nitrogen (Scottgas). UV illumination was provided by a Blue Wave 200 (Dymax) UV spot source filtered to ~100 mW/cm$^2$. Samples were challenged using chloroethyl ethyl sulfide (CEES) available from Aldrich. CEES is a less toxic simulant for bis(2-chloroethyl) sulfide, also known as sulfur mustard gas or simply as HD in military circles. Either molecule readily eliminates a chloride ion by intermolecular $S_N1$ substitution. If this process occurs inside a cell it generates acidic conditions that result in cell death and blistering, hence the categorization as a blister-vesicant agent. The $S_N1$ reaction also generates a highly reactive sulfonium ion which can go on to attack the guanine nucleotide of DNA strands also leading to cell death. In all tests performed in this manuscript CEES is used as a simulant for HD mustard because it can undergo similar reactions, but with only half the potency. As shown in Figure 13 CEES possesses only one chloride leaving group while HD mustard has two. Given the opportunity HD mustard can also undergo the sulfonium ion reaction twice, effectively crosslinking two DNA strands and causing more serious long-term health effects. It should be noted by anyone attempting to reproduce results seen here, CEES is a vesicant compound which can cause blisters if it comes in contact with the skin. While it is a less toxic simulant for mustard gas, extreme caution should be exercised particularly when working with CEES vapors. FTIR testing was conducted using a Nexus 870 FTIR ESP (Thermo Nicolet) in a quartz gas cell with a 10 cm pathlength.

**Figure 13. Chemical structures of CEES and HD Mustard**

*Film Construction:* We begin by synthesizing titanium dioxide nanoparticles via a controlled hydrolysis utilizing a modified sol-gel process. By limiting the rate at which the hydrolysis reaction converts titanium (IV) isopropoxide into titanium dioxide, we are able to create a monodisperse colloidal suspension of titanium dioxide nanoparticles exhibiting 5-10 nm diameters. Further investigation with x-ray diffraction indicates that the particles are of the anatase phase (see Figure 7), which is preferred for the nanoparticles to act as a photocatalyst. Zeta-potential analysis by phase analysis light scattering (Zeta-PALS) indicates that the particles carry a mean surface charge of roughly

-34 mV, implying the solution conditions are far enough removed from the isoelectric point of the amphoteric titania (pI ≈ 5.75) to ensure that the suspended particles are more than sufficiently charged to participate in LbL deposition.

A photocatalytic coating can then be deposited by alternating adsorption between the synthesized colloidal solution and a solution of a polycationic material, which in this case is poly(dimethyldiallylammonium chloride), chosen for its strong polyelectrolyte properties and thus the independence of its degree of ionization with respect to solution pH. Because a Spray-LbL system is utilized,[30,40,41] the coatings are developed at the rate of one 'bilayer' cycle every 80 seconds allowing for the creation of a 50 bilayer film in slightly more than one hour of process time.

## 2.2 Results and Discussion

Multilayer coatings were generated via the alternating misting of a 10 wt% solution of titanium dioxide nanoparticles and a 20 mM solution of PDAC. All solutions, including rinse water, were titrated to pH 10 prior to deposition. As shown in Figure 14, the growth of the $(TiO_2/PDAC)_n$ films proceeds linearly at a constant rate of approximately 10 nm per deposition cycle, suggesting that $TiO_2$ particles are adsorbed to the developing surface approximately as a monolayer during each exposure to colloidal solution. An example thermogravimetric analysis (TGA) performed on one such film constructed under these conditions can also be seen in Figure 14. Starting at ambient conditions, we find that approximately 2.6% of the film's weight at equilibrium is water, while 41% of the film is combustible organic material. Upon heating to 800 °C and holding for several hours, it is observed that titania comprises approximately 56% of the film by weight.

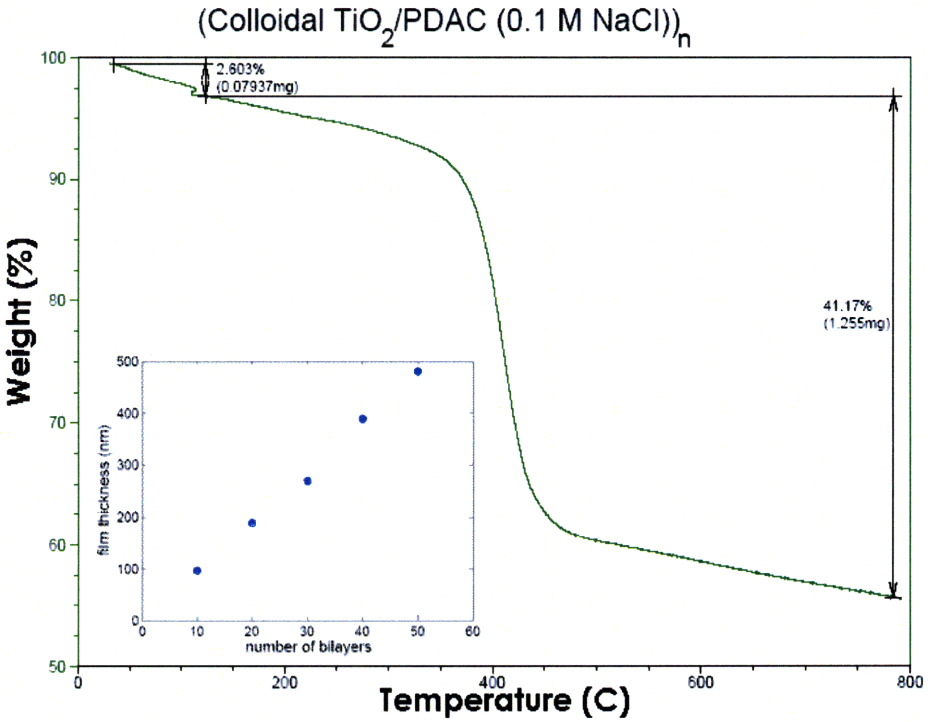

**Figure 14. Growth rate and composition of photocatalytic film**

Characterization of as deposited (colloidal $TiO_2$/PDAC)$_n$ films. Depositing all solutions at pH 10 results in a film that is ≈ 56% $TiO_2$ at ambient conditions as determined by thermogravimetric analysis. This film is deposited at a linear rate of ≈ 10 nm per bilayer (inset). Reported thicknesses are averages taken from several data points on a silicon wafer and vary by less than ± 10 nm across the matrix.

The resulting film is mechanically stable, as a result of the strong electrostatic interactions between the charged species. Hence, even though it is comprised of 56wt% rigid nanoparticles, it is able to resist gentle rubbing. This result can be attributed to the strong charge observed on the surface of the synthesized colloidal nanoparticles, as well as the intermolecular entanglements of the codeposited polyion.

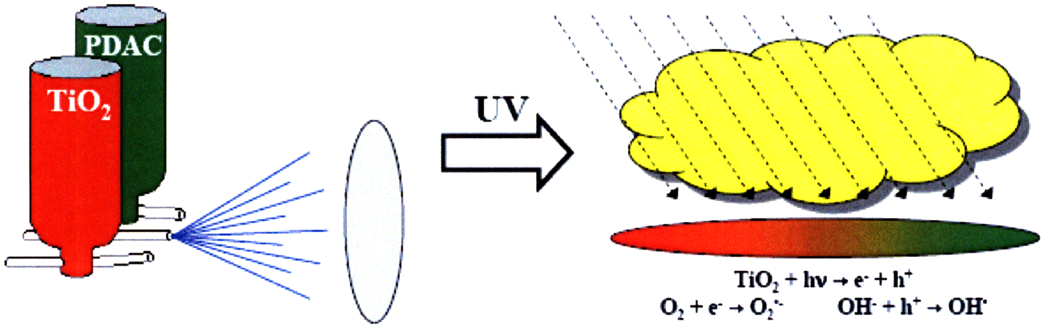

**Figure 15. Film deposition scheme**

Testing method by which Spray-LbL deposited coatings are tested for photocatalytic degradation of volatile organic compounds. Coatings are deposited, dried, and mounted in a sealed test chamber where they are exposed to the volatile organic compound and UV radiation similar to sunlight.

*Permeation Testing*: In order to conduct the desired reactive mass transfer tests a stainless steel permeation cell, represented schematically in Figure 16 and graphically in Figure 17, was specifically designed and engineered to conform to military standard MIL-STD-282F. A coated substrate sample is sandwiched, along with a 1/16" butyl rubber gasket of the same outer diameter as the sample and 13/16" inner diameter, between the face of a stainless steel plug and the base of the cell. The plug has been bored through to accommodate a second smaller plug, which then encloses a 23.3 mL vapor space above the coated sample. It is into this vapor space that a specific dose of condensed phase CEES is introduced as shown in Figure 15. As simulant vaporizes from the condensed source, the concentration of CEES in the vapor space is maintained at its saturation vapor pressure ($C_{sat} \approx 5000$ ppm) for an extended period of time until the source is consumed and the test is complete. The smaller plug is capped with a quartz wafer providing negligible adsorption of radiation in the ultraviolet wavelengths down to 200 nm. One face of the sample material is exposed to a known concentration of CEES vapor, while below the sample a stream of ultra-pure carrier gas is passed at a flow rate that is sufficiently large to ensure the partial pressure of simulant on the permeant side of the sample is negligibly small. Thus a known cross-sectional area of the sample is exposed to a saturated environment of CWA simulant creating a driving force for mass transfer in the form of a concentration gradient. The exposed cross-sectional diameter has been chosen so as to eliminate edge diffusion effects (i.e. sample thickness << cross-sectional diameter) simplifying the analysis by causing mass transfer to be predominantly uni-directional.

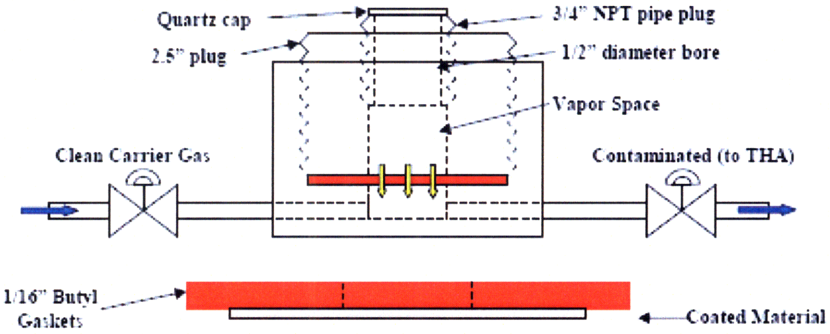

**Figure 16. Vapor permeation cell schematic**

Permeation cell in which photocatalytic testing was conducted. The cell design restricts mass transfer to one dimension through the coated material (represented by yellow arrows), while the entire surface area through which permeant is passing can be uniformly exposed to ultraviolet radiation.

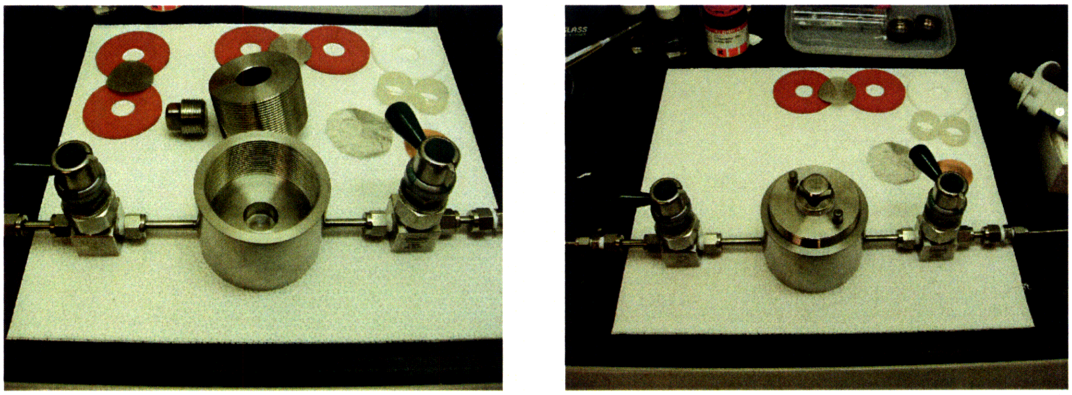

**Figure 17. Vapor permeation cell exploded view**

View of stainless steel permeation cell opened (left) with both large and small pipe plugs separate, and closed (right) with large pipe plug installed to secure sample in place and small pipe plug inserted to enclose vapor space.

Assuming the sample is sufficiently thin, so radial diffusion can be neglected, and uniform, so angle-dependent diffusion can be neglected, and that the sample is non-porous, so convection can be neglected, the equation governing cylindrical mass transfer

$$\frac{\partial C_i}{\partial t} + v_r \frac{\partial C_i}{\partial r} + \frac{v_\theta}{r}\frac{\partial C_i}{\partial \theta} + v_z \frac{\partial C_i}{\partial z} = D_i\left[\frac{1}{r}\frac{\partial}{\partial r}\left(r\frac{\partial C_i}{\partial r}\right) + \frac{1}{r^2}\frac{\partial^2 C_i}{\partial \theta^2} + \frac{\partial^2 C_i}{\partial z^2}\right] + R_{vi}$$

**Eqn. 5**

can be simplified substantially. Once adequate time has passed for a steady-state scenario to evolve, further simplification can be made to describe mass transfer within the sample.

$$\frac{\partial C_i}{\partial t} = D_i \frac{\partial^2 C_i}{\partial z^2} + R_{vi} = 0$$

**Eqn. 6**

In the special case of non-reactive samples Fick's 1st Law of Diffusion applies, in that the flux of vapor through a sample is equal to the product of the permeability, the cross-sectional area and the concentration gradient driving the mass transfer.[75,76] This relationship will be used extensively in Chapter 4 to characterize the mass transfer properties of several non-reactive barrier materials.

Returning to the permeation cell, vaporized CEES from the vapor space dissolves into the LbL coating of the sample which may or may not be photocatalytically active during the test. CEES, or the appropriate products of degradation, then diffuse through the inert substrate before leaving the sample into the carrier gas on the permeant side of the substrate. The carrier gas is then analyzed by combustion in the hydrogen/oxygen flame of a Total Hydrocarbon Analyzer equipped with an FID capable of contaminant detection at 0.01 ppm levels. Similarly, the test can also be run in conjunction with an ultraviolet spot source, equipped with a mercury vapor lamp to mimic sunlight. The lamp is capable of illuminating the exposed portion of the sample through the quartz cap above the vapor space, eliminating the risk of contamination between the UV lamp and the vapor space. The mass flux of contaminant through the sample can then be determined by measuring the concentration of contaminant in the sweep gas, as well as the flow rate at which the sweep gas is passing under the sample. Similarly, the rate at which contaminant passes through the sample can be normalized by the cross-sectional area through which mass transfer is allowed to occur, specified by the cell geometry, and the driving force for mass transfer in the form of a partial pressure gradient. Termed the permeance, the normalized flux can be calculated,

$$P = \frac{q}{A * \Delta p} = f\left(F_{carrier}, ppm_{CEES}\right) \qquad \textbf{Eqn. 7}$$

by measuring the flow rate of carrier gas as well as the concentration of CEES contaminant in the stream. The calculation gives a thickness independent interpretation of the exposure a user would expect to experience while under the protection of such a coated substrate. It should be noted that the choice of butyl rubber gaskets was not made arbitrarily. During development of the permeation cell several prospective gasket candidates underwent testing. Four rubber materials (silicone, butyl, neoprene and latex) of identical thickness were selected for their flexibility and resiliency as measured by the Shore Durometer test to ensure good sealing capabilities, and were mounted one at a time in the permeation cell as described above. Once subjected to excess CEES in the sealed vapor space, the flux of CEES through each gasket material was recorded in Figure 18. Butyl rubber exhibited the longest breakthrough time, more than three times that of latex or neoprene, implying butyl rubber took up CEES least readily of the four flexible rubbers tested.

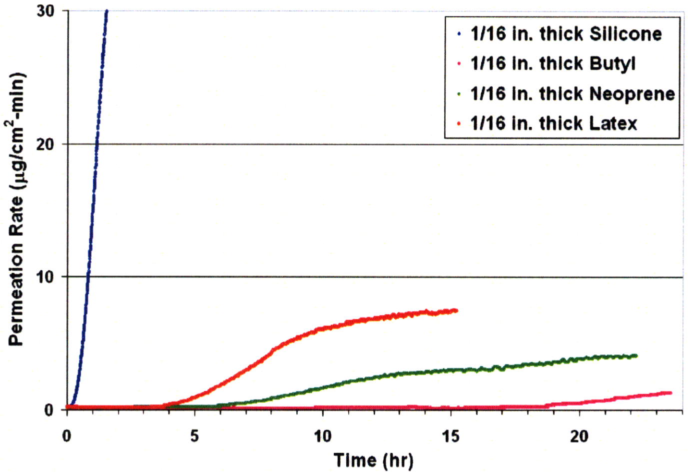

**Figure 18. Permeation rates of gasket materials**

Observed permeation rates of several possible gasket material candidates. Silicone, butyl and neoprene all rated 60 on the Shore Durometer scale, while latex rated 38 indicating it was a slightly softer rubber.

*Photocatalytic Capabilities*: For the purpose of testing the photocatalytic capabilities of the $(PDAC/TiO_2)_n$, a 50-cycle deposition was performed using the Spray-LbL technique. The film was constructed on a 12.7 µm thick nonporous poly(vinylidene chloride) sheet available under the trade name Saran 8 from the Dow Chemical Company. This substrate material was chosen for several reasons. The inherent negative surface charge on the plastic sheet enables the adherence of the first few monolayers to the substrate via electrostatic interactions. Further, by choosing a nonporous substrate with easily characterizable gas permeation properties it is possible to determine mass transfer characteristics of the uncoated substrate to serve as a benchmark for future comparisons with the coated material. Saran is a biaxially oriented monolayer barrier film which is moderately CEES permeable, a property which is quantified below. It is also inert to chlorinated compounds such as CEES, making it an ideal substrate for permeation testing of $(PDAC/TiO_2)_n$ reactive coatings.

The coated sample was then mounted in the permeation cell, and 3 μL of condensed phase CEES were introduced into the vapor space above the sample. As the vapor permeated through the sample it was collected and swept away to the Total Hydrocarbon Analyzer which was calibrated for CEES identification. The resulting mass flux, in g CEES per minute, can be seen in Figure 19. During the first 15 minutes of testing no contaminant is observed in the permeant vapor. After this breakthrough time, $t_{b,dark}$, however the concentration of CEES in the sweep gas continues to increase as the sample becomes loaded with CEES. The parabolic downturn occurs as the condensed source of CEES in the vapor space becomes depleted and is no longer able to maintain a constant vapor pressure above the sample. A maximum concentration of CEES in the permeant stream is observed at 33 ppm. The test is conducted for two hours, which is sufficient for the large majority of the CEES to exit the system.

Upon complete evacuation of CEES from the system further testing can be conducted. An identical film was subjected to a similar 3 μL loading. This time however ultraviolet light was passed through the quartz cap of the cell illuminating the area of the coated sample simultaneously exposed to the saturated atmosphere of CEES. Again permeant vapor is removed by the sweep gas and analyzed by the THA. The observed instantaneous mass flux can also be seen in Figure 19. In this scenario, no contaminant is detected by the THA prior to a shorter 8 minute breakthrough time, $t_{b,UV}$. This can be explained by the solution-diffusion mechanism by which CEES transfers across the material. Permeability is typically expressed as the product of the diffusivity of a molecule through the solid matrix and the solubility of the vapor molecule in the solid.[77] As the intense UV radiation falls on the titania particles some of the energy is used to generate electron-hole pairs which eventually result in the superoxide anions that make titania useful as a photocatalyst. The remainder of the energy is absorbed as radiant heat, slightly increasing the temperature of the underlying solid material. This rise in temperature will serve to increase both the diffusivity and the solubility of CEES throughout the sample. A slight increase in permeation rate is thus not surprising, and the contaminant molecules appear twice as rapidly in the permeant stream.

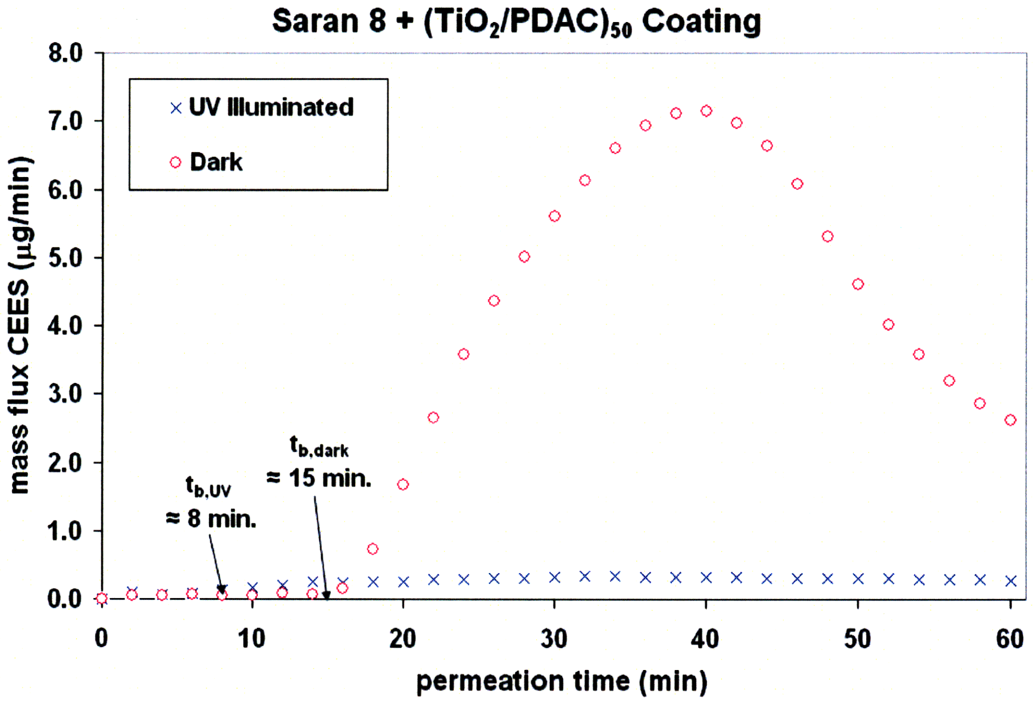

**Figure 19. Reactive permeation data**

Mass flux of CEES through a coated sample as measured in the carrier gas passing below the sample. Identical samples were exposed to 3 μL loadings of CEES and allowed to permeate. The test was conducted both with (X) and without (O) UV illumination.

Aside from the temperature induced decrease in resistance to mass transfer, it is clear that the overall CEES permeation has been greatly reduced. This effect becomes even more pronounced as time passes. The peak concentration of CEES in the permeant vapor occurs at roughly the same elapsed time, but the degradation of CEES vapor in the photocatalytic coating has reduced this peak value to less than 1.5 ppm. Thus the reduction in maximum CEES concentration on the permeant side of the sample membrane was decreased by more than 95% when subjected to UV light. It is also beneficial to analyze the protective capabilities of the film from a net exposure standpoint. Since these tests have been conducted with 3 μL loadings of CEES, a stoichiometric constraint imposed by the amount of oxygen present in the vapor space available to participate in the photocatalytic reaction at the titania surface, this type of analysis is only appropriate up to the point where the condensed CEES source appears to run out. After this time the vapor space is no longer maintained at the saturation concentration as CEES is reactively consumed by the film, and the partial pressure gradient driving mass transfer begins to decrease. This appears to occur at approximately 40 minutes of test time. Up to this point, only 5.1 μg of CEES have passed through the photocatalytically active (i.e. exposed to UV light) sample. This corresponds to less than 1% of the 3.21 mg of CEES introduced into the vapor space. A more thorough understanding of the net flux over longer periods of time is necessary to fully evaluate this material and will be obtained in the future after some modifications to the test cell. However, it can be concluded from these preliminary results that the (colloidal

$TiO_2$/PDAC)$_{50}$ coating, when illuminated by UV light, can exhibit reactive protection for at least 40 minutes of more than 99% from a saturated environment of CEES.

The net mass flux over the one hour time frame displayed in Figure 19 can also be calculated by integrating the instantaneous flux over the length of the test. In the dark membrane test, this net flux corresponds to 104 μg, while the UV illuminated test results in 8.2 μg net permeation. By forming a ratio of the net flux observed in the presence of UV light to that observed without UV light, a 10-fold reduction is seen. This 10-fold reduction can then be expected in further testing independent of the fact that a steady state scenario was never actually reached in these tests. As mentioned above, a benefit of using a nonporous substrate such as Saran 8 is that material mass transfer properties can be determined using this type of permeation cell by simply increasing the condensed CEES loading until a steady state diffusion scenario is obtained. The increased loading provides a larger condensed phase source capable of maintaining the saturated vapor space until the sample reaches diffusional equilibrium. Prior to these tests it was determined that the steady-state concentration of CEES observed in the sweep gas, of identical flow rate, below a sample of uncoated Saran 8 was determined using Figure 20 to be 113 ppm. Coupled with the flow rate of sweep gas this uncoated control test corresponds to a steady state mass flux of CEES through Saran 8 of 32.7 μg/min, five times greater than the largest rates observed in either of these tests. We can thus assume that the multilayer coating provides a significant portion of the resistance to mass transfer across the sample.

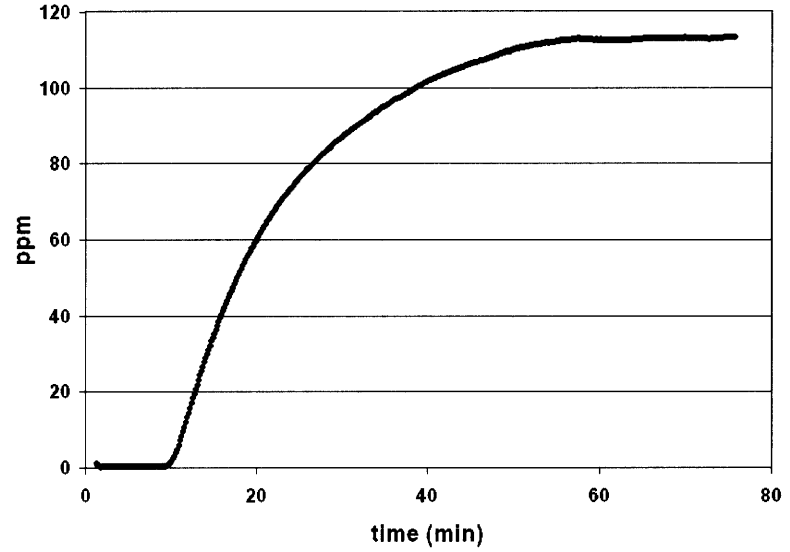

**Figure 20. Example permeance profile for Saran 8**

Plot records the concentration of CEES in the sweep stream below a nonporous Saran 8 barrier film.

It has been suggested by previous work that ultraviolet illumination of LbL constructed films composed of titania nanosheets and PDAC will elicit the photocatalytic decomposition of the PDAC in the film, producing inorganic multilayers composed only of the titania nanosheets and charge balancing ammonium ions.[70] The resulting coating would presumably have a marked decrease in mechanical stability, as well as a change in film permeability over time as the structure collapses and the titania sheets are freed of the PDAC. If this were the case the formation of $NH_4^+$ upon UV illumination, generated from the decomposition of PDAC, would be readily observable in the film via FTIR analysis as a sharp peak around 1427 $cm^{-1}$ as well as three broad peaks in the 2800-3300 $cm^{-1}$ range. As can be seen in Figure 21, UV exposure of the (colloidal $TiO_2$/PDAC)$_{50}$ coating for 60 minutes does not appear to generate these results. While the sharp peak at

1107 $cm^{-1}$ is clearly visible, due to Si-O-Si stretching from surface oxides on the silicon wafer, no peaks have been generated at 1427 $cm^{-1}$. Three very small peaks at 2861, 2934, and 3029 $cm^{-1}$ can be seen, indicating that a small portion of the available PDAC has been photocatalytically decomposed, but this does not appear to have had an effect on the mechanical stability of the coating. Furthermore, it has recently been demonstrated that $NO_3^-$ ions are a reasonable degradation product of short-chain alkyl amines as well.[78] However no increase in absorption in the 1410-1340 $cm^{-1}$ region is observed upon UV exposure. Even after intense UV exposure for 60 minutes the film still resists rubbing indicating that it has not undergone collapse of the interpartical galleries as a result of PDAC decomposition.

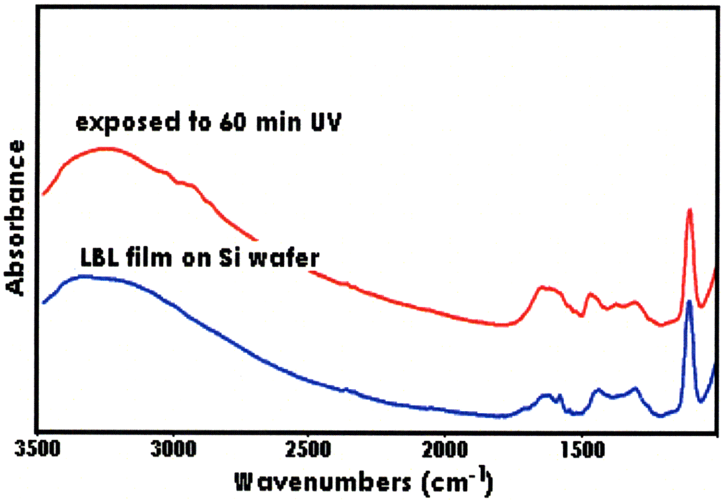

**Figure 21. UV degradation of PDAC**

FTIR spectra of **(a)** the as deposited (colloidal $TiO_2$/PDAC$)_{50}$ coating on IR transparent silicon, and **(b)** the same coating after 60 minutes of UV exposure.

*Photocatalytic Confirmation*: It should be noted in Figure 19 that the tail of the data collected from the 'dark' test extends for prolonged times at low values, as ever decreasing amounts of CEES desorb from the once-saturated film, and diffuse into the sweep gas over several hours. As less CEES is dissolved in the sample the driving force to leave the solid and enter the gas stream decreases, and the appearance of several ppm of CEES for some time is to be expected. Rather than attempting to quantify the amount of CEES accounted for in these tails we have chosen to focus the previous discussion on the peak dosage allowed during the early portions of the test. Thus to confirm the presence of a photocatalytic degradation reaction, and not simply a strong absorption of CEES with slow desorption over extended time periods, further testing was conducted on the UV-illuminated sample. A batch FTIR test was constructed by mounting a 0.51 in$^2$ swatch (i.e. identical to the exposed cross-sectional area within the permeation cell) of coated sample in a sealed quartz gas cell. Again 3 μL of condensed CEES were introduced into the cell through a septum and allowed to vaporize for 10 minutes, simulating the breakthrough period afforded by the sample in the permeation cell. The sample was then illuminated by the same UV source, and the vapor in the cell analyzed at ten minute intervals over a thirty minute test period. The simplified mechanism by which superoxide anions ($O_2^{\bullet-}$) and surface hydroxyl radicals ($OH^{\bullet}$) are generated and CEES is subsequently decomposed is as follows

$$TiO_2 \overset{hv}{\rightarrow} e^- + h^+ \qquad \textbf{Eqn. 8}$$

$$O_2 + e^- \rightarrow O_2^{\bullet-} \qquad \textbf{Eqn. 9}$$

$$H_2O \rightarrow H^+ + OH^- \Rightarrow OH^- + h^+ \rightarrow OH^{\bullet} \qquad \textbf{Eqn. 10}$$

$$CEES + 7.5O_2^{\bullet-} \rightarrow 4CO_2 + 3H_2O + H_2SO_4 + HCl \qquad \textbf{Eqn. 11}$$

The gas phase decomposition has been investigated and it has been shown that there are a variety of less toxic intermediate byproducts which are also observed.[63,65] When a photocatalytic reaction is occurring, the appearance of compounds such as ethylene, chloroethylene, acetaldehyde, chloroacetaldehyde and carbon dioxide should be readily observable in the resulting vapor. Portions of the FTIR spectra taken initially and after 10, 20 and 30 minutes of UV irradiation can be seen in Figure 22.

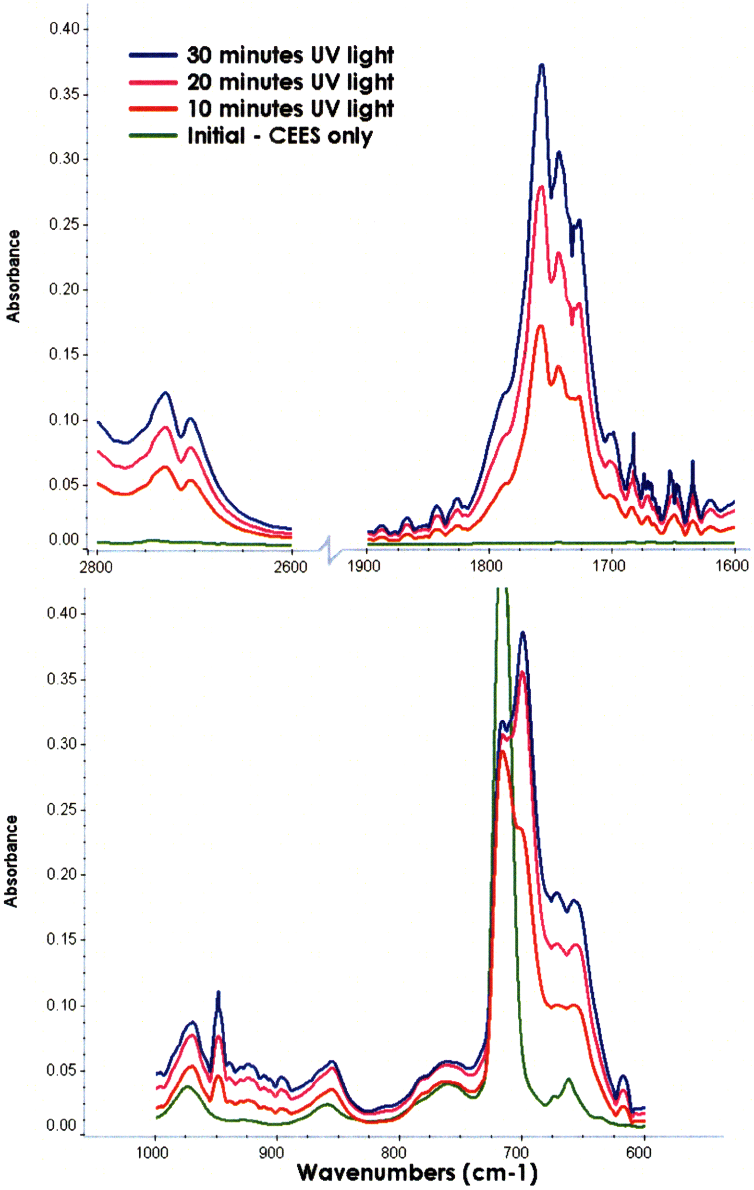

**Figure 22. Photocatalytic confirmation via FTIR**

FTIR spectra collected during a closed cell batch analysis. The cell contained a sample of coated material, equal in size to the exposed surface during permeation testing, and 3 μL condensed CEES. The entire cell was then irradiated by UV light and spectra taken at 10 minute time intervals.

Two broad peaks are observed in the 2750-2700 $cm^{-1}$ range, while a strong triplet centered around 1750 ± 50 wavenumbers is observed to increase as the test proceeds. These suggest the presence of the carbonyl stretching band of acetaldehyde as well as chloroacetaldehyde.[79,80] Neither of these regions exhibit any IR absorption in gaseous CEES. A sharp peak appears at 950 $cm^{-1}$ which is also clearly not present in the initial spectra containing only gaseous CEES. This band is present in an IR-fingerprint of ethylene as the $\nu_7$ band, but may also be a result of chloroethylene present in the vapor.[81] The increase in absorbance at 668 $cm^{-1}$ is indicative of the $\nu_2$ band of carbon dioxide,[82] suggesting the increasing presence of one of the final products throughout the duration of the test. The conclusion can then be drawn that even in a saturated atmosphere the surface of the titania remains active for at least 30 minutes. A weak signal of several peaks is also observed at wavenumbers slightly less than 3000 $cm^{-1}$, similar to those recorded in previous photocatalytic degradation studies,[63] suggesting some HCl to be present in the gas phase. The relative weakness of this signal is not of concern, however, as most of the hydrogen chloride and sulfuric acid generated by the reaction is expected to remain bound to the titania surface. Typically these products can be responsible for the fouling and eventual elimination of the catalytically active sites on the titania surface, however the observed steady increase of several byproducts in the gas phase indicate this has not succeeded in stifling the reaction over the course of this test.

## 2.4 Conclusion

Results presented in the chapter describe a unique way to synthesize and introduce titanium dioxide nanoparticles into a mechanically stable coating capable of the photocatalytic degradation of the chemical warfare agent simulant chloroethyl ethyl sulfide. The entire coating process, from synthesis to deposition, can be conducted at ambient temperatures and moderate pressures, and does not require expensive specialized equipment to produce. The process is readily scalable and can be conducted on substrates of limitless dimension and geometry based on the Spray-LbL method by which the coating is applied. Sample coated plastics have been shown to provide more than 99% protection from a saturated atmosphere of simulant when subjected to ultraviolet radiation with a spectrum resembling that of sunlight. Similarly, the polar ionic complex nature of LbL films allows the material to have much greater water vapor transport properties when compared to inert rubbers capable of similar protective properties. The coating is optically clear and can be deposited on materials without compromising their underlying functionality. Finally, because the titania is deposited as part of an exterior coating there is less risk that superoxide anions developed even under intense UV light will degrade the underlying material. While small portions of the polycation in the film are degraded by the photocatalytic activity of the titania, the mechanical stability of the coating is not compromised.

# 3. Metal Ion Doped Layer-by-Layer Coatings

## Abstract

In this chapter the first substantial difference to be observed between the physics of sprayed and dipped deposition is investigated. Using the Spray-assisted Layer-by-Layer (Spray-LbL) technique, the number of metal counterions trapped within LbL coatings is significantly increased by kinetically freezing the film short of equilibrium, potentially limiting interchain penetration and forcing chains to remain extrinsically compensated to a much greater degree than observed in the traditional dipped LbL technique. The basis for the enhanced entrapment of metal ions such as $Cu^{2+}$, $Fe^{2+}$ and $Ag^{+}$ is addressed, including the equilibrium driving force for extrinsic compensation by soft versus hard metal ions, and the impact of spray-LbL on the kinetics of polymer-ion complexation. These polymer-bound metal ion coatings are also demonstrated to be effective treatments for air filtration, functionalizing existing filters with the ability to strongly bind toxic industrial compounds such as ammonia or cyanide gases, as well as chemical warfare agent simulants such as chloroethyl ethyl sulfide. Future work could extend this method to include other toxic 'soft-base' ligands such as carbon monoxide, benzene, or organophosphate nerve agents.

## 3.1 Introduction

When a polycation and polyanion are alternately adsorbed via the Layer-by-Layer (LbL) process to electrostatically assemble multilayers,[5] the corresponding counterions accompanying the polyelectrolyte chains in solution are freed as polyion contact pairs are formed to create ionically crosslinked thin films. The extent to which this ejection occurs remains heavily debated within the Layer-by-Layer community as researchers argue both for[43,45,83-89] and against[13,49,90-96] counter-anion inclusion as well as for[97,98] and against counter-cation inclusion. In any case the entropically favorable ejection of at least a portion of the small counterions present is crucial to electrostatic self-assembly and leads to thin films suitable for a wide variety of applications, however there are cases in which small metal ion incorporation is a desirable feature. For example, Rubner and Cohen have deposited poly(acrylic acid) (PAA)/poly(allylamine hydrochloride) (PAH) films at low pH conditions, yielding high amounts of free acid groups that can later complex ions which can be reduced to metal nanoparticles.[99] Bruening and coworkers directly adsorbed metal salts of PAA into LbL thin films, from which metal ions were removed after deposition to leave –$COO^-$ vacancies behind in a process known as metal-ion templating.[97,98] In both cases, the extent of metal ion complexation is limited by thermodynamic equilibrium; ions will readily diffuse out of the films if immersed in weakly acidic aqueous solutions, resulting in very small residual ion concentrations.

In this chapter metal ions will be electrostatically bound to a portion of the carboxylic acid side chains of PAA in solution using a method similar to that demonstrated by Bruening and co-workers; however, here we are interested in exploiting the reactivity of metal ions toward toxic ligand molecules, for example $Cu^{2+}$ toward ammonia. For such applications, it is necessary to retain much higher ion concentrations within the layered thin film following assembly. Here we demonstrate that the sprayed variation of the traditional dipped LbL method[30,40,41] can be used to kinetically pin metal ions into polymeric films at much greater than equilibrium concentrations, effectively retaining the ions within the film following assembly. We suggest several thermodynamic based arguments which allow us to incorporate much larger numbers of counter-ions into LbL films than have been previously reported, and means by which the spray assembly method allows the trapping of such ions within the film, providing insight into the physical mechanistic differences between spraying and the traditional dipping techniques. The technique is then extended to include the complexation of the toxic industrial compound hydrogen cyanide using $Fe^{2+}$, and the mustard gas simulant chloroethyl ethyl sulfide using $Ag^{+}$. The efficiency of each ion doped coating is tested as a functionalizing treatment for air-filters.

This unique ion-trapping behavior creates coatings that are highly reactive toward specific chemical ligands. During the 85 years since World War I, which is recognized as the start of the modern era of chemical warfare, the US Army has progressed through a series of improvements to their Nuclear Biological Chemical (NBC) filtration technology.[100] For nearly fifty years the US Army standard filters were based on a coal-based whetlerite carbon known as ASC, impregnated with copper, silver and hexavalent chromium containing compounds.[101] Copper(II) oxide was present to react with toxic vapors such as arsine, chlorine and acid-gas producers such as phosgene, however some of the copper oxide reacted with HCN to form the toxic byproduct cyanogen. To mediate this undesirable reaction a chromium(VI) salt was present to more efficiently react specifically with cyanide compounds. Once hexavalent chromium was designated a hazardous material by the EPA, the cost of disposing of the existing filters dramatically increased, and the Army was forced to switch to ASZ carbon. The new technology relied on the presence of copper, silver, zinc and triethylenediamine (TEDA). Zinc and TEDA function as acid gas sinks to filter out any cyanogen byproducts, while zinc comes with the added bonus of forming a thin shell around the copper granules. Zinc reacts with HCN without the formation of cyanogen compounds, effectively shielding the underlying copper. Unfortunately, upon exposure to humid environments the copper was found to migrate to the external surface, requiring the Army to once again update the filter technology to the ASZM carbon.[102] In its current form this technology relies on the use of a whetlerite carbon matrix impregnated with copper, silver, zinc and molybdenum (to prevent copper migration) metal oxides and salts which can undergo chemical reactions with a variety of chemical warfare agents, aerosols and organic chemicals, and absorb toxic byproducts. Furthermore, recent military focus has broadened not only to include traditional chemical warfare agents but also many Toxic Industrial Chemicals (TIC) recognized as threats to military personnel and HAZ-MAT workers exposed to them. Nanotechnological developments have allowed researchers to propose several improvements to the NBC technology, including the use of zero-valent metal nanoparticles which exhibit increased activity toward contaminant species when compared to metal oxides or metal salts.[103]

Drawing on the state-of-the-art military filtration technique, here we propose a further step toward increased activity, and therefore increased decontamination efficiency, by creating polymeric coatings doped with metal ions in order to bind specific contaminants as metal ion-ligand complexes. The energetic favorability of these complexes, as opposed to zero-valent particles, provides increased reactivity, while the lack of a heterogeneous covalent reaction will eliminate dangerous byproducts which are often as toxic as the original contaminant. The idea of doping polymers with metal ions via ion-beam implantation has been widely investigated in the past,[104,105] however we propose a technique to accomplish the task at room temperatures and moderate pressures which can be used to apply coatings conformally to a wide variety of substrate materials and geometries. Here we demonstrate the validity of our technique using three metals to target two toxic industrial compounds and one chemical warfare agent simulant, but the technique can be extended to a wider variety of compounds in the future.

## 3.2 Experimental

*LbL Solutions:* Poly(acrylic acid, sodium salt) (PAA, MW = 15,000) was purchased from Aldrich and used to make a solution of 20 mM concentration with respect to the repeat unit of PAA. A metal salt was then added to the solution depending on the desired metal ion to be electrostatically attached to the carboxylic pendant groups. For $Cu^{2+}$, copper (II) sulfate pentahydrate (Aldrich), for $Fe^{2+}$, iron (II) chloride (Fluka), and for $Ag^{+}$, silver nitrate (Aldrich) was added. The divalent ions were limited to specific concentrations to avoid precipitation of the polymer chains. The optimal recipes were found to be $y \approx 0.15$ in the case of $Cu^{2+}$ and $y \approx 0.20$ for $Fe^{2+}$, where x, y and z are fractions of the total number of repeat units and sum to one. Since the monovalent $Ag^{+}$ would not be expected to crosslink two adjacent chains it could be added in much larger amounts without precipitation, in this case $y \approx 0.70$.

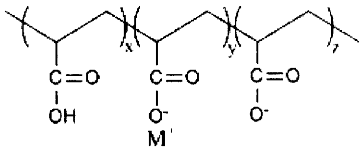

The ratio of x to z was then manipulated by controlling the pH of the PAA-$M^+$ solution. Again $Cu^{2+}$ and $Fe^{2+}$ solutions behaved similarly and were titrated to 5.5 using hydrochloric acid, while $Ag^+$ solutions were titrated to 7.0 in the same manner. Polycationic solutions of poly(allylamine hydrochloride) (PAH, MW = 60,000) were made at a concentration of 20 mM with respect to the repeat unit as well.

*Coating Construction:* Dipped deposition was conducted using a Carl Zeiss HMS DS-50 slide stainer. The silicon substrates were first exposed to the PAH solution for 10 minutes, followed by three rinse steps in Milli-Q water, titrated to pH = 5.5 using hydrochloric acid, for a total of 2 min. It was then exposed to one of the PAA-$M^+$ solutions for 10 minutes and rinsed similarly. The cycle was repeated for the required number of layer pairs. Sprayed coatings were created using an automated Spray-LbL system.[30] Identical polyelectrolyte solutions were delivered by ultrahigh purity Argon gas regulated to 50 psi. PAH was sprayed for 3 s and allowed to drain for 7 s, before spraying with rinse water for 10 s and allowing it to drain for 10 s. The half cycle was repeated for the PAA-$M^+$ solution resulting in a 60 s cycle, while the full cycle was repeated 50 times to create the final coatings tested here. This method allows for conformal multilayer coating of a variety of substrates including but not limited to planar silicon, porous filter paper, and porous Bekipor® stainless steel filter mesh (Bekaert). In the case of porous substrates, the spray of polyelectrolyte solutions is drawn through the substrate by adding a vacuum attachment to the apparatus which is discussed in much greater detail in Chapter 4. Finally, $(PAH/PAA\text{-}Ag^+)_n$ coatings were immediately treated by exposing to a hydrogen atmosphere for 60 minutes to reduce the highly reactive $Ag^+$ ions to more stable $Ag^{(0)}$ nanoparticles, while $(PAH/PAA\text{-}Cu^{2+})_n$ and $(PAH/PAA\text{-}Fe^{2+})_n$ coatings were tested as is. Careful considerations were taken in choosing the combination of polycation and metal-ion to be deposited simultaneously. $Fe^{2+}$ was found to form undesirable ligand-metal complexes with tertiary or quaternary amines, as can be seen in Figure 23, while similar results were observed for $Ag^+$ with secondary or tertiary amines. Poly(allylamine hydrochloride) (PAH), which contains only primary amines was therefore chosen to insure only electrostatic interactions secured the metal ions into the film, allowing them to remain free for further complexation with the desired toxic ligand.

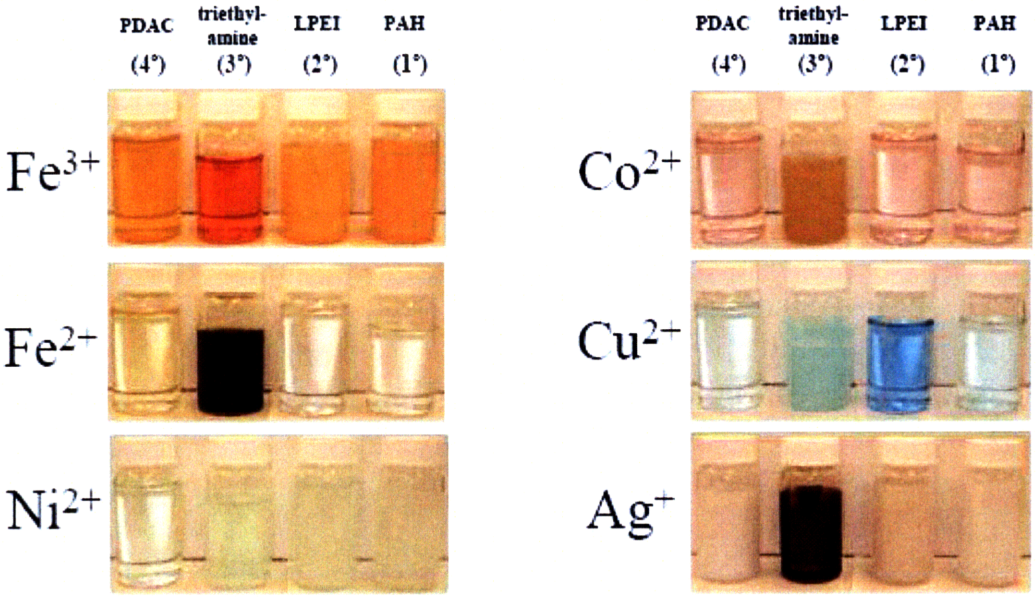

**Figure 23. Ligand-metal complexes with several amines**

Six metal ions, three of which are used extensively in this work, were mixed with primary, secondary, tertiary or quaternary amines to test for complexation. All six metal ions undergo some form of complexation with tertiary amines, while quaternary amines don't complex with anything but $Ag^+$ ions. Primary amines do not complex with $Fe^{2+}$ or $Cu^{2+}$ ions, and only marginally with $Ag^+$ ions.

*Characterization:* Coating thickness was determined using a Tencor P10 Profilometer to drag a stylus across a scored film and record the step height. A stylus tip force of 6 mg was used to avoid film penetration. Film composition was determined using a JEOL JSM-5910 Scanning Electron Microscope equipped with EDX X-ray Spectrometer, and confirmed using a TA Instruments TGAQ50 thermogravimetric analyzer. The oxidation state of metals within the films was determined using a Kratos AXIS Ultra X-ray Photoelectron Spectrometer, while the binding kinetics of contaminant vapors were investigated using a Varian Cary 6000i UV-vis-NIR Spectrophotometer equipped with a 10 cm path length vapor cell. Permeation testing was conducted in a stainless steel cell[31], shown in Figure 16, and the contaminated stream was analyzed using a Gow-MAC Instrument Co. Series 23-550 Total Hydrocarbon Analyzer equipped with a flame ionization detector when detecting chloroethyl ethyl sulfide (CEES), or a Pfeiffer Vacuum Thermostar Mass Spectrometer when detecting ammonia. FTIR testing was conducted using a Nexus 870 FTIR ESP (Thermo Nicolet) using KBr pellets. *Caution:* Samples were challenged using chloroethyl ethyl sulfide (ScottGas), ammonia (Aldrich) and hydrogen cyanide (AirGas) vapors during this testing. All three of these compounds are considered to be toxic industrial compounds, and extreme caution should be exercised when working with them. Only qualified personnel taking appropriate protective measures should attempt to work with these materials.

## 3.3 Results and Discussion

The incorporation of significant amounts of metal counter-ions into multilayered coatings was achieved via the direct assembly of polyion/metal salt complexes of poly(acrylic acid) and poly(allylamine hydrochloride), using the spray LbL approach described in Chapter 1. In each of three metal ion systems, copper, iron, and silver ions were incorporated directly into films at a range of pH and ion concentrations. In the following sections, each of these systems is addressed independently, and a general approach to determining the thermodynamic driving force for maintaining high ion complexation is addressed to gain insight into the non-equilibrium constraints placed upon the system in order to incorporate the large number of reactive ions observed.

### 3.3.1 Copper Binding of Ammonia

According to Pearson's concept of identifying hard- and soft-acids and bases, we expect to see a favorable electrostatic interaction between the soft base $-COO^-$ and the soft acid $Cu^{2+}$.[106] Copper addition will titrate the localized negative charge from a portion of the $-COO^-$ groups dispersed along the PAA backbone depending on the pH of the solution. Therefore it is necessary to carefully control the amount of copper ions introduced to the solution to prevent destabilization and precipitation. Copper in its +2 oxidation state is also a divalent ion capable of binding carboxylate groups between PAA chain segments leading to the cross-linking of chains and network formation. Assuming the degree of ionization of the PAA chains is sufficiently high, most copper ions will exist in this bidentate state.[107,108] The uptake of copper was optimized by adjusting the pH of the solution to 5.5, which agrees very well with previously reported results.[109] During the LbL deposition process, most of the remaining free $COO^-$ groups will form electrostatic interactions with ionized PAH chains to form stable multilayers, but the fate of the copper counterions is somewhat more complicated.

*Counterion Theory:* In the traditional dipped LbL technique small salt counterions accompanying the polymer chains in solution play a very important role during film deposition. The entropic gain realized as extrinsically compensated polyelectrolyte charges (i.e. point charges within the film occupied by a salt counterion)[95,96] eject the small ions in favor of intrinsic compensation by an alternately charged polyelectrolyte is a driving force for film deposition. However, in the presence of sufficiently large salt concentrations it is also a reversible process, known as salt swelling, which can be described physically as a competition for charged sites within the film between bound counterions and alternately charged polyelectrolytes, as well as mathematically by the equilibrium expression:

$$Pol^{-}Pol^{+}{}_{(m)} + M^{+}_{(aq)} + A^{-}_{(aq)} \leftrightarrow Pol^{-}M^{+}{}_{(m)} + Pol^{+}A^{-}{}_{(m)} \qquad \textbf{Eqn. 12}$$

$$K = \frac{[Pol^{-}M^{+}{}_{(m)}][Pol^{+}A^{-}{}_{(m)}]}{[Pol^{-}Pol^{+}{}_{(m)}][M^{+}_{(aq)}][A^{-}_{(aq)}]} \qquad \textbf{Eqn. 13}$$

Here the competition occurs between intrinsically compensated $Pol^{-}Pol^{+}$ sites within the multilayer film and $M^{+}$ or $A^{-}$ ions in solution. This process has been observed experimentally for some LbL systems at very high ionic strength. Considering only counter-cations to simplify the argument, for the example of PAA deposition with sodium counterions, $Pol^{-}$ is the carboxylate ion side chain and $M^{+}$ is the sodium counterion in solution. Here the equilibrium constant favoring sodium occupation of carboxylate sites is on the order of $10^1$-$10^2$.[110] Counterion complexation is relatively weak, allowing incoming polycation chains to displace most of the small ions entropically. Furthermore the practice of briefly rinsing the film in DI water (where $[Na^{+}] \approx 0$) after each deposition step will be sufficient to shift the equilibrium, breaking this weak attraction and ejecting any remaining sodium ions from the surface chains of the final film. For these reasons it has often been reported that only trace amounts of sodium counterions are observed in finished LbL films.[83]

However, previous studies reporting counter-cation ejection have been limited to the study of Period I and II cations.[13] Ions in these Periods, such as $Na^{+}$, exhibit relatively high orbital electronegativity and the absence of easily excitable outer shell electrons. According to Pearson's HSAB system of classifying metals and ligands, these characteristics group them as hard-acids which would not be expected to bond favorably with a soft-base such as the carboxylate ion.[111,112] On the other hand moderate- to soft-acid ions such as $Cu^{2+}$, $Fe^{2+}$ or $Ag^{+}$ with increased size and polarizability, as well as easily excitable d-orbital electrons would exhibit much more favorable interactions. Quantitatively, if the previous example was reconsidered this time with $Cu^{2+}$ counter-ions instead of $Na^{+}$, an increase in equilibrium constant in favor of counterion-ligand complexation to the order of $10^6$-$10^7$ is observed.[113-115] This corresponds to an increase of roughly 5 orders of magnitude in the fraction of counter-ions that can avoid ejection by incoming polyelectrolytes, explaining the incorporation of some residual $Cu^{2+}$ counterions into dipped $(PAA/PAH)_n$ films observed by both Bruening[97] and Caruso[98] in the past.

Having established counterion ejection to be an equilibrium process, it is necessary to describe the route by which that equilibrium is reached. When a charged substrate is exposed to solutions of alternately charged polyelectrolytes via the traditional dipped LbL technique, charged molecules near the surface immediately adsorb, setting up a concentration gradient between the bulk solution and interfacial region near the surface. Polyelectrolyte transport to the surface is limited by diffusion and therefore occurs relatively slowly. As individual molecules arrive at the surface they have the lateral mobility to bind to points of localized charge density as well as to penetrate the surface of the film and interact with previously adsorbed chains. If allowed to proceed to equilibrium during deposition, followed by prolonged rinsing in the absence of salt, this process will enable significant polycation/polyanion complexation, and will liberate all remaining hard-acid counter-cations, or a large portion of any remaining soft-acid counter-cations, depending on the system, resulting in a highly intercalated multilayer film. Alternatively, when a charged substrate is exposed to alternating sprayed mists of polyelectrolyte solutions, the entire surface is simultaneously and uniformly exposed to the bulk polyion concentration. Incoming polyelectrolyte chains are limited in mobility to interact primarily with the opposite charges immediately experienced at the top surface, since over the reduced time frame of spraying chains are not able to sample other arrangements. Conformational differences may also exist due to the convective action of spraying which may force chain spreading while limiting interpenetration. Less opportunity for interaction with underlying chains, and therefore less opportunity to proceed to equilibrium through ejection of counter-ions, would result in a less intercalated film[30] which should contain significantly more small counter-cations particularly in the case when equilibrium favors a strong ligand-metal interaction. Some interdiffusion and thus intrinsic compensation will still occur, but is significantly reduced. The net result is that chains are kinetically trapped in less-than-equilibrium conformations, with lower degrees of polyion complexation and higher numbers of retained polyion-metal ion pairs.

*Characterization of Coatings:* As shown in Figure 24, when identical solutions of PAA-$Cu^{2+}$ and PAH are used, very similar growth rates (i.e. the increase in thickness with each adsorption cycle) are observed independent of the method of deposition chosen. Assuming the ratio of $Cu^{2+}$ to $-COO^-$ in solution is 0.15 and that each copper ion is capable of binding two carboxylate groups at optimal pH, a maximum of 30% of the total carboxylic side chains will participate in $Cu^{2+}$ binding. At pH 5.5 another 20-50% of acid groups will be ionized,[46] and available to participate in electrostatic interactions with the polycation, a fraction which is unaffected by the presence of up to 30% copper.

Similar amounts of electrostatic interaction, and therefore similar growth rates, suggests that the thickness increase due to additional counter-ions in the film is offset by the increased amount of inter- and intra-chain crosslinking induced by the divalent ions, i.e. a fraction of the $Pol^-Pol^+$ crosslinks appear to have been replaced by $Pol^-M^{2+}Pol^-$ crosslinks.[116]

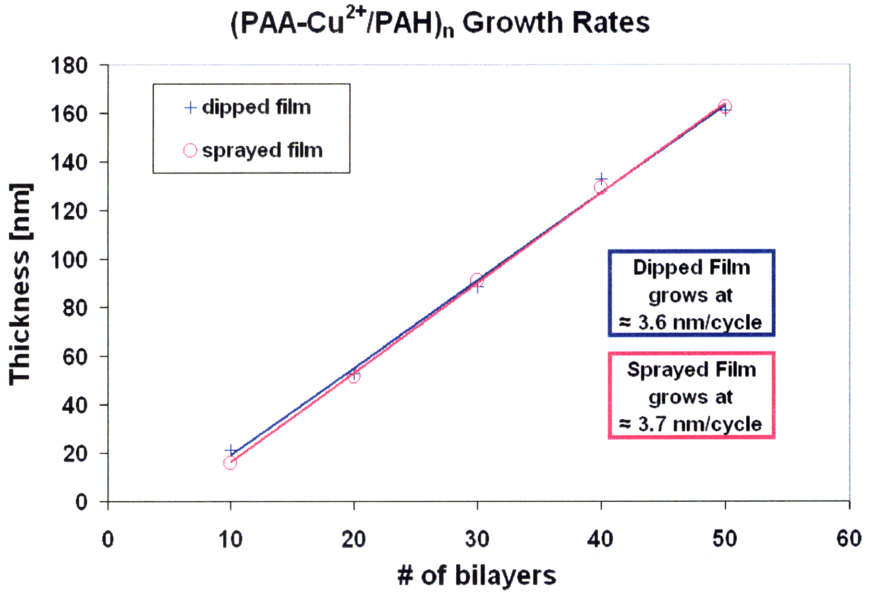

**Figure 24. Dipped versus sprayed growth rates**

Correlation of total film thickness to layer pair number for the (PAA-Cu$^{2+}$/PAH)$_n$ system both by sprayed deposition and dipped evaluated using profilometry. Reported values are averages taken from several data points on a silicon wafer. Both dipped and sprayed films exhibit very similar linear growth rates after 5 deposition cycles.

The decrease in deposition time, by roughly 30-fold when using the Spray-LbL technique, does not affect the rate of deposition. As anticipated, the presence of some $Cu^{2+}$ counterion is observed, via elemental analysis in Figure 25, in dipped films when the PAA-$M^+$ interaction is strengthened by using the soft-acid counter-ion $Cu^{2+}$. Coatings created via the Spray-LbL technique include significantly larger amounts of $Cu^{2+}$ as counterions that appear to be kinetically frozen within the polyelectrolyte matrix. Quantitatively, the composition of the sprayed film contains more than 12 wt% copper, as can be seen in Figure 26, while otherwise similar dipped films contain less than 5 wt%. Complexing copper to PAA chains shifts the decomposition range to higher temperatures,[109] clearly seen in the progression from no copper content in the $(PAA/PAH)_{50}$ control film, to $\approx$ 5% copper in the dipped, and 12% in the sprayed LbL films.

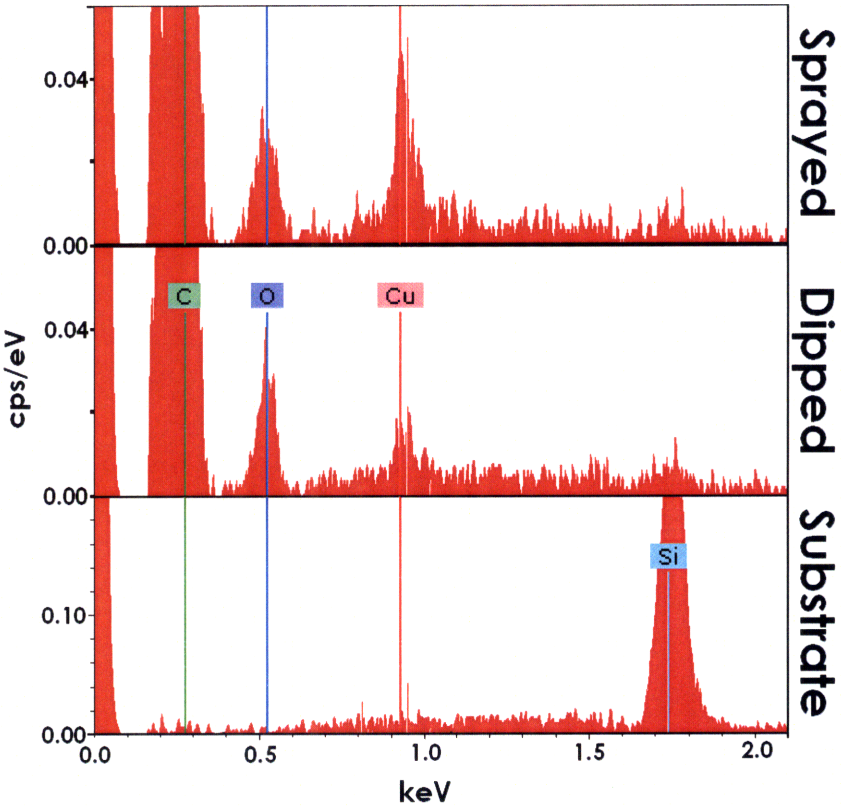

**Figure 25. Increased Cu$^{2+}$ counter-ion content: EDX**

Elemental Analysis of (PAA-Cu$^{2+}$/PAH)$_{50}$ coatings created both by sprayed deposition and dipped using a 3.0 keV beam potential. For clarity the carbon, oxygen and copper signals identified in the film, as well as the silicon signal from the underlying substrate have been labeled. The carbon peak has also been truncated to magnify the oxygen and copper peaks.

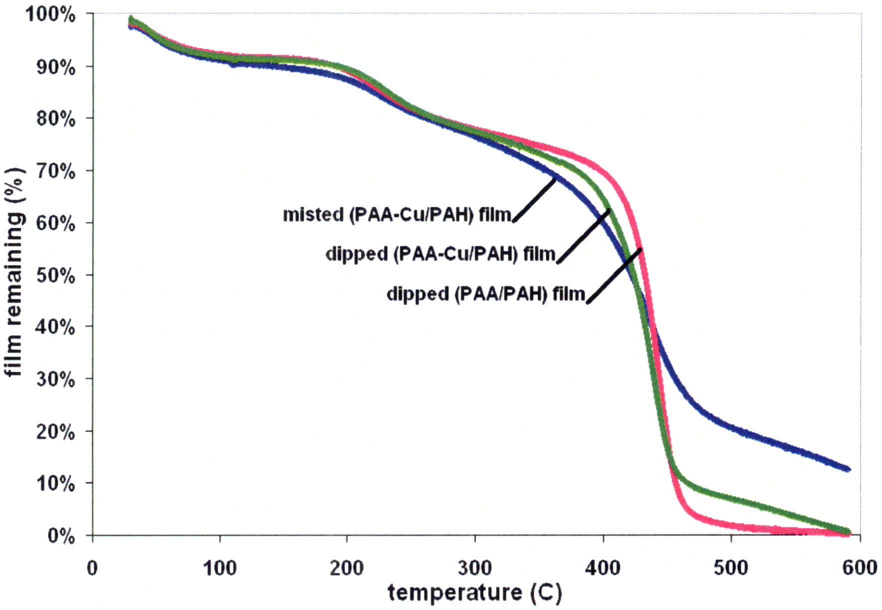

**Figure 26. Increased $Cu^{2+}$ counter-ion content: TGA**

Thermogravimetric Analysis of $(PAA\text{-}Cu^{2+}/PAH)_{50}$ coatings created both by sprayed deposition and dipped. Films were deposited on silicon substrates and scraped free to conduct TGA.

Finally, the observation of the Cu $2p_{3/2}$ and Cu $2p_{1/2}$ peaks in Figure 27 with measured binding energies slightly greater than 930 and 950 eV confirm the presence of copper in the $Cu^{2+}$ state in the $(PAA/PAH)_n$ coatings.[117] Therefore, the spray deposition technique is able to introduce significantly more copper into the polyelectrolyte film than the traditional dipped technique, and the copper that is introduced remains in the oxidized $Cu^{2+}$ form.

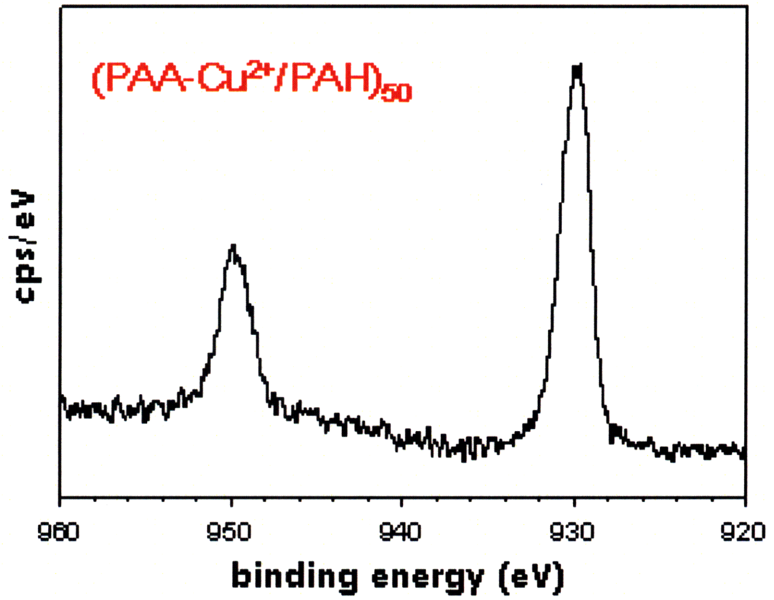

**Figure 27. Increased $Cu^{2+}$ counter-ion content: XPS**

X-ray Photoelectron Spectrometry of $(PAA\text{-}Cu^{2+}/PAH)_{50}$ coatings created by sprayed deposition.

*Reactivity:* Having established that copper ions are electrostatically attached to $-COO^-$ groups within a film assembled by electrostatic interactions, it is necessary to determine if the copper present in the film is free to undergo further reaction. In the presence of excess ammonia, the tetraamminediaquacopper(II) complex ion, $[Cu(NH_3)_4(H_2O)_2]^{2+}$, is generated as d-orbital electrons from the $Cu^{2+}$ ion are donated to the antibonding orbitals of the ammonia and water ligands.

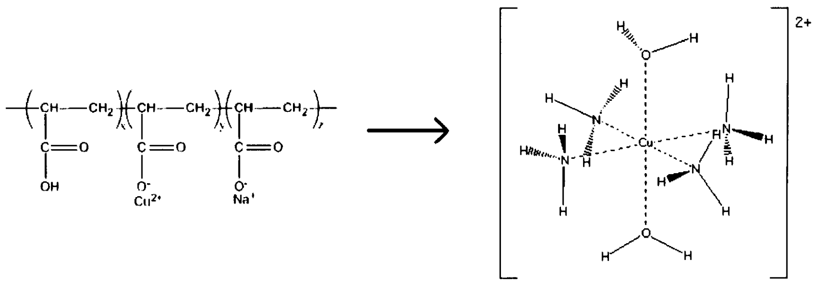

This reaction is an energetically favorable process; however it must be sufficiently favorable to overcome the electrostatic interactions binding copper ions to PAA chains in the film, as well as rapid enough to work as a filtration technique. A (PAA-$Cu^{2+}$/PAH)$_{50}$ coating was deposited on a quartz wafer and mounted in the vapor cell of a UV-Vis Spectrometer. Initial absorbance at 261 nm in Figure 28 confirms the presence of PAA•$Cu^{2+}$ chelated between two carboxyl groups.[115] Upon exposure to $NH_3$ vapor this band immediately disappears, and does not reappear even 20 minutes after the vapor pulse has occurred.

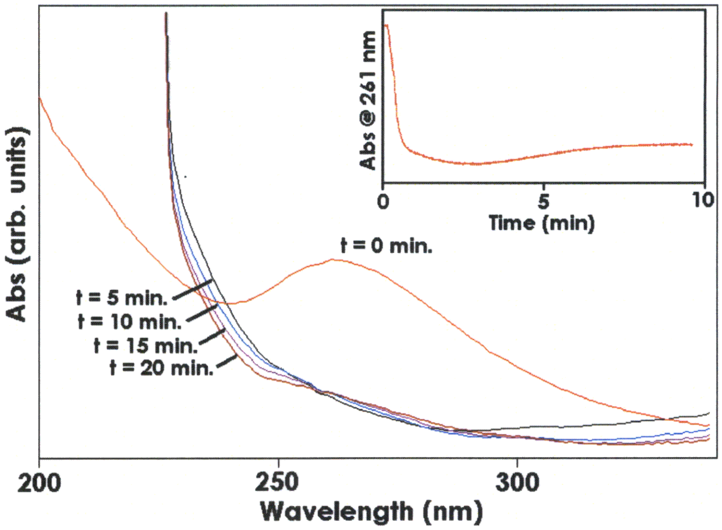

**Figure 28. Reactivity of $Cu^{2+}$ doped films: UV-Vis**

UV-Vis absorption of a $(PAA\text{-}Cu^{2+}/PAH)_{50}$ coating on quartz exposed to a saturated vapor of ammonia. Samples were taken initially and at 5, 10, 15 and 20 minutes after the stimulus was injected. **Inset:** Real time analysis of the same test recording only adsorption at $\lambda = 261$ nm, indicating the speed at which the electrostatic- to ligand-interaction exchange occurs.

**Figure 29. Change in polyelectrolyte complex color with ammonia**

The polyelectrolyte complex generated by mixing PAA-$Cu^{2+}$ and PAH is initially light blue (left) due to the visible spectrum absorption of the PAA-$Cu^{2+}$ bond. Upon exposure to ammonia vapor, the deep purple of the $[Cu(NH_3)_4(H_2O)_2]^{2+}$ complex ion is clearly observed (right).

A real time kinetic study of absorbance at 261 nm indicates that the elimination of this peak upon exposure to ammonia occurs very rapidly, within the first 30 seconds. This suggests the PAA-$Cu^{2+}$ complex has been disrupted throughout the film both rapidly and thoroughly. Visually a striking change in polyelectrolyte complex color can be observed in Figure 29. Further investigation of the film both before and after exposure to ammonia vapor using infrared radiation yields insight to the exchange taking place. In Figure 30(a) the observed broadening of the peak around 1550 $cm^{-1}$ is due to counterion-induced changes in the energy of the $-COO^-$ stretch as a result of $Cu^{2+}$ ions.[118] Upon exposure, this $\nu(COO^-)$ peak is clearly sharper in Figure 30(b) suggesting the ejection of the $Cu^{2+}$ ions from the $COO^-$ groups. Simultaneously the large increase around 1410 and 1450 $cm^{-1}$ is a result of $Cu^{2+}$-ammonia adsorption[119] Using molecular dynamics simulations it is possible to predict the infrared vibrational frequencies of the $[Cu(NH_3)_4(H_2O)_2]^{2+}$ ion as shown in Table 1.[120] The peak at 1450 cm$^{-1}$ in Figure 30 is thus assigned to symmetric deformation of the $H_2O$ molecules acting as ligands in the complex ion. This technique also predicts a strong peak due to $NH_3$ rocking at lower frequencies which appears around 800 cm$^{-1}$ in the coating.

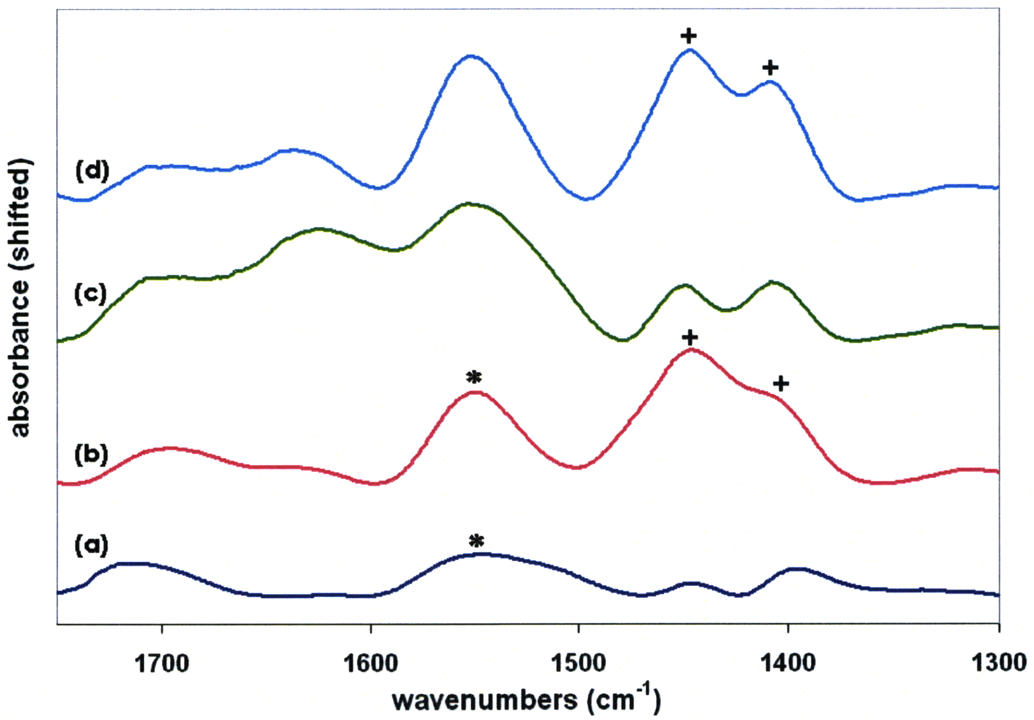

**Figure 30. Reactivity of $Cu^{2+}$ doped films: FTIR**

Infrared absorption of **(a)** (PAA-$Cu^{2+}$/PAH)$_{50}$ coating on silicon, **(b)** exposed to ammonia vapor, **(c)** soaked 60 minutes in DI water, and finally **(d)** re-exposed to ammonia vapor. Peaks associated with the –$COO^-$ stretch are indicated by (*) while those associated with $Cu^{2+}$-ammonia adsorption are indicated with (+).

| frequency (cm$^{-1}$) | normalized intensity | assignment |
|---|---|---|
| 3987 | 1.0000 | $H_2O$ asymmetric deformation |
| 1450 | 0.7497 | $H_2O$ symmetric deformation |
| 1140-1150 | 0.7098 | $NH_3$ symmetric deformation |
| 3780-3800 | 0.3460 | $NH_3$ asymmetric deformation |
| 545-567 | 0.2131 | $NH_3$ rocking |
| 1632-1636 | 0.1494 | $NH_3$ asymmetric deformation |

**Table 1. Simulated infrared vibrational frequencies of the $[Cu(NH_3)_4(H_2O)_2]^{2+}$ complex ion**

A coating was then applied to an off-the-shelf stainless steel filter mesh appropriate for either air or water filtration. In an effort to maximize the surface area, thus increasing reactivity, a thin coating only 15 bilayers thick was applied to the filter using a vacuum modified version of the Spray-LbL technique reported in Chapter 1. In this application a pressure gradient was induced across the filter mesh using a vacuum pump to draw sprayed solutions through the filter, enabling the conformal coating of the interstices of the substrate; a technique which will be discussed in much greater detail in the next chapter. The filter samples were then dried and mounted for testing in a stainless steel test cell designed for mass transfer quantification with acutely toxic chemicals.[31] The effluent concentration of ammonia vapor was monitored as 1 mL of ammonium hydroxide was introduced into the vapor space upstream of the filter. The resulting profiles observed when an as-received filter is challenged as well as when an identical filter treated with a $(PAA\text{-}Cu^{2+}/PAH)_{15}$ coating is used can be seen in Figure 31.

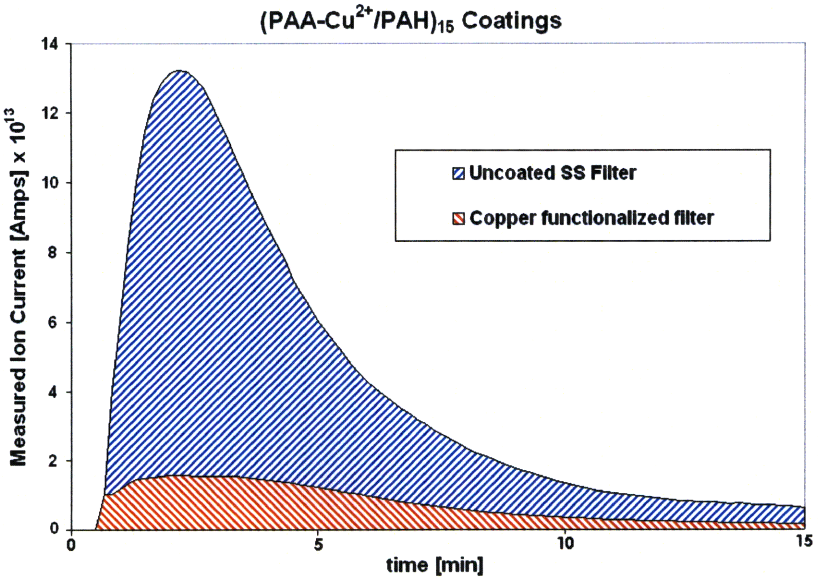

**Figure 31. Reactivity of Cu$^{2+}$ doped films: Permeation Test**

Ion Current recorded by a Mass-Spectrometer monitoring the effluent concentration of ammonia downstream of a filter mesh. In one case an untreated 'off the shelf' air filter is challenged. Subsequently, an identical filter is treated with a (PAA-Cu$^{2+}$/PAH)$_{15}$ coating and challenged with the same dosage of saturated ammonia vapor. Ammonia was introduced to the vapor space at time 0 min.

The pulse of ammonia vapor (approximately 0.012 mol $NH_3$) was made intentionally large enough to see the effects of saturation on the treated filter. Within the first few seconds of exposure the capacity of the Cu$^{2+}$ ions is exhausted as the coating binds more than 80% of the vapor dose. Since the coating is ultra-thin, the pores have not been occluded and the remainder of the mass transfer occurs as if the filter were untreated. Even when subjected to a saturated ammonia vapor the filter operates very efficiently, while FTIR absorption identical to Figure 30(b) is observed several weeks after exposure indicating negligible desorption of ammonia over time.

*Regeneration of films:* Investigation into the regeneration of ion containing coatings is of interest for several applications, and gives insight into the various interactions taking place within the film. Although the ejection of $Na^+$ counterions by $H^+$ ions is expected to occur when films are soaked in DI water (the protonation constant for PAA in the presence of hard-acid cations such as $Na^+$ is ~ $10^5$),[110] the ejection of $Cu^{2+}$ ions by $H^+$ via the reaction

$$(RCOO)_2Cu_{(m)} + 2H^+_{(aq)} \leftrightarrow Cu^{2+}{}_{(aq)} + 2RCOOH_{(m)} \qquad \textbf{Eqn. 14}$$

is significantly less favorable with $K_2 \sim 10^2$. Bruening and coworkers[97] have shown that increasing $[H^+]$ and soaking (PAA-$Cu^{2+}$/PAH) films in acidified water, pH 3.5 or lower, results in the ejection of copper ions. Therefore, in the interest of retaining the copper ions in the film for future use the following test will be performed in neutral pH DI water. Upon soaking in DI water for 60 minutes, Figure 30(c) shows decrease of the absorbance bands at 1410 and 1450 $cm^{-1}$ to levels observed in the original film. The peak intensities have not returned completely to those observed initially, indicating some irreversibility in the process. These peaks were attributed previously to the presence of the $[Cu(NH_3)_4(H_2O)_2]^{2+}$ ion in the film, the reverse complexation of which by rinsing may or may not have removed the copper ions as well. However, re-exposure to ammonia vapor in Figure 30(d) shows the appearance of these absorption bands once again to the degree observed during the initial exposure indicating the presence of roughly the same quantity of copper ions.

As ammonia vapor comes into contact with the initial film, $Cu^{2+}$ ions held electrostatically into the film undergo a swap in lieu of the more energetically favorable $[Cu(NH_3)_4(H_2O)_2]^{2+}$ ion, leaving $-COO^-$ vacancies in the film. The complex ion formed has the same positive charge as the original copper ion, and is held electrostatically by the nearby negative carboxylate group. When soaked in DI water over time, many of the ammonia ligands are able to solubilize and escape the metal-ligand interaction, allowing the copper ion to reverse the exchange and return to the nearby carboxylate groups as PAA-$Cu^{2+}$ complexes. This process takes time, and not all ligands will undergo solubilization in water, so it is observed that some complex ions remain bound to the film even after 60 minutes of soak.

It should be noted that the metal counterion - carboxylate bonds are sufficiently stable in the electrostatically assembled films to withstand de-ionized water soak overnight (Figure 32). However, as expected from the previous discussion the ions can be removed from the sprayed films by driving the polyanion/polycation complexation toward equilibrium. As shown in Figure 33, prolonged soaking in 0.5 M NaCl salt solution promotes structural rearrangement allowing positive groups on PAH chains to find carboxylate groups on the PAA chains, thereby ejecting $Cu^{2+}$ ions entropically and reducing the concentration of $Cu^{2+}$ ions in the film. Likewise, if 0.5 M $CuSO_4$ solution is used instead the induced rearrangements occur in the presence of elevated $Cu^{2+}$ concentrations. As discussed previously the carboxylate and $Cu^{2+}$ interact much more favorably than do the $Na^+$ ions in the previous example, and the loading of $Cu^{2+}$ counterions in the film appears to increase slightly.

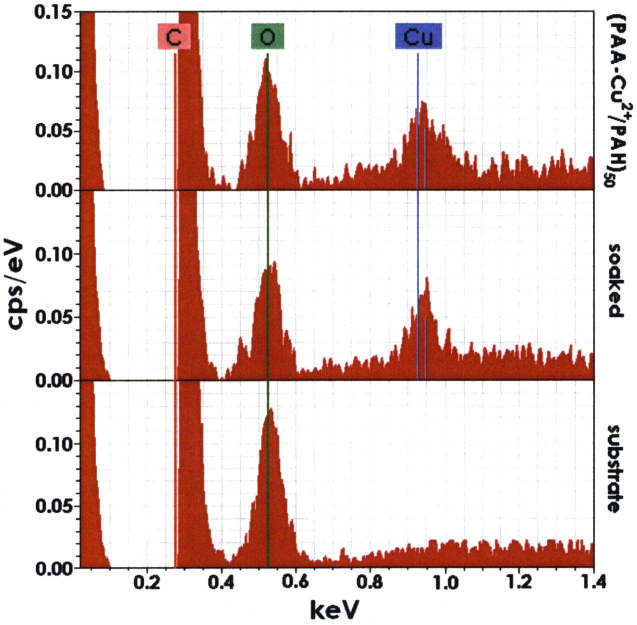

**Figure 32. Extended DI water soak**

Elemental Analysis of (PAA-$Cu^{2+}$/PAH)$_{50}$ coatings created by sprayed deposition on filter paper to eliminate silicon signals using a 5 keV beam potential. For clarity the carbon, oxygen, and copper signals identified in the film have been labeled. The carbon peak has also been truncated to magnify the other peaks. Data shown (from top): as-deposited coating, coating soaked in DI water overnight, and untreated filter paper.

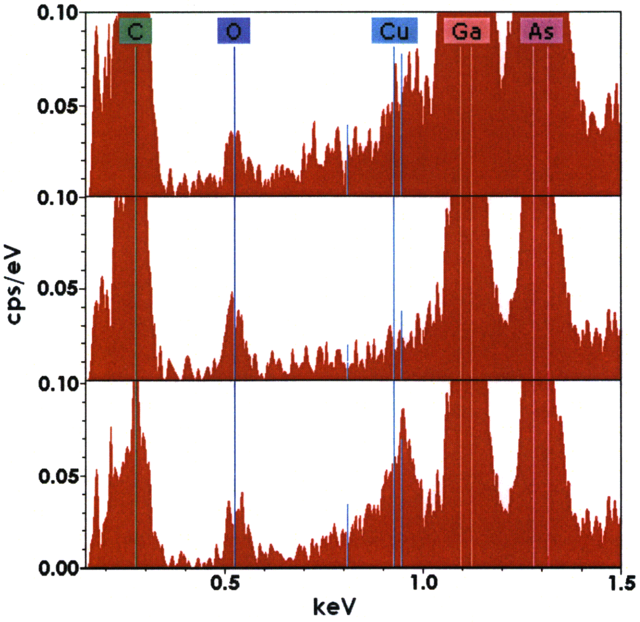

**Figure 33. Extended salt water soak**

Elemental Analysis of (PAA-$Cu^{2+}$/PAH)$_{50}$ coatings created by sprayed deposition on GaAs wafers (to eliminate silicon signals) using a 3 keV beam potential. For clarity the carbon, oxygen, and copper signals identified in the film have been labeled. Data shown (from top): as-deposited coating, coating soaked in 0.5 M NaCl solution overnight, and coating soaked in 0.5 M $CuSO_4$ solution overnight.

### 3.3.2 Iron Binding of Hydrogen Cyanide

*Characterization of Coatings:* Although they have not been reported elsewhere, the creation of (PAA-$Fe^{2+}$/PAH)$_n$ coatings is also possible using this technique. $Fe^{2+}$, like $Cu^{2+}$, is categorized as a moderate to soft-acid according to Pearson, and can undergo favorable interactions with the carboxylate groups present in the PAA chain. Furthermore, the flexibility of using polymer bound metal ions for toxic chemical filtration can again be demonstrated, this time toward an acid gas since $Fe^{2+}$ is capable of chelating six cyanide groups as the hexacyanoferrate(II) complex ion, accompanied by the distinct color change displayed in Figure 34.

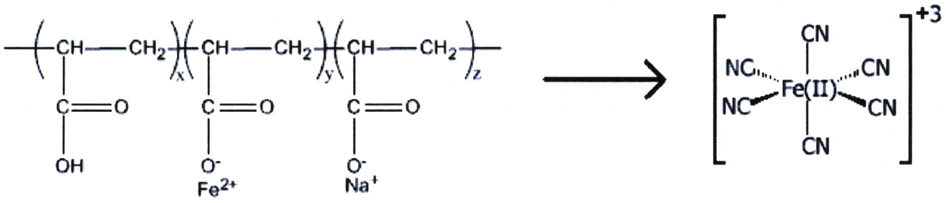

In its +2 oxidation state iron is capable of crosslinking PAA chains, thus the ratio of $Fe^{2+}$ to $-COO^-$ was found to be limited to 0.20. The solution pH was also reduced to 5.5 to optimize iron uptake[109] before coating deposition. Elemental Analysis, in Figure 35, confirms the presence of iron in the film while the observation of the Fe $2p_{3/2}$ and Fe $2p_{1/2}$ peaks in Figure 35(inset) with measured binding energies at 708.3 (shoulder at 711.9) and 721.3 eV (shoulder at 724.9) confirm the presence of $Fe^{2+}$ in the $(PAA/PAH)_n$ coatings.[121]

**Figure 34. Change in polyelectrolyte complex color with hydrogen cyanide**

The polyelectrolyte complex generated by mixing PAA-$Fe^{2+}$ and PAH is initially light orange (left) due to the visible spectrum absorption of the PAA-$Fe^{2+}$ bond. Upon exposure to hydrogen cyanide vapor, the dark green of the $[Fe(CN)_6]^{4-}$ complex ion is clearly observed (right).

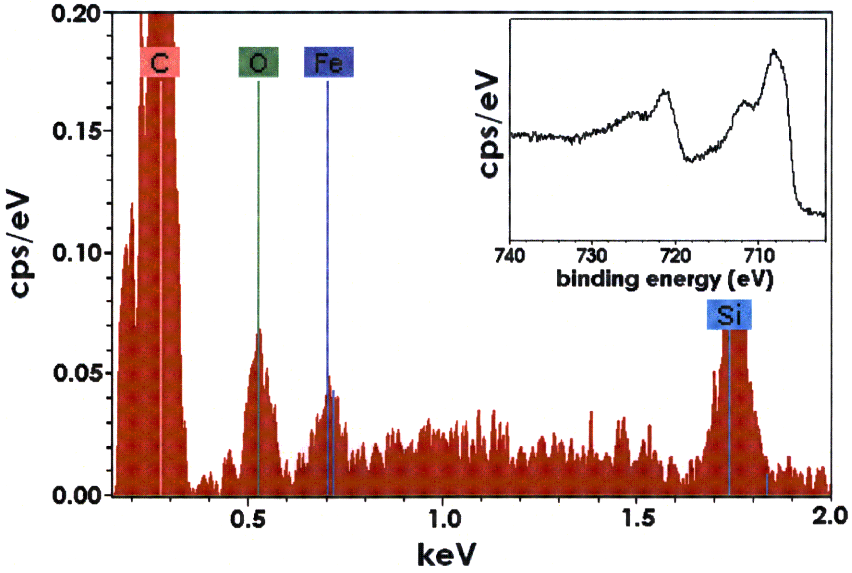

**Figure 35. Increased $Fe^{2+}$ counter-ion content: EDX and XPS**

Elemental Analysis of $(PAA\text{-}Fe^{2+}/PAH)_{25}$ coatings created by sprayed deposition using a 2.5 keV beam potential. For clarity the carbon, oxygen and iron signals identified in the film, as well as the silicon signal from the underlying substrate have been labeled. The carbon peak has also been truncated to magnify the oxygen and iron peaks. **Inset:** X-ray Photoelectron Spectrometry of $(PAA\text{-}Fe^{2+}/PAH)_{25}$ coatings created by sprayed deposition.

*Reactivity:* In order to form a coordinate bond with a soft metal ion a good ligand must have a lone pair of electrons which it can donate much as a Lewis base does. It is therefore the cyanide ion $CN^-$ which acts as a ligand in the $[Fe(CN)_6]^{4-}$ complex, not the neutral hydrogen cyanide. Hydrogen cyanide exists in the vapor phase but the cyanide ion is only observed if the vapor finds moisture and can dissolve. This limits the applications of the $(PAA\text{-}Fe^{2+}/PAH)_n$ coating to cases of air filtration under nearly saturated humidity or water filtration. As the vapor test cell used for this work is only equipped to handle air filtration, the following reactivity tests will be conducted as batch systems in a closed chamber saturated with water vapor from a nearby hot plate. The coated substrate is then subjected to hydrogen cyanide vapor which upon reaching the damp substrate ionizes to form the reactive ligand $CN^-$. For comparison the full IR-spectrum scan of a $(PAA\text{-}Fe^{2+}/PAH)_{50}$ coating before and after exposure to hydrogen cyanide vapor can be seen in Figure 36, with the only difference being an absorption band at 2070 $cm^{-1}$. Molecular dynamics simulations of the $[Fe(CN)_6]^{4-}$ ion indicate only one appreciable vibrational mode, at 2300 $cm^{-1}$ (See Table 2). The experimentally observed peak at 2070 $cm^{-1}$ is therefore assigned to triple bond stretching of the cyanide groups in the complex ion which has been shifted to slightly lower frequencies as a result of interaction with the film. In this case the complex ion is of opposite charge to the original $Fe^{2+}$, suggesting the complex is not held electrostatically into the film. The complex ion remains bound in similar quantities even several days after the sample is taken, but the nature of the interaction will require further investigation.

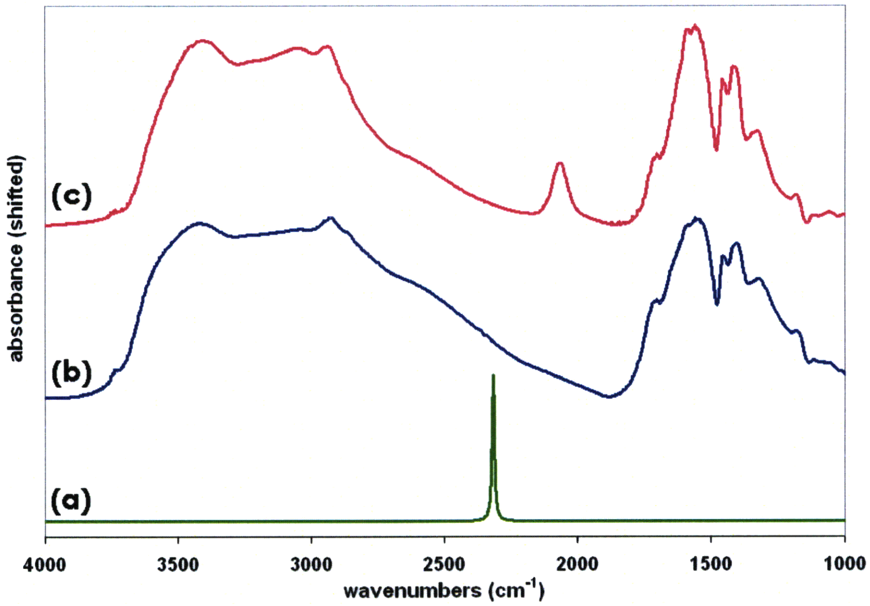

**Figure 36. Reactivity of Fe$^{2+}$ doped films: FTIR**

(a) Infrared absorption spectra of the hexacyanoferrate(II) complex ion as generated using molecular dynamics. Infrared absorption of (b) (PAA-Fe$^{2+}$/PAH)$_{50}$ coating on silicon, and (c) the coating exposed to hydrogen cyanide vapor in 100% relative humidity.

| frequency (cm$^{-1}$) | normalized intensity | assignment |
|---|---|---|
| 2316 | 1.0000 | C≡N stretching |
| 573 | 0.0560 | Fe-C≡N bending |
| 391 | 0.0406 | Fe-C≡N bending |

**Table 2. Simulated infrared vibrational frequencies of the [Fe(CN)$_6$]$^{4-}$ complex ion.**

### 3.3.3 Silver Binding of CEES

*Characterization of Coatings:* Finally, the capabilities of this technique to bind and filter more complex molecules will be demonstrated using a less toxic simulant for mustard gas, chloroethyl ethyl sulfide or CEES. The highly polarizable nature, low electronegativity, and absence of easily excitable outer-shell electrons of the sulfur atom in the center of CEES cause the molecule to behave like a soft-base. CEES is a particularly relevant analog compound to test in this case, as HD mustard gas contains the same sulfur center. In the presence of a soft-acid CEES has been shown to form stable complexes with silver ions in organic solvents.[122] Military efforts have even been made to impart anti-vesicant properties to cellulosic fabrics by treating them with solutions of anthranilic acid and silver salts,[123,124] however mechanical stability of the treatment was poor. To overcome this shortcoming we have introduced silver ions into $(PAA/PAH)_n$ films. Rubner and coworkers have reported the synthesis of silver nanoparticles by submersing finished $(PAA/PAH)_n$ films in silver salt solutions followed by reduction in a hydrogen atmosphere,[99] but in keeping with the theme of this research silver ions were complexed first with PAA chains in solution. The monovalent nature of silver ions allows for a much greater degree of complexation without the risk of uncontrollable crosslinking.[108] In this case the ratio of $Ag^+$ to $-COO^-$ was found to be limited to 0.70, after which the solution pH was reduced to 7.0 before deposition versus PAH. Elemental Analysis, shown in Figure 37, confirms the presence of silver in the resulting film.

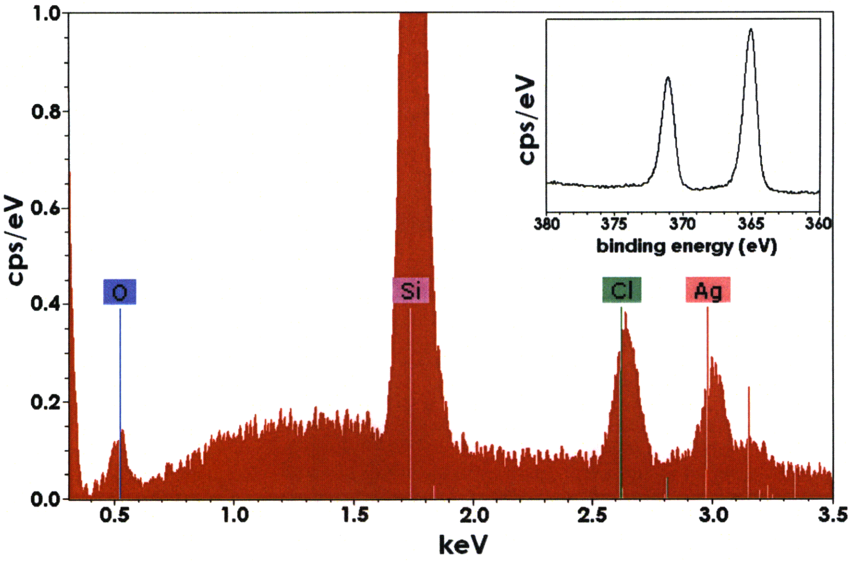

**Figure 37. Increased $Ag^+$ counter-ion content: EDX and XPS**

Elemental Analysis of $(PAA\text{-}Ag_{(s)}/PAH)_{50}$ coatings created by sprayed deposition using a 5 keV beam potential. For clarity the oxygen, chlorine and silver signals identified in the film, as well as the silicon signal from the underlying substrate have been labeled. The silicon peak has also been truncated to magnify the other peaks. **Inset:** X-ray Photoelectron Spectrometry of $(PAA\text{-}Ag_{(s)}/PAH)_{50}$ coatings created by sprayed deposition.

As deposited, the $(PAA\text{-}Ag^+/PAH)_n$ films were found to be particularly susceptible to reaction with atmospheric oxygen, forming the undesirable silver oxide. In order to preserve the silver reactivity toward CEES the resulting films were treated in a hydrogen atmosphere to reduce the silver to zero-valent nanoparticles. The observation of the Ag $3d_{3/2}$ and Ag $3d_{5/2}$ peaks in Figure 37(inset) with measured binding energies at 371 and 365 eV confirm this reduction to $Ag^{(0)}$,[125,126] while TGA indicates the final film contains ≈ 50 wt% silver.

*Reactivity:* The coating was applied to an off-the-shelf stainless steel filter mesh using the vacuum assisted Spray-LbL technique. After drying and hydrogen treatment the samples were mounted in the stainless steel test cell, and the effluent concentration of CEES vapor was monitored as a burst of CEES was introduced into the vapor space upstream of the filter. The resulting profiles observed when an as-received filter is challenged as well as when an identical filter treated with a $(PAA\text{-}Ag^{(0)}/PAH)_{15}$ coating is used can be seen in Figure 38. The burst of contaminant was made intentionally large enough to see the effects of saturation on the treated filter and demonstrates the high rate at which the coating responds. The 100 ppm dosage of simulant is more than 5 times the typically reported battlefield concentration. Even in a 'worst case' scenario, within the first few seconds of exposure the capacity of the evenly distributed silver nanoparticles is exhausted as the film binds almost 80% of the vapor dose. With only 15 bilayers of coating in place the normal flow rate of clean air through the filter is unaffected.

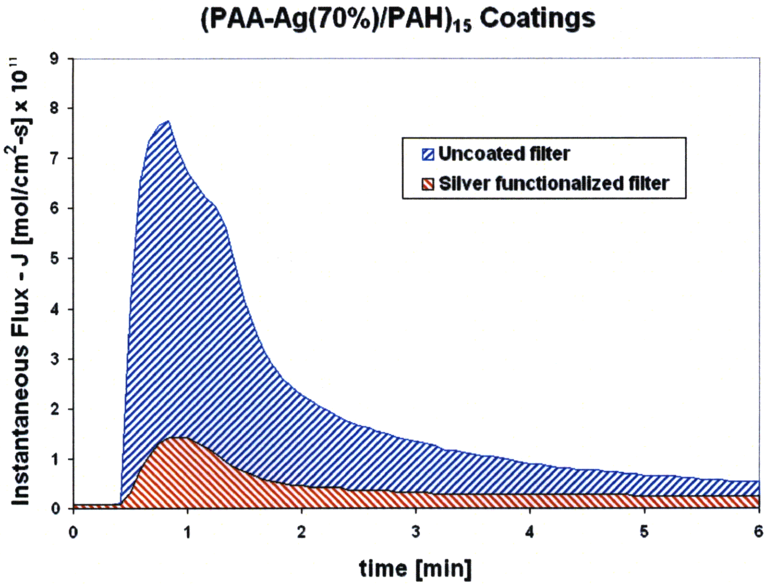

**Figure 38. Reactivity of $Ag^+$ doped films: Permeation Test**

Mass flux recorded by a Total Hydrocarbon Analyzer FID monitoring the effluent concentration of CEES downstream of a filter mesh. In one case an untreated 'off the shelf' air filter is challenged. Subsequently, an identical filter is treated with a (PAA-$Ag_{(s)}$/PAH)$_{15}$ coating and challenged with the same dosage of saturated CEES vapor.

## 3.4 Conclusions

The work described in this chapter presents the first in depth investigation into the physics of sprayed deposition, giving us insight into the subtle differences between it and the traditional dipped technique. The Spray-LbL technique is capable of increasing the number of metal counterions present in an LbL film by minimizing interlayer penetration of surface chains, thus freezing the film short of equilibrium and causing chains to remain extrinsically compensated to a much greater degree than observed in the traditional dipped LbL technique. Appropriate selection of soft-acid metals make it possible to dope

$(PAA/PAH)_n$ films as much as 12wt% with divalent counter-cations such as $Cu^{2+}$ and $Fe^{2+}$, or as much as 50% or higher when using monovalent ions such as $Ag^{+}$. These electrostatically bound coatings have been shown to be effective treatments for air filtration; functionalizing existing filters with the ability to strongly bind toxic industrial compounds such as ammonia or cyanide, as well as chemical warfare agent simulants such as chloroethyl ethyl sulfide. Based on results collected during this research future work could extend this method to include other soft-base toxic ligands such as carbon monoxide, benzene, or organophosphate nerve agents.

# 4. Asymmetric Functionalization via Spray-LbL

## Abstract

As engineers strive to mimic the form and function of naturally occurring materials with synthetic alternatives, the challenges and costs of processing often limit creative innovation. In this chapter we describe a powerful yet economical technique for developing multiple coatings of different morphology and function within a single textile membrane, allowing scientists to engineer the properties of a material from the nanoscopic level in commercially viable quantities. By simply varying the flow rate of charged species passing through an electrospun material during spray-assisted Layer-by-Layer (Spray-LbL) deposition, individual fibers within the matrix can be conformally functionalized for ultra-high surface area catalysis, or bridged to form a networked sublayer with complimentary properties. Exemplified here by the creation of selectively-reactive gas purification membranes, the myriad applications of this technology also include self-cleaning fabrics, water purification, and protein functionalization of scaffolds for tissue engineering.

## 4.1 Introduction

Naturally occurring membranes, such as those found in plants, cell walls and organs including the epidermis and intestinal wall, derive their ability to segregate two different environments largely from the asymmetry established by their protein constituents[127,128]. Instead of functioning as a uniform barrier, the cross section of these membranes varies according to their purpose, allowing interior and exterior portions of the membrane to serve very different roles. Segregation of structure is also observed in porous polymer membranes, where a thin effective separation layer is formed at the upstream surface of the membrane, while the bulk material remains porous and less densely packed[129]. Although identical in chemical composition, asymmetric arrangement of two morphologies provides the membrane with mechanical robustness while separation is regulated predominantly by the thin barrier layer of material near the surface. Aside from mechanical integrity, however, the phase inversion technique used to generate asymmetric polymer membranes does not introduce functional activity to the bulk matrix, thereby underutilizing the full potential of the substrate material. Here we present a novel process capable of two distinct flow rate-dependent modes of electrostatic deposition by which multiple functionalities can be introduced into a single engineered textile. Similar to the way many naturally occurring membranes simultaneously regulate mass transfer and undergo chemical reactions with solute molecules, this technique allows portions of the textile to act as an inert barrier while the bulk material acts as a high surface area scaffold capable of a wide variety of functionalities.

The Layer-by-Layer (LbL) assembly technique enables the deposition of ultrathin uniform films via the sequential electrostatic deposition of charged polymers[5,7,13], nanoparticles[3,14,73,74], biological templates[130], or biologically active species[19]. An inherently charged substrate is serially exposed to solutions of oppositely charged species, which adsorb to the developing film at rates that allow nanometer-scale control of the film thickness[23]. In recent years, an extension of this technique has been developed by which solutions of charged species are sprayed onto the desired substrate[30,40,41]. Similar to the traditional dipping process, assembly occurs via electrostatic interactions between areas of local charge density on oppositely charged species, but process times can be reduced more than 25 fold by convectively transporting charged species to the surface. Planar non-porous substrates such as silicon and glass are readily coated by either technique and, when exposed to similar solutions, exhibit ostensibly similar growth rates and final film properties[30,40]. Electrospun fibers enable the generation of porous polymer scaffolds which can be tuned for fiber size and surface area[131] and chemically modified using a number of methods[132-134]. By drawing a pressure gradient across porous substrates during the Spray-LbL process[32], we have found highly conformal coatings can be developed on individual fibers, wires, or pores throughout the thickness of the bulk porous substrate. This process retains the flexibility, speed and ambient processing conditions that make Spray-LbL an attractive deposition technique, and is capable of creating exceptionally high surface area coatings; applications of relevance include self-cleaning photocatalysis[132,135,136], conformal surface passivation[137-140] for corrosion protection, or biocatalytic membranes for pharmaceutical or biofuel applications. Pursuant to the goals of this thesis, asymmetrically functionalized electrospun materials will be demonstrated as a highly reactive, yet breathable, means of protection against toxic vapors and chemical warfare agents.

## 4.2 Results and Discussion

### 4.2.1 Conformal Growth

To demonstrate the conformal coating of individual fibers within a material, parallel plate electrospinning was used to create flexible nonwoven mats of microscale nylon 6,6 fibers ($D = 1.64 \pm 0.25$ μm), from hexafluoroisopropanol solutions (Figure 39a-b)[141]. Selecting poly(dimethyldiallylammonium chloride) (PDAC) as the cationic species and amphoteric titanium dioxide nanoparticles (which have been synthesized at a pH above the isoelectric point rendering them negatively charged) as the anionic species, a sprayed deposition can be performed. Chosen for its photocatalytic capabilities, this system presents an ideal candidate for catalysis applications by implementing a surface coating on a high surface area scaffold. Imposing a pressure gradient across the electrospun material during the deposition generates a controllable convective flow rate which was found to have a profound effect on the geometry of the developing film. Recalling $Re_d \approx 6$ as the critical diameter-based Reynolds number for flow separation from the downstream side of a cylinder[142], surprising agreement with the correlation is observed; At $Re_d = 6.5$ film growth is observed only near the stagnation point on the front of the cylindrical fibers (Figure 40a). It is possible that growth is occurring at the downstream stagnation point on the back side of the fibers as well. Unfortunately cross-sectioning, prior to SEM imaging, tends to remove the stagnation growth (on the front and possibly the back) before it can be observed. Prior to cross-sectioning we are unable to see the back side of the fibers to confirm the presence of a coating. However as $Re_d$ becomes sub-critical, uniform coatings develop conformally on individual fibers within the mat (Figure 40b). The coating does not exhibit preference toward the direction of flow (Figure 39c), but grows linearly (Figure 40c) at rates similar to those observed on planar substrates (9.6 nm/cycle)[31]. This indicates that viscous forces are responsible for species deposition, not line-of-sight impact as observed at higher $Re_d$ values. Furthermore, based on the Spray-LbL technique, conformal coatings can be created rapidly and uniformly even on large substrate areas using this technique. From electron microscopy, it is clear that the nanofibers are each individually coated with a concentric and uniform shell of polymer multilayer, and that the shell is of consistent thickness independent of fiber diameter or position within the electrospun cross-section ( $\approx$ 0.5 mm thick). Furthermore, Energy Dispersive X-ray (EDX) elemental analysis of the cross-section of the conformally treated electrospun mat indicates in Figure 41 that titanium dioxide (confirmed by tracing elemental titanium) is present across the entire cross-section, not simply near the upstream surface.

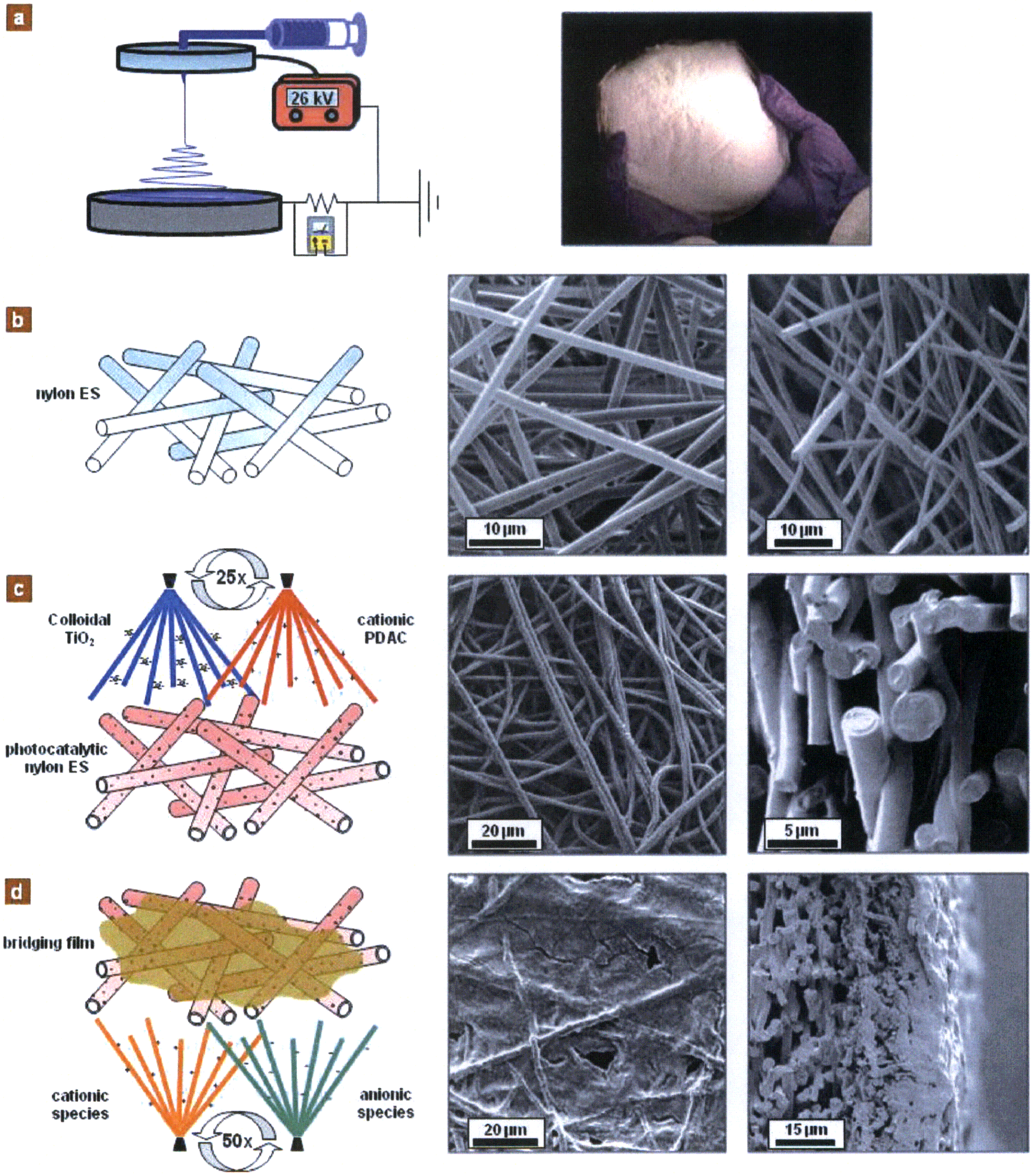

**Figure 39. Multi-functionalization process on electrospun mats**

**(a)** parallel plate electrospinning technique (diagram, left) is used to create nylon 6,6 electrospun mats of 8-10 inch diameter (right), represented schematically in **(b)**, and with top-down (center column) and cross-sectional (far right) SEM micrographs. **(c)** the technique of spraying in concert with a pressure gradient across the mat is demonstrated to create $(PDAC/TiO_2)_{25}$ conformal coatings on individual fibers. Conformal coatings are of uniform cross-section independent of spray direction, and smoothly coat the length of the fibers. **(d)** spraying in the absence of a pressure gradient to deposit $(PDAC/SPS)_{50}$ coating bridges pores on the mat surface. Heavy bridging occurs after relatively few deposition cycles, and can be performed using a variety of charged species to affect functionality of the final membrane.

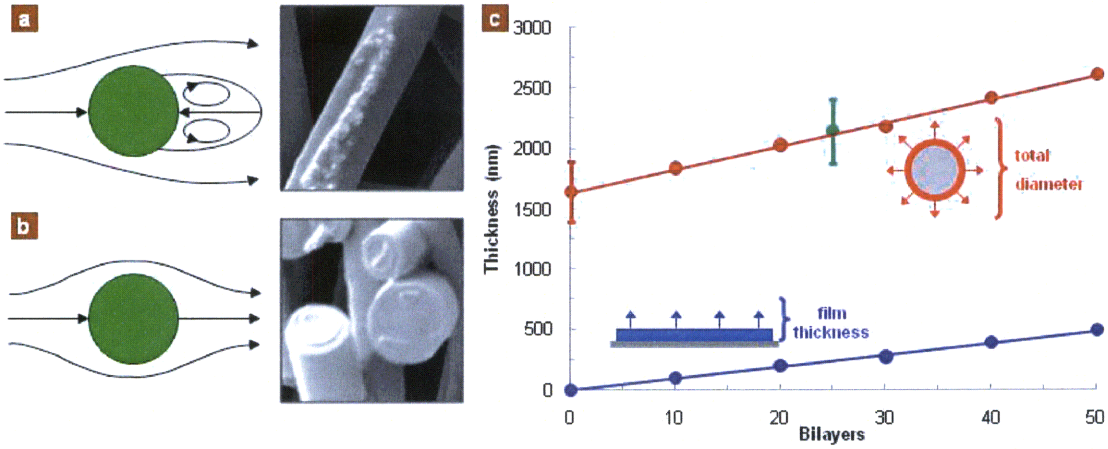

**Figure 40. Flow-rate dependant growth mechanism**

**(a)** For packed bed Reynolds numbers $Re_d = (D*V_s) / ((1-\varepsilon)*\nu) > 6$ (where D is the average fiber diameter, $V_s$ is the superficial fluid velocity, $\varepsilon = 0.85$ is the void fraction of the electrospun mat, and $\nu = 15.7 \times 10^{-6}\ m^2/s$ is the kinematic viscosity of air at 300K) flow separation of the streamlines from the back side of the fiber occurs. At these fluid velocities (SEM taken for $Re_d \approx 6.5$) LbL deposition is only observed to occur near the leading edge stagnation point on the fibers. **(b)** As the velocity is decreased and $Re_d$ becomes subcritical, the absence of flow separation allows viscous forces to uniformly deposit polyelectrolyte molecules evenly around the fiber circumference (cross-sectional

SEM taken at $Re_d \approx 1.7$). **(c)** The growth profile observed for $(PDAC/TiO_2)_n$ deposited on planar silicon is plotted in blue, and indicates a rate of 9.6 nm per cycle. Assuming conformal growth is due to a similar mechanism for $Re_d < 6$, the expected incremental increase in average fiber diameter is plotted in red starting from the observed initial fiber diameter. Average fiber diameter (red line) is expected to grow twice as rapidly as a planar film (blue line) since the deposited layer is counted twice, once from each side of the fiber, by this measurement. Remarkable agreement is observed for the empirical mean and standard deviation of electrospun fibers treated with $(PDAC/TiO_2)_{25}$, plotted in green. Error bars reflect +/- one standard deviation in values observed using SEM images.

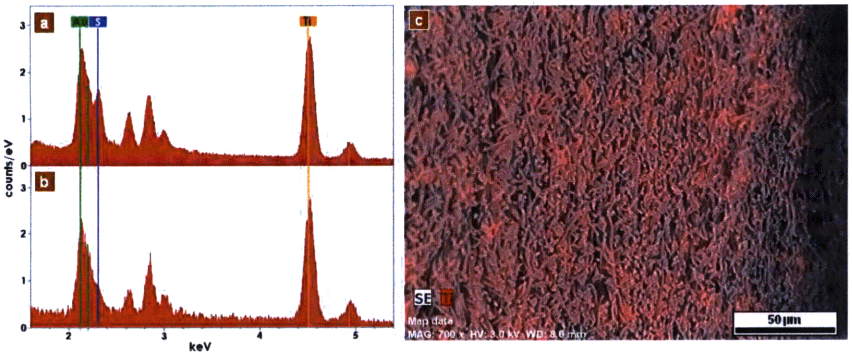

**Figure 41. Cross-sectional elemental analysis**

EDX data collected using a 10 keV beam potential from, a, the bridged surface of the mat, indicating the presence of titanium, from the $TiO_2$, and sulfur, from SPS in the bridged layer. b, Data collected from deeper within the treated electrospun mat indicates a similar level of titanium but very little sulfur, suggesting $TiO_2$ has been deposited throughout the mat while the $(PDAC/SPS)_n$ treatment has been restricted to the surface in the absence of a pressure gradient during deposition. Samples were first sputtered with an Au-Pd coating in preparation for microscopy, thus the gold peak's presence in both scans. c, Further EDX mapping (at reduced voltage to minimize sample deterioration during the prolonged time required for elemental mapping) again indicates the presence of titanium throughout the mat cross-section. Blotchy image is due to reduced map resolution chosen to minimize sampling time and reduce destructive charging.

### 4.2.2 Bridging Growth

In the absence of a pressure gradient (i.e. $Re_d = 0$) the conformally coated mats can be further processed using the same Spray-LbL technique. Instead of convectively penetrating into the electrospun matrix, polyelectrolyte chains arriving at the material's surface begin to fill the gaps between fibers. As serial deposition continues the coating grows laterally, filling interstitial voids. After only 50 sequential alternations between the cationic species PDAC and a suitably strong polyelectrolyte anionic species such as poly(sodium 4-styrenesulfonate) (SPS), the bridging of surface voids is nearly complete (Fig. 1d). It is perhaps surprising that polyelectrolytes with hydrodynamic sizes on the order of 50 nm are able to occlude 10-20 μm gaps between fiber supports; however, without a convective force driving polyelectrolyte transport throughout the porous network, surface fibers act as an electrostatic net catching the ≈ 5 μm droplets between nearby fibers via favorable interfacial interactions. Fiber spanning ensues, and bridges efficiently build across the larger pores as the LbL cycle is repeated. As a result penetration is restricted to 20-30 μm at the surface of the nylon matrix. It should be noted that we believe the geometry of the electrospun material plays a crucial role in the bridging process as well. In this demonstration impinging droplets of solution are of similar order of magnitude in size compared to the inter-fiber voids, and vary in charge density. At this scale fluidic properties such as solid-liquid contact may play an equally important role as electrostatics during the bridging process. The upper limitation on bridgeable pore size, if any, will yield further insight into the underlying mechanisms of this type of growth, and will be the subject of future investigation.

The flexibility of this technique is further demonstrated by extending the choice of bridging materials to include polyelectrolyte solutions at pH values drastically different than pH 10, at which $(PDAC/TiO_2)_n$ deposition was conducted. When (PDAC/SPS) in the previous example is replaced by the polyelectrolyte system poly(amidoamine) (PAMAM) and poly(acrylic acid) (PAA) titrated to pH 4, the conformal (PDAC/$TiO_2$) coating remains intact and unaffected. Prolonged exposure to pH 4 solutions in traditional LbL dipping baths would normally lead to loss of ionization of titania nanoparticles (pI = 6), exfoliation and eventual deconstruction and destabilization of (PDAC/$TiO_2$)$_n$ coatings, severely restricting the range of available pH conditions for processing. The Spray-LbL process is significantly more rapid, and the treated mat is never subjected to prolonged soak exposure times at potentially unfavorable pH, lending greater flexibility to the range of coatings which can be applied to the same substrate sample.

### 4.2.3 Application of Conformal Functionalization

To demonstrate the advantages to material design and engineering this technique presents, we have investigated the application of multi-functionalized electrospun mats as self-cleaning materials that can provide toxic chemical protection to the wearer while maintaining comfort and breathability in the form of water vapor permeability. The goal of this application is to engineer a selectively reactive membrane with tunable mass transfer properties. Deposited as described above, the conformal application of a photocatalytic film in the presence of a pressure gradient (hereon written vac(PDAC/$TiO_2$)$_{25}$) onto the fibers of an electrospun nylon mat increases the active surface area of smooth as-spun fibers from 2.02 to 48.75 $m^2/g$ as determined by BET surface area analysis. BET-determined values were consistently found to be within 10% of those calculated via SEM measurements and the geometric relationship for untreated as-spun samples of both nylon and poly(ε-caprolactone)

$$\frac{A_{surface}}{mass} = \frac{2}{R_{fiber}\rho_{material}} \qquad \textbf{Eqn. 15}$$

where $R_{fiber}$ refers to the average electrospun fiber radius and $\rho_{material}$ refers to the density of the bulk electrospun mat. The 25-fold increase in surface area is directly due to the conformal coating, the outermost surface layer of which is nanoparticles as the LbL spray sequence concludes with the anionic species (in this case colloidal $TiO_2$), now encasing the smooth fibers originally generated during the intense whipping of the electrospinning process. Treated samples were subjected to photocatalytic testing by mounting the mat in between a sealed vapor space containing a saturated vapor of chloroethyl ethyl sulfide (CEES), a simulant for the chemical warfare agent HD mustard gas, and a stream of clean air.[31] By comparing the flux of CEES in the air stream with and without UV irradiation on the sample, the photocatalytic capability of the treated material can be quantified as

$$photocatalytic\_capability = 1 - \frac{\int_{t_0}^{t_\infty} [permeant]_{UV} dt}{\int_{t_0}^{t_\infty} [permeant]_{dark} dt} \qquad \textbf{Eqn. 16}$$

where the permeant concentrations refer to the concentration of CEES in the air stream below the sample. An ideal sample will have a photocatalytic capability of 1.0, as the net flux of CEES during the UV illuminated test approaches zero, whereas a material with no photocatalytic capability will rate 0.0. Electrospun nylon treated with vac$(PDAC/TiO_2)_{25}$ exhibits high surface area for catalytic reaction, degrading 15% of the CEES dosage when exposed to UV light, but the reaction remains rate limited by the rate of adsorption of CEES onto the fiber surfaces, allowing significant amounts of CEES contaminant to move diffusively through the highly porous mat. (Note: To confirm that $TiO_2$ is necessary for CEES degradation a negative control test using untreated Nylon under UV light was conducted. This test also served as a leak control test of the permeation cell. The integrals in the numerator and denominator of the "photocatalytic capability" calculation were within 2% of each other, confirming the reproducibility of the test process as well as the necessity of $TiO_2$ in the degradation process.) Placing the functionalized electrospun material in series with a nonporous barrier material such as Saran® 8 (a biaxially oriented monolayer film of poly(vinylidene chloride)) eliminates rapid vapor diffusion through the matrix. Acting as diffusive resistance and restricting mass transfer, Saran increases the residence time of CEES molecules in the photocatalytic matrix. Consequently, the observed photocatalytic capability increases to 87%. This scenario illustrates the traditional trade-off of chem-protective materials: chemical barriers suppress toxic chemical penetration, but in the process suppress transport of other small molecules such as water vapor. Electrospun nylon + vac$(PDAC/TiO_2)_{25}$ is highly porous and allows water vapor flux at 14.3 $kg/m^2$-day, but is only able to degrade 15% of a saturated CEES dosage. Placing it in series with a Saran barrier significantly increases the catalytic residence time, but in order to achieve the resultant 87% CEES deactivation, we decrease the water vapor flux by 99%.

### 4.2.4 Application of Asymmetric Functionalization

The Spray-LbL platform presents an elegant solution by enabling the application of a mass transfer limiting "barrier" layer with controllable properties and thickness directly onto the functionalized membrane using electrostatic assembly of hydrophilic polyelectrolytes. To establish a basis by which polyelectrolyte multilayers form an effective barrier layer, the mass transfer properties of four weak polyelectrolyte systems were evaluated by spraying non-porous films on microporous polycarbonate substrates. Weak polyelectrolytes vary their degree of ionization as a function of solution pH, presenting a means to manipulate the effective ionic crosslinking of the film as well as the chemical composition independently to tune permeation of CEES molecules through the matrix. Using the time-lag method[143,144] to describe solution-diffusion mass transfer of solute molecules through a non-porous material[77], permeability values were collected for the four polyelectrolyte systems deposited over a range of pH values. This technique can be demonstrated using the inert barrier layer Saran 8, which was utilized in Chapter 2 for its CEES mass transfer regulating properties (Note: the time-lag method can also be applied to reactive barrier materials[145], however the math becomes significantly more complex). Figure 20 can easily be converted from ppm signal at the Total Hydrocarbon Analyzer to an instantaneous flux through the sample at time t, $J_t$, if the flow rate of carrier gas, F, and cross-sectional area of the membrane, A, are known using

$$J_t\left[\frac{mol}{cm^2 \cdot s}\right] = (ppm_t)(1x10^{-6})\rho_{carrier}\left[\frac{mol}{cm^3}\right]F\left[\frac{cm^3}{s}\right]\left(\frac{1}{A[cm^2]}\right)$$

**Eqn. 17**

where $\rho_{carrier}$ refers to the density of air (or nitrogen depending on the sweep gas) at STP. The net flux profile over time, Q(t), can be calculated by integrating the instantaneous flux values

$$Q(t) = \int_0^t J_t dt$$ **Eqn. 18**

to generate a plot similar to that shown in Figure 42. Four regions of this plot are worth noting: (1) an introductory region leading up to breakthrough, during which no CEES vapor is detected in the carrier stream, (2) increasing appearance of CEES in the carrier stream as the permeation profile approaches steady-state, (3) the steady-state plateau, visible in Figure 20 as a level plateau and in Figure 42 in pink, during which a constant rate of CEES permeates through the Saran film, and (4) a region after the steady-state portion of the test indicating the vapor space has been depleted of CEES liquid and the test is complete. While region 4 data is typically discarded, the linear portion of region 3 can be used to calculate the Diffusivity of CEES in Saran.

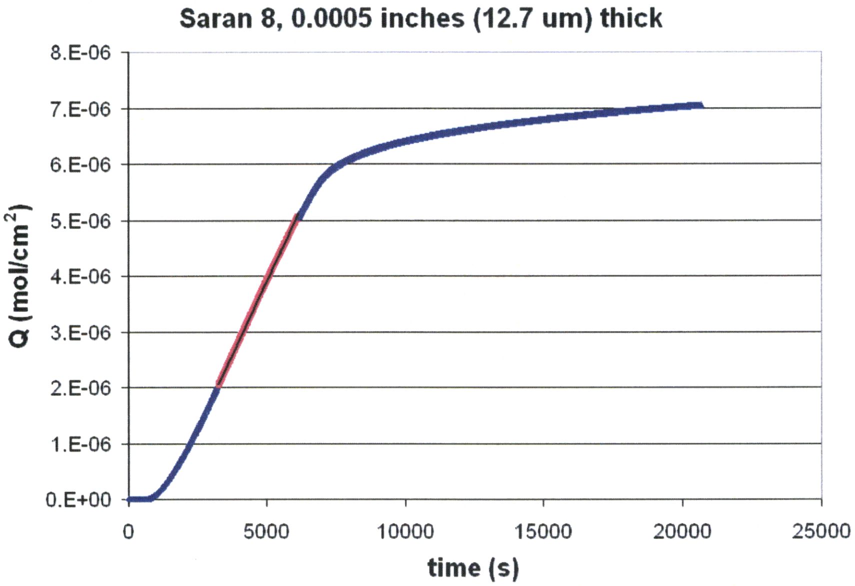

**Figure 42. Net flux of CEES through Saran 8**

Net flux data calculated by integrating the instantaneous flux data generated using Figure 20 which describes the rate at which CEES vapor passes through a nonporous 12.7 μm thick Saran 8 film.

According to the time-lag technique, after the decay of transience the net flux of permeant as a function of time can be modeled

$$Q = \frac{DC_0}{l}\left(t - \frac{l^2}{6D}\right)$$ **Eqn. 19**

where D refers to the vapor diffusivity in the solid, $C_0$ refers to the driving force for mass transfer and l to the thickness of the sample. Thus, referring only to the linear portion of the net flux plot, the line can be regressed to the x-axis where Q = 0 and

$$t = \frac{l^2}{6D}$$ **Eqn. 20**

This value is denoted the lag-time or L. In this way, curve fitting the linear portion of Figure 42 determines the lag-time which in turn can be used to find the Diffusivity. The linear portion of the instantaneous flux curve is determined by isolating the plateau data points which deviate from the final flux value by less than the magnitude of noise in the data. Data points which deviate systematically from the plateau are considered to be prior to steady-state and not included in this linear regression. For the case of Saran 8, the lag-time is found using linear regression to be 1293 seconds, yielding a Diffusivity of 2.08 x $10^{-8}$ $cm^2/s$. Returning to the instantaneous flux profile, the Permeability of CEES through Saran 8 can be calculated directly from the steady state plateau. Here, Fick's First Law of Diffusion applies and the Permeability, P, can be calculated using

$$P\left[\frac{g \cdot cm}{s \cdot cm^2 \cdot bar}\right] = P[barrers] = \frac{J_{SS} \cdot MW_{CEES} \cdot l}{\Delta p} = \frac{\left[\frac{mol}{cm^2 \cdot s}\right]\left[\frac{g}{mol}\right][cm]}{[bar]}$$

**Eqn. 21**

where $J_{SS}$ refers to the steady-state condition and $\Delta p$ refers to the partial pressure gradient driving mass transfer. Knowing the Permeability and the Diffusivity, the Solubility can be calculated according to the solution-diffusion model

$$S = \frac{P}{D} = \frac{\left[\dfrac{g \cdot cm}{s \cdot cm^2 \cdot bar}\right]}{\left[\dfrac{cm^2}{s}\right]} = \left[\frac{g}{cm^3 \cdot bar}\right] \qquad \textbf{Eqn. 22}$$

Using this technique, the permeability can be broken down into a solubility contribution and a diffusivity contribution. To assess the impact of amine content and pH at which deposition is conducted on the mass transfer properties of LbL films four polycations, including two linear chains poly(allylamine hydrochloride) (PAH), which contains only primary amines, and linear poly(ehtyleneimine) (LPEI), which contains only secondary amines, as well as a branched-polymer branched poly(ethyleneimine) (BPEI), which contains roughly 25% primary amine, 50% secondary amines and 25% tertiary amines, and a hyperbranched dendritic molecule poly(amidoamine) (PAMAM), which contains tertiary amines in its interior and primary groups on the surface were deposited versus a common polyanion, poly(acrylic acid) (PAA), at four different pH values. Noting the $pK_a$ values for primary amines ($pK_a \approx 8$-$9$), secondary amines ($pK_a \approx 5$-$6$), tertiary amines ($pK_a \approx 6$-$7$), and carboxylic acids ($pK_a \approx 6.5$), the pH range for testing was chosen to be 3-6. For example, $(PAMAM/PAA)_{100}$ films were deposited at pH 3, 4, 5, and 6, after which permeation testing was conducted versus CEES to generate the four net flux versus time profiles shown in Figure 43. Similar tests were conducted for the remaining three polyelectrolyte systems. The solubility contribution (average calculated values tabulated in Table 3) in LbL films can be interpreted as the relative ease with which solute molecules interact with chemical species present in the polymer film as they traverse the film. The diffusivity contribution (average observed values tabulated in Table 4) reflects the molecular scale mobility of CEES in the coating. Increased solubility occurs when the energy associated with introducing a solute molecule into the polymer matrix is low, and decreased diffusivity is observed as the charged nature of the polyelectrolyte constituents increases leading to a more densely crosslinked electrostatic thin film. For example, films deposited from the weak polycation poly(allylamine hydrochloride) (PAH) and the weak polyanion PAA over the pH range 3-6 exhibit very similar CEES permeability values, recorded in Table 5 in units of Barrers,[146] to those observed for films of poly(ethyleneimine) (LPEI) and PAA, but for very different reasons. PAH is highly charged below its $pK_a$ ($\approx 8.5$) generating more densely crosslinked films, and lower diffusivities, than those created from LPEI ($pK_a \approx 5.5$) for the pH range in question. Similarly, CEES molecules interact more favorably with primary amine groups present in $(PAH/PAA)_n$ films than secondary amines present in $(LPEI/PAA)_n$ films, leading to significantly higher solubility values. The net effect on permeability appears quantitatively similar in Figure 44, but the insight gained by separating the permeability into solubility and diffusivity contributions is invaluable. In an effort to facilitate water vapor transport while retarding CEES transport, it is necessary to form a mass transfer-limiting surface layer bridging the network of fibers using polyelectrolyte systems that specifically exhibit low CEES solubility values.

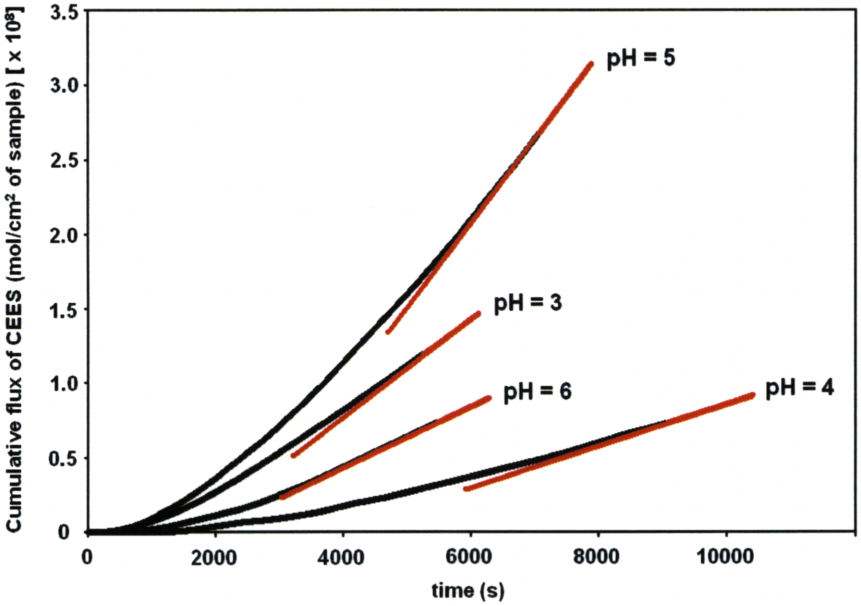

**Figure 43. Net flux data for (PAMAM/PAA)$_{100}$ pH series.**

Cumulative flux data has been tabulated by collecting instantaneous flux data and integrating over time. As the instantaneous flux profile approaches a steady state value the cumulative flux profile will become linear (highlighted in red). Regressing this line to the x-axis yields a time-lag value which is used to calculate the diffusivity of CEES through the (PAMAM/PAA)$_{100}$ films. Using this method, the longest lag time occurs for the film assembled at pH 4 ($\tau_{lag}$ = 3784 s), which can be attributed primarily to the thick film generated when PAA is only weakly charged, but PAMAM (both 1° and 3° amines) is highly charged. Being less densely ionically cross-linked this film also corresponds to a comparatively large diffusivity value.

| pH | 3 | 4 | 5 | 6 |
|---|---|---|---|---|
| LPEI/PAA | 30 | 4 | 1 | 13 |
| BPEI/PAA | 701 | 684 | 591 | 100 |
| PAMAM/PAA | 56 | 18 | 186 | 92 |
| PAH/PAA | 681 | 763 | 819 | 939 |

**Table 3. Average calculated Solubility in (g/cm$^3$·bar) of CEES in LbL films**

| pH | 3 | 4 | 5 | 6 |
|---|---|---|---|---|
| LPEI/PAA | 6.8E-11 | 7.2E-09 | 1.2E-08 | 1.9E-10 |
| BPEI/PAA | 9.2E-11 | 2.6E-10 | 2.8E-10 | 1.0E-10 |
| PAMAM/PAA | 2.7E-09 | 1.3E-08 | 1.1E-09 | 5.6E-10 |
| PAH/PAA | 2.6E-11 | 5.4E-11 | 1.2E-11 | 7.5E-12 |

**Table 4. Average observed Diffusivity in (cm$^2$/s) of CEES in LbL films**

| pH | 3 | 4 | 5 | 6 |
|---|---|---|---|---|
| LPEI/PAA | 2.0E-09 | 2.6E-08 | 2.6E-08 | 2.6E-09 |
| BPEI/PAA | 6.4E-08 | 1.7E-07 | 1.6E-07 | 1.0E-08 |
| PAMAM/PAA | 1.5E-07 | 2.3E-07 | 2.1E-07 | 5.1E-08 |
| PAH/PAA | 1.8E-08 | 4.1E-08 | 2.9E-08 | 7.0E-09 |

**Table 5. Average observed Permeability in (Barrers) of CEES in LbL films**

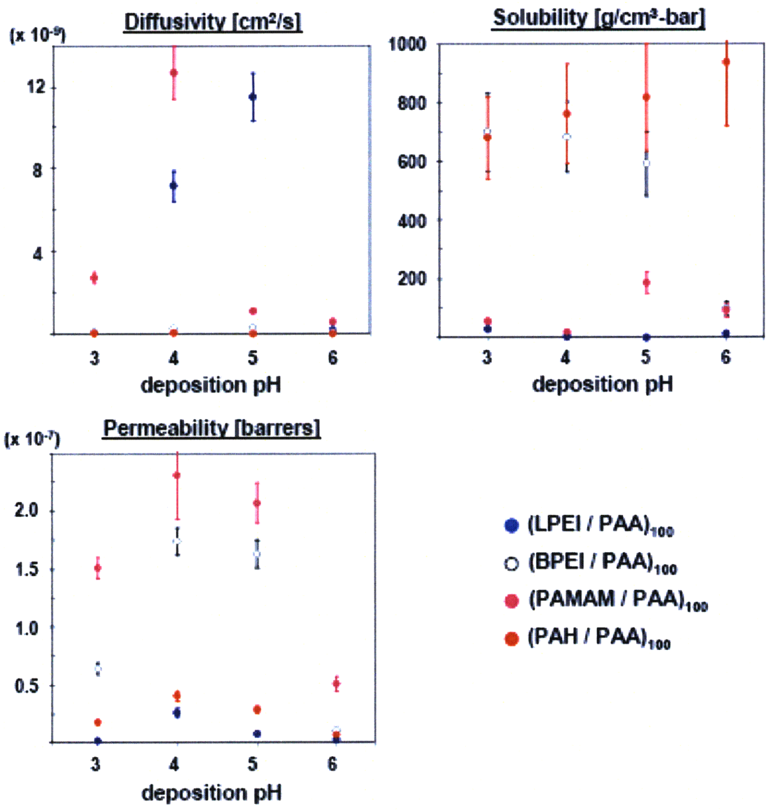

**Figure 44. Diffusivity, Solubility and Permeability data**

Permeability, diffusivity and solubility of CEES measured for four LbL films deposited over a range of pH values. Permeability data has been collected using a specially designed cell[31] for four LbL systems deposited at pH = 3, 4, 5, and 6 on microporous polycarbonate track etched membranes, and plotted as instantaneous flux as well as cumulative flux over time. The steady state plateau obtained from the plot of instantaneous flux versus time is used to calculate the permeability through the film, while the diffusivity is calculated using the time-lag method[143,144]. By extrapolating the linear portion of the cumulative flux versus time plot back to the x-axis intercept a time-lag equal to the film thickness squared over six times the diffusivity can be found. The solubility is then readily calculated as the ratio of the permeability and the diffusivity. This type of analysis presents vital engineering properties of the materials that give insight into why a material is an effective barrier. Solubility values reflect the energetic favorability of allowing a solute molecule into the polymer matrix, while diffusivity values quantify the architectural barriers to mass transfer. As a result, two materials can demonstrate very similar permeability values, such as $(LPEI/PAA)_n$ and $(PAH/PAA)_n$, but for very different reasons. Error bars on permeability values were determined by compounding maximum possible experimental error due to FID detector resolution, flow meter resolution, and typical variation in film growth rates. Similarly, error bars on diffusivity values were based on typical variation in film growth rates. Since solubility values were calculated using permeability and diffusivity data, the reported error bars on solubility data reflect possible errors in either of these values.

Selecting materials which fit this criterion, we demonstrate the creation of asymmetrically functionalized electrospun (ES) membranes using the weak polyelectrolyte systems $(LPEI/PAA)_n$ at pH 5 and $(PAMAM/PAA)_n$ at pH 4, as well as the strong polyelectrolyte system $(PDAC/PAA)_n$, as bridging agents. In the absence of convective driving force ($Re_d = 0$), 50 bilayers of the dendritic PAMAM deposition efficiently bridges the surface pores while penetrating less than 30 μm into the 300 μm thick electrospun membrane. A barrier layer is created near the mat's surface (Figure 45) reminiscent of asymmetric polymer membranes created by phase inversion[147,148]. In this case, however, the remaining 90% of the mat contains conformal vac($PDAC/TiO_2$) functionality, and is capable of degrading contaminant molecules, with the aid of UV light, during their prolonged residence time in this portion of the membrane. While it appears quite porous, the barrier layer visible in the cross-sectional image is capped with a thin, relatively continuous polymer film (Figure 39d) covering more than 95% of the surface. Furthermore, since the CEES-barrier properties of the $(PAMAM/PAA)_{50}$ region are due primarily to solubility effects, the hydrophilic nature of the sublayer and thin-film skin continues to permit water vapor permeation. When compared to ES vac($PDAC/TiO_2$) material with no bridged layer, ES vac($PDAC/TiO_2$) + $(PAMAM/PAA)_{50}$ samples demonstrate an increase in photocatalytic capability as defined by Eq. 16 from 15% to 74%, while maintaining a water vapor flux of 14.3 $kg/m^2$-day (for comparison cotton materials typically allow 12 - 14 $kg/m^2$-day, while any material demonstrating flux greater than 1 $kg/m^2$-day is categorized as water permeable). This reflects a roughly 0.5% reduction in flux compared to non-bridged ES vac($PDAC/TiO_2$). Peak flux of CEES under UV light briefly climbs to similar levels observed in dark tests (Figure 46) due to some vapor diffusion that occurs rapidly through the remaining pores, but sharply recedes as the detoxifying features of the film activate.

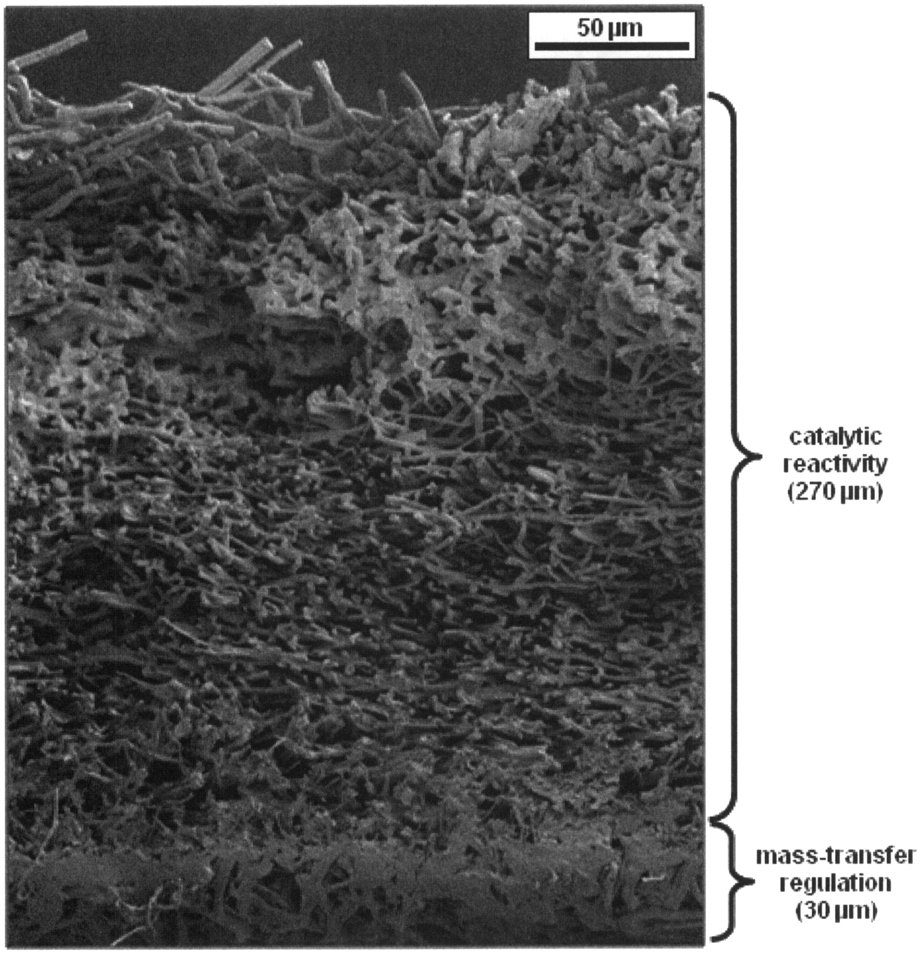

**Figure 45. Cross-section of a multi-functionalized membrane**

An electrospun nylon sample which has been treated with $(PDAC/TiO_2)_{25}$ in the presence of a pressure gradient to create a high surface area photocatalytic region, followed by $(PAMAM/PAA)_{50}$ treatment in the absence of a gradient to create a CEES transport barrier can be seen in its entirety. Closely resembling an asymmetric polymer membrane for high efficiency gas separation, only 30µm, or roughly 10% of the membrane, near the surface is responsible for regulating mass transport, while the remainder of the membrane is free to act as a high surface area scaffold for photocatalysis as well as mechanical support for the relatively thin barrier region. Flux can be closely controlled by tuning the content and thickness of the barrier region, producing an optimal residence time for catalytic degradation to occur.

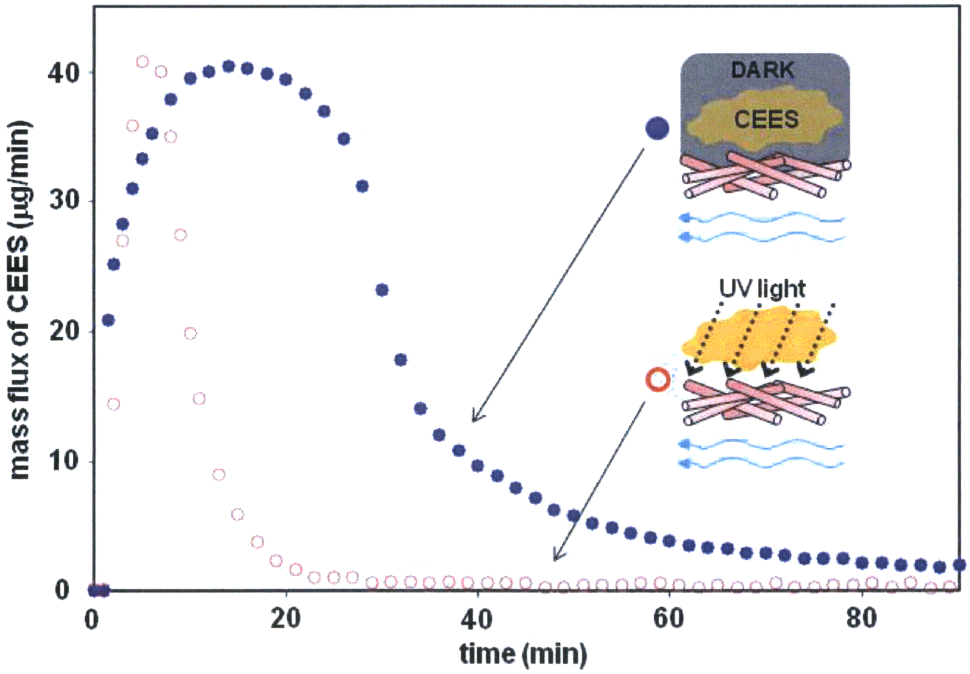

**Figure 46. CEES permeation test results**

An electrospun nylon sample is treated with $(PDAC/TiO_2)_{25}$ along with a pressure gradient to create a high surface area photocatalytic region, followed by $(PAMAM/PAA)_{50}$ in the absence of a gradient to create a barrier to CEES transport. Upon exposure to 3 μL of CEES the mass flux of CEES across the membrane and into the sweep gas is observed in the presence of UV light as well as in the dark. In both cases a time-lag of 60-90 seconds is observed during which the vapor sample is in the capillary of the test system but has not yet reached the detector. Net permeation over the duration of the test is reduced by more than 74% in the presence of UV light while peak flux occurs earlier in the test when compared to the dark scenario. This is attributed to UV absorption, localized heating and material expansion of the thin barrier film restricting CEES permeation.

For comparison, measured photocatalytic capabilities as well as water vapor flux rates for ES vac(PDAC/$TiO_2$) + $(PDAC/SPS)_{50}$ and ES vac(PDAC/$TiO_2$) + $(LPEI/PAA)_{100}$ are tabulated in Table 6 along with BET surface areas for the two best performing films. ES vac(PDAC/$TiO_2$) + $(LPEI/PAA)_{100}$ demonstrated high water vapor permeability as expected from its low CEES solubility during $(LPEI/PAA)_n$ permeability tests (Note: CEES permeation tests are conducted at ambient humidity, thus solid films that exhibit high water permeability naturally tend to have more moisture present in their matrix. CEES and water mixtures are highly energetically unfavorable, which explains the tendency for high water vapor solubility, thus permeability, and low CEES solubility to go hand in hand); however, the low molecular weight LPEI (25k) resulted in a barrier layer with less tendency to bridge the large electrospun pores. Significant amounts of CEES were therefore able to pass via vapor diffusion, avoiding degradation. Higher molecular weight SPS (1M), in combination with PDAC (150,000), led to a greater degree of pore bridging, as indicated by the membranes' measured surface area decrease from 48.75 to 36.59 $m^2/g$, thus increasing residence time for photocatalytic activity. Similarly, the effects of less hydrophilic SPS in the barrier region and thin-film skin manifest themselves in reduced water vapor flux as compared to samples bridged using the high amine content PAMAM system. As discussed previously the traditional trade-off between barrier properties and water vapor transport is described graphically in Figure 47. Materials along the axes exhibit either good reactive barrier properties or high water vapor flux, but not both. *The ability to control chemical identity, thickness and degree of bridging in the flux-limiting portion of the membrane enables enhancement of the reactive properties while maintaining membrane breathability*, producing an engineered textile that exhibits the reactive capability of non-porous barrier materials and water vapor flux similar to highly porous untreated electrospun mats. ES vac(PDAC/$TiO_2$) + $(PAMAM/PAA)_{50}$ shows a significant decrease in membrane surface area due to the pore bridging ability of the dendritic PAMAM molecules, as well as high water vapor flux due to their hydrophilic nature.

| # | | Water Vapor Flux (kg/m$^2$-day) | Photocatalytic Capability | Surface Area (m$^2$/g) |
|---|---|---|---|---|
| 1 | **Saran® plastic film + (PDAC/TiO$_2$)$_{25}$** | **0.2** | **0.48** | **-** |
| 2 | **Electrospun (ES) Nylon** | **14.3** | **0** | **2.02 ± 0.08** |
| 3 | **ES + vac(PDAC/TiO$_2$)$_{25}$** | **14.3** | **0.15** | **48.75 ± 1.02** |
| 4 | **ES + vac(PDAC/TiO$_2$)$_{25}$ over Saran film** | **0.2** | **0.87** | **-** |
| 5 | **ES + vac(PDAC/TiO$_2$)$_{25}$ + (PDAC/SPS)$_{50}$** | **12.8** | **0.58** | **36.59 ± 0.01** |
| 6 | **ES + vac(PDAC/TiO$_2$)$_{25}$ + (PAMAM/PAA)$_{50}$** | **14.2** | **0.74** | **19.15 ± 0.30** |
| 7 | **ES + vac(PDAC/TiO2)$_{25}$ + (LPEI/PAA)$_{100}$** | **14.2** | **0.27** | **-** |
| 8 | **US Army Cotton Battle Dress Uniform** | **12.1** | **0** | **-** |

**Table 6. Permeability to CEES and water vapors exhibited by several asymmetrically-functionalized samples.**

Measured water vapor flux and photocatalytic capability of several untreated (#2 and 8), photocatalytically functionalized (#1, #3 and #4), and multiply functionalized (#5-7) samples. Each surface area range represents values collected from three separate samples deposited from independent solutions. Samples #5 and 6 demonstrate the advantages of conformal TiO$_2$ treatment as well as pore bridging on available surface area and permeation characteristics. The dramatic increase in surface area observed when as-spun nylon fibers are conformally treated with (PDAC/TiO$_2$)$_{25}$ coatings does not translate to increased photocatalytic ability until a barrier layer is added to mitigate vapor phase diffusion through the membrane and increase the residence time for reaction to occur.

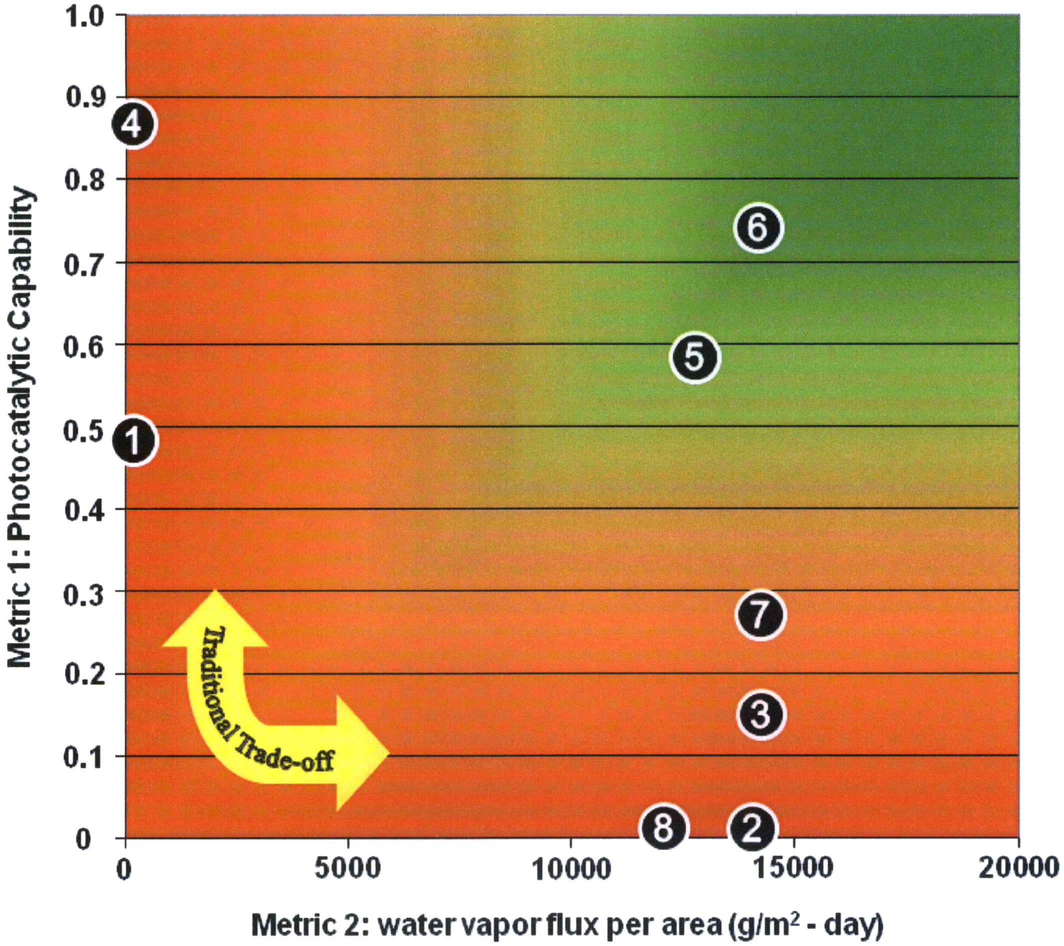

**Figure 47. Trade-off between degradative and water vapor transport rates.**

Graphical representation of data tabulated in Table 6. Traditionally, effective barrier materials (#1 and 4) do not possess the high selectivity necessary to discern between water molecules and contaminant molecules, thus sacrificing water vapor permeability in an effort to limit toxic molecule permeation. Alternatively, highly porous materials (#2 and 8) readily permit water vapor transport, but provide little resistance to hazardous vapors. Multiply functionalized electrospun materials (#5-7) are able to act as tunable asymmetric membranes to optimize the residence time of toxic vapors in the reactive portion of the membrane, improving photocatalytic activity without sacrificing water vapor permeability.

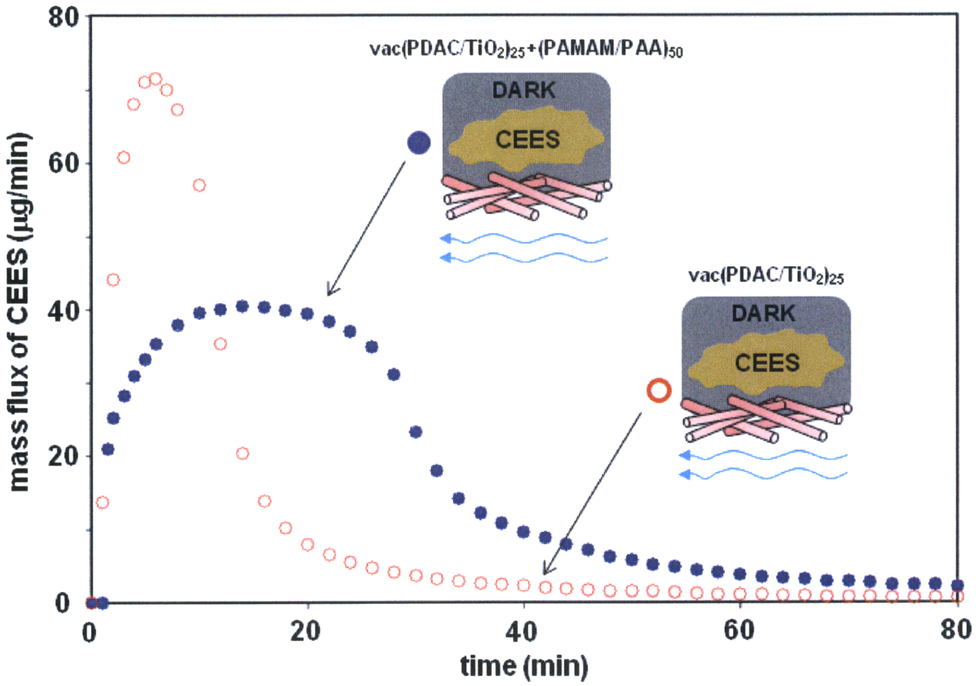

**Figure 48. Effect of bridged layer on non-reactive mass transfer**

Two electrospun nylon samples are treated with (PDAC/$TiO_2$)$_{25}$ along with a pressure gradient to create a high surface area photocatalytic region. One sample is subsequently treated with (PAMAM/PAA)$_{50}$ in the absence of a gradient to create a barrier to CEES transport. Upon exposure to 3 µL of CEES the mass flux of CEES across each membrane and into the sweep gas is recorded for both samples in the dark. In the absence of UV degradation the net flux remains the same over the duration of either test, but a reduction in peak flux, by roughly 56%, is observed when the bridged layer is in place. This reduction in peak flow rate increases the residence time of CEES in the photocatalytic region of the mat and thus increases photocatalytic degradation.

### 4.2.5 Reactive Membrane Model

To validate the decision to use Layer-by-Layer bridging films as the perm-selective barrier in the system tested here, we have modeled the asymmetrically functionalized electrospun membrane as a Packed Bed Reactor (PBR). Packed Bed Reactors are typically tubular and filled with solid catalyst particles to provide large amounts of surface area for heterogeneous fluid-solid reactions to occur. In this instance the packed bed is made of surface-functionalized fibers as opposed to solid particles. As noted previously for asymmetric gas separation membranes, once treated there are two subregions within the composite mat. The first region encountered is responsible for catalytic reactivity, but provides relatively little resistance to mass transport. The second region, made up of a bridged network of electrospun fibers, is specifically designed not only to restrict mass transfer in general, but to selectively restrict mass transfer of CEES and water vapor to different extents. For simplicity we begin by neglecting any byproducts generated by the photocatalytic degradation of CEES, and model flow in the two region PBR as two-component; CEES and water. As described in Figure 49, catalytic degradation within the mat implies the volumetric flow rate, $\nu_{CEES}$, and concentration, $C_{CEES}$, of CEES vapor at the outlet of the mat will be less than that at the inlet, however water vapor will not be affected by the catalytic process, thus $\nu_{water}$ will remain constant in the absence of a pressure gradient (i.e. $\Delta P = 0$).

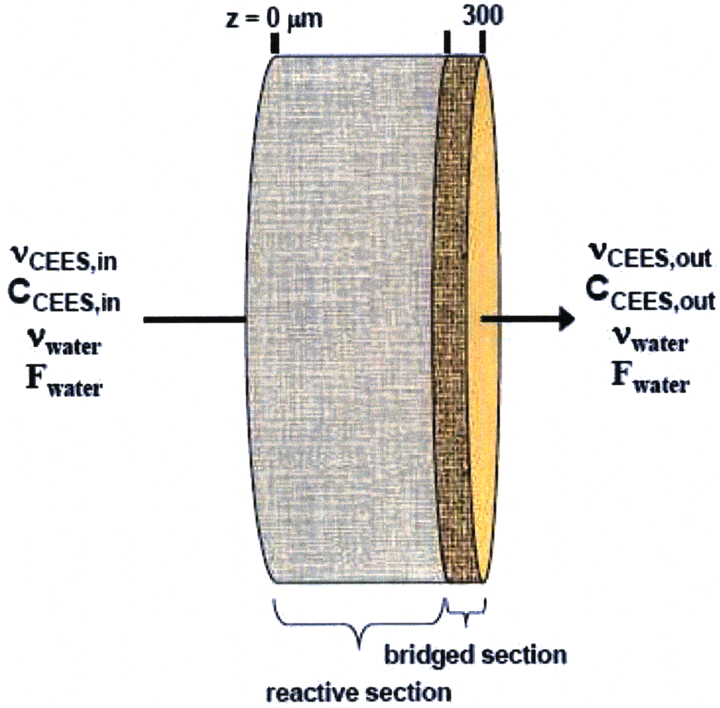

**Figure 49. Packed Bed Reactor Schematic**

The multi-functionalized mat can be modeled as a packed bed containing two sections. One section contains conformally coated electrospun fibers and is responsible for catalytic decomposition of CEES. The second section contains a bridged network of fibers and is responsible for selectively restricting mass transfer of CEES and water through the composite mat.

With no pressure gradient across the sample, thus no convection to measure, the unreacted flow of water vapor provides a way to quantify the mass transfer process due to diffusion. It is unclear from Figure 39d or Figure 45 precisely how thick the bridged layer within the network of fibers is, nor is it clear precisely what fraction of the mat surface is occluded by this network. An effective thickness of the bridged layer can be deduced, however, by applying previous data obtained from water permeation and CEES permeation tests performed on planar $(PAMAM/PAA)_n$, $(LPEI/PAA)_n$ and $(PDAC/SPS)_n$ films to the data observed here. $(PAMAM/PAA)_{25}$ exhibits a mass transfer resistance to water vapor of 950 s/m via DMPC test (Figure 51). Tested at 20°C by passing a 95% relative humidity stream ($p_{water}$ = 22.203 hPa) and a 5% R.H. stream ($p_{water}$ = 1.169 hPa) across opposite sides of the $(PAMAM/PAA)_{25}$ film, supported again by a track-etched polycarbonate support membrane, the water vapor flux rate can be calculated using

$$\frac{Flux}{area}\left[\frac{mol}{cm^2 \cdot s}\right] = \frac{1}{R[s/m]}(C_1 - C_2)\left[\frac{mol}{cm^3}\right] \qquad \textbf{Eqn. 23}$$

which can be obtained by solving the steady-state (no t-dependence), inert (no reaction term) form of Eq. 6, where R refers to the water vapor mass transfer resistance and $C_1$ and $C_2$ refer to the concentration of water vapor in the two streams as defined by the relative humidity and temperature. A water vapor flux of 9.13 x $10^{-8}$ mol/cm$^2$-s can then be converted to a water vapor permeance of 6.7 g/day-cm$^2$-bar by first calculating the partial pressure driving force for mass transfer to be 0.021 bar from the relative humidities. Permeance is similar to permeability in the way that resistance is similar to resistivity. Resistivity, like permeability, is a material property independent of geometry, but resistance is not. For example, a 3 foot long metal rod will exhibit the same resistivity as a 6 foot long rod of the same metal and cross-section, but half the resistance. Likewise, to convert the permeance value to a permeability which can be applied to $(PAMAM/PAA)_n$ films of varying thickness the permeance must be multiplied by the thickness of the film to get a water vapor permeability, through any $(PAMAM/PAA)_n$ deposited at pH 4, of 4.25 x $10^{-3}$ g/day-cm-bar. Tabulated in Table 7, this process can be repeated to calculate the water vapor permeability through $(LPEI/PAA)_n$ films deposited at pH 5 and $(PDAC/SPS)_n$ films created at 0.1 M NaCl.

| sample | mass transfer resistance (s/m) | water flux (mol/cm$^2$-s) | thickness ($\mu$m) |
|---|---|---|---|
| (PAMAM/PAA)$_{25}$ at pH 4 | 950 | 9.13E-08 | 6.300 |
| (LPEI/PAA)$_{25}$ at pH 5 | 1050 | 8.26E-08 | 0.163 |
| (PDAC/SPS)$_{25}$ at [NaCl] = 0.1 M | 156 | 5.56E-07 | 0.066 |

| sample | water permeance (g/day-cm$^2$-bar) | permeability (g/day-cm-bar) |
|---|---|---|
| (PAMAM/PAA)$_{25}$ at pH 4 | 6.75 | 4.25E-03 |
| (LPEI/PAA)$_{25}$ at pH 5 | 6.11 | 9.95E-05 |
| (PDAC/SPS)$_{25}$ at [NaCl] = 0.1 M | 41.09 | 2.73E-04 |

**Table 7. Water permeation data of planar LbL bridging films**

Understanding these material properties, independent of film thickness, allows us to calculate an implied 'effective thickness' of the (PAMAM/PAA) bridged network. This effective thickness will take into account any non-uniformity in the bridged layer such as pin holes or variation in thickness, resulting in a value which can be used to model the time spent by CEES vapor in the reactive portion of the mat as a result of the non-uniform bridged network of (PAMAM/PAA). Assuming negligible resistance to water vapor transport due to the reactive portion of the treated mat, all resistance can be attributed to the barrier layer. Water vapor permeation rates have been tabulated in Table 6 for the multi-functionalized electrospun mats, and can be converted to permeance values as described above. Using the equation

$$P^{water}_{(PAMAM\,/\,PAA)} = Permeance^{water}_{bridged} * thickness_{bridged} \qquad \textbf{Eqn. 24}$$

the 'effective thickness' of the (PAMAM/PAA) bridged network in the treated film is 0.629 μm, significantly less than the 10 μm value assumed prior to this analysis. This suggests that the pinholes observed in Figure 39d have a profound effect on the effective thickness of the bridged network, and also that the limitation to mass transfer is created by thin inter-fiber webs of material, not a 30 μm thick region as suggested by Figure 45. Further calculation indicates the effective thickness of the (PDAC/SPS) bridged layer in Sample #5 is significantly thinner at only 0.045 μm, while the (LPEI/PAA) bridged layer in Sample #7 is even thinner at 0.015 μm.

Knowing the effective thickness of the barrier layer restricting mass transport, we now turn to mass transfer of the second component, CEES. A rigorous analysis of CEES in the treated mat can be performed by constructing two species conservation equations similar to Eq. 6, one for each portion of the mat:

$$\frac{\partial C_{CEES}}{\partial t} = D_{CEES,1}\frac{\partial^2 C_{CEES}}{\partial z^2} + R_{v,CEES} \text{ (conformal/reactive region)} \qquad \textbf{Eqn. 25}$$

$$\frac{\partial C_{CEES}}{\partial t} = D_{CEES,2}\frac{\partial^2 C_{CEES}}{\partial z^2} \text{ (bridged/barrier region)} \qquad \textbf{Eqn. 26}$$

where $C_{CEES}(z, t)$ is a function of depth in the mat, z, and time, t. These equations are coupled by the symmetric boundary conditions at their shared interface, and subject to initial conditions. Ideally, selection of two diffusivity values (one for each portion of the mat), a reaction rate constant, and the thickness of each region would allow us to model the CEES flux profiles over time observed for each of the three asymmetrically functionalized systems in Table 6. Unfortunately, the inlet CEES concentration profile, $C_{CEES}(z = 0, t)$, is not known using our permeation system. In order to fit parameters to the model described above it would be necessary to deconvolute the CEES vs. time data obtained for the three dark (i.e. unreactive) scenarios to establish an inlet profile which could then be used as a boundary condition in solving the above pair of equations. This process could then be iterated to find the appropriate reaction rate constant and thicknesses of the two regions within the mat. To avoid uncertainty in the inlet stream, however, the remainder of this discussion will focus on integrated net-flux data, without time-dependence, to determine the effects of barrier material on the net photocatalytic capability of the multi-functionalized mats.

The permeability of CEES through $(PAMAM/PAA)_n$ at pH 4 and $(LPEI/PAA)_n$ at pH 5 films, independent of film thickness, are tabulated in Table 5 to be $2.31 \times 10^{-7}$ and $2.63 \times 10^{-8}$ Barrers respectively. The permeance of CEES through the mat is rate limited by the barrier layer, and can be calculated using the effective thickness determined from water vapor transport rates.

$$\frac{P^{CEES}_{(PAMAM\,/\,PAA)}}{thickness_{bridged}} = Permeance^{CEES}_{bridged} \qquad \textbf{Eqn. 27}$$

For the (PAMAM/PAA) and (LPEI/PAA) bridged samples the permeance is found to be 0.00367 and 0.0175 g/s-cm$^2$-bar respectively. Multiplying by the sample cross-sectional area and CEES partial pressure driving force, the permeance can be converted to volumetric flow rates of 0.0127 and 0.0606 cm$^3$/s of CEES through the barrier layer, indicating CEES travels through the (LPEI/PAA) bridged sample almost 5 times as rapidly as it does through the (PAMAM/PAA) bridged sample. Furthermore, these numbers can be converted to residence times spent by CEES in the reactive portion of the mat using

$$\tau_{CEES}[s] = \frac{V_{mat}\left[cm^3\right]}{v_{CEES}\left[\frac{cm^3}{s}\right]}$$ **Eqn. 28**

Thus $\tau_{CEES}$ equals 7.9 s for the (PAMAM/PAA) bridged sample and only 1.7 s for the (LPEI/PAA) bridged sample.

Typically, heterogeneous fluid-solid reactions such as this are modeled as packed bed reactors to calculate the weight of catalyst necessary to achieve a specific conversion of reactant in the bed. In our case, however, the precise weight of $TiO_2$ catalyst available for reaction (i.e. on the outermost surface of the fibers and untarnished by the bridging polymer during the deposition process) is neither precisely known nor easily controlled in the scope of this work. According to Fogler[149], there are seven steps in a catalytic reaction:

1. Diffusion of reactants from bulk fluid to external surface of the catalyst particle
2. Diffusion of the reactants from the pore mouth through the catalyst pores to the immediate vicinity of the catalytic sites
3. Adsorption of reactants onto the catalytic sites
4. Reaction on the surface of the catalyst
5. Desorption of the products from the surface
6. Diffusion of the products from the interior sites to the pore mouth at the external surface
7. Mass transfer of the products from the external pellet surface to the bulk fluid

one of which limits the process and dictates the rate for the entire reaction. I hypothesize that what is limiting the conversion of CEES is not quantity of $TiO_2$ catalyst, which would suggest that reaction on the surface (Step 4) is the rate-limiting step, but residence time spent in the proximity of the catalytic surfaces, thus either mass transfer from the bulk fluid to the catalytic sites (Steps 1 and 2) or binding of CEES onto the surface (Step 3) is rate-limiting. The available data are inconclusive as to which of these three phenomena, or possibly a combination, is limiting, so for the purposes of this discussion they will be grouped as the mass transfer process of CEES from the bulk stream to the bound state on the fiber surface, prior to reaction. If the hypothesis that this process is limiting the catalytic degradation holds, it is possible to model the reaction in terms of residence time CEES molecules spend traveling through the 'reactor', $\tau$, which is typically the case for a plug flow reactor (PFR). The outlet concentration of CEES, as measured by Total Hydrocarbon Analyzer during these tests, is a function of the inlet concentration, the residence time, $\tau$, and the reaction rate constant, k. Assuming for simplicity that the reaction is first order ($r = k^*C_{CEES}$) and isothermal (k = constant), the design equation for a PFR becomes

$$C_{CEES,out} = C_{CEES,in}e^{-k\tau} \qquad \textbf{Eqn. 29}$$

or

$$\frac{C_{CEES,out}}{C_{CEES,in}} = 1 - X = e^{-k\tau} \qquad \textbf{Eqn. 30}$$

where X is defined as the conversion of CEES within the mat. Substituting for conversion from Table 6 and $\tau$, the reaction rate constant, k, can be solved for each of the two systems in question

(PAMAM/PAA) bridged $\qquad 1 - 0.74 = e^{-k*(7.9s)}$

$$k = 0.171\ s^{-1}$$

(LPEI/PAA) bridged $1-0.27=e^{-k*(1.7s)}$

$k = 0.185\ s^{-1}$

The similarity of reaction rate constants calculated from two different systems suggests several conclusions; (1) the increased residence time caused by the (PAMAM/PAA) bridged layer is the primary reason for the increase in photocatalytic degradation observed in Figure 47, which implies (2) the proposed residence time dependent model suggested above adequately fits the two data points developed here, realizing fully that this is a very small sample size from which to draw these conclusions. These results do however present an interesting model by which to gauge future materials for testing. If the permeability of CEES through a sample material is known (or tested using the permeation cell described here), and the water vapor flux through the same material is independently known (or tested using the DMPC test described here), the degradative capabilities and water vapor flux rate of a conformally functionalized electrospun mat in series with a layer of the material of specified thickness can be calculated prior to creating and testing the composite system. The water vapor and CEES transport rates can then be compared to LbL materials tested here, allowing the proposed materials to be rapidly screened for applicability. If a successful material is identified, the challenge becomes to generate a mechanically stable film of the material that is sufficiently thin to meet the calculated requirement.

## 4.3 Conclusion

While these results present an attractive improvement on the current chemical protective measures practiced by the US Army, the applications are significantly broader in scope. Demonstrated here for high-efficiency reactive gas purification, the self-cleaning functionalities of these membranes can be extended to water purification, by creating and functionalizing filters with reactive capabilities[150,151], and fabric treatment[135,136,152]. As a readily scalable platform application, this technology also has potential in the large scale manufacture and treatment of carbon nanotube sheets[153,154], as well as the rapidly developing field of biological and tissue engineering by functionalizing high surface area scaffolds with proteins[155-159]. As the challenges of generating more complex polymer-based membrane systems require engineers to impart new functionalities to materials without sacrificing mechanical robustness[160] or ease of manufacturing, LbL spray-coating of porous nonwovens provides the versatility to control nanoscale features and functionality on the macroscopic level. Specialized technologies can now be developed in industrially-significant quantities using a rapid, yet inexpensive, scalable approach.

## 4.4 Experimental

Electrospun Materials Synthesis: In preparation for this work several electrospun materials were tested for applicability. Poly(ε-caprolactone) and poly(styrene) were found to be susceptible to attack by CEES acting as a chlorinated solvent. Poly(ethylene oxide) as well as PEO/poly(methyl methacrylate) copolymer blends were found to withstand chlorinated solvents, but were too water-soluble to be treated using an aqueous deposition technique like LbL. Electrospun nylon was mechanically stable in both chlorinated solvents as well as water, so nonwoven meshes of nylon fibers were made by electrospinning a solution of 10% nylon 6,6 (45,000 $M_w$) (Scientific Polymer Products) in hexafluoroisopropanol (Aldrich) at 0.1 mL/min with a needle-to-collector distance of 31 cm and a source voltage of 26.8 kV for 40 minutes using a parallel plate electrospinning apparatus[131]. Mats were soaked in 0.02 M aqueous solution of PAH (56,000 $M_w$) (Aldrich) for 30 minutes prior to LbL treatment.

LbL Film Assembly: LPEI (25,000 $M_w$) (Polysciences), PAA (15,000 $M_w$, 35% aqueous solution) (Aldrich), PAMAM (G4, 22% solution in methanol) (Dendritech), SPS (1,000,000 $M_w$) (Aldrich) and PDAC (150,000 $M_w$, 20% aqueous solution) (Aldrich) were used as received and prepared as 0.02 M solutions, based on the repeat unit molecular weight, in Milli-Q water (see Figure 50 for structures). A colloidal solution of $TiO_2$ nanoparticles was synthesized as shown in Figure 12[31], and diluted to a concentration of 1.65 mg/mL. Mats were first conformally treated using a vacuum assisted Spray-LbL technique by alternately spraying with PDAC and $TiO_2$ solutions titrated to pH 10 to develop 25-bilayer coatings. To accomplish this, four inch diameter circles of electrospun Nylon were cut and mounted on coarse mesh stainless steel wire cloth (9x9 mesh) which had been previously fixed in the mouth of a large funnel. The other end of the funnel was connected via rubber tubing to an adjustable-flow single stage vacuum generator operating on compressed air, which was adjusted prior to operation to set the flow rate of air through the electrospun mat during spray deposition. The flow rate, and hence Re number, were determined using a high sensitivity anemometer. During operation the mat was held in place on the wire mesh only by vacuum. Atomized sprays of solutions were formed using modified air-brushes assembled into an automated system, and driven by compressed ultra-pure argon regulated to 20 psi. Cationic PDAC (150,000 $M_w$, 20% aqueous solution) (Aldrich) solution was first sprayed for 3 seconds at a rate of 0.2 mL/s at a sufficient distance and cone angle to reach the entire cross section of the mounted mat simultaneously. Two seconds later pH 10 rinse water was sprayed from a similar distance for 10 seconds, and allowed 2 seconds for the bulk to be removed by vacuum. This half cycle was repeated for the anionic $TiO_2$, and the total cycle (34 seconds) was repeated 25 times to develop the conformal coating.

Vacuum was removed and the mat flipped and remounted. No further drying time was necessary, and the still-damp mat was easily mounted on the same stainless steel screen. Bridged coatings were formed using LPEI (25,000 $M_w$) (Polysciences), PAA (15,000 $M_w$, 35% aqueous solution) (Aldrich), PAMAM (G4, 22% solution in methanol) (Dendritech), SPS (1,000,000 $M_w$) (Aldrich) and PDAC prepared as 0.02 M solutions, based on the repeat unit molecular weight, in Milli-Q water. While the same spray geometry was used, the time between sprays was increased from 2 seconds to 6. In the absence of vacuum solutions were observed to cascade down the mat surface, and therefore were allowed greater rest time (50 second cycle). PAMAM and PAA titrated to pH 4 or SPS and PDAC titrated to pH 10 were applied to develop 50-bilayer coatings, or LPEI and PAA titrated to pH 5 to develop 100-bilayer coatings.

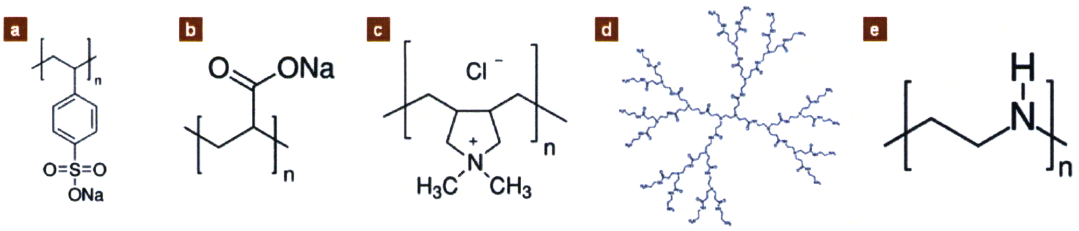

**Figure 50. Polyelectrolyte chemical structures**

Chemical structure of polyelectrolytes deposited using the Layer-by-Layer process in this work. Anionic species **a**, poly(sodium 4-styrenesulfonate), SPS (1,000,000 $M_w$), and **b**, poly(acrylic acid) sodium salt, PAA (15,000 $M_w$), as well as cationic species **c**, poly(diallyldimethylammonium chloride), PDAC (150,000 $M_w$), **d**, poly(amidoamine) dendrimer, PAMAM (G4, but drawn here as G2 for clarity), and **e**, linear poly(ethyleneimine), LPEI (25,000 $M_w$).

Characterization: Mats were coated with a 10 nm layer of Au/Pd and imaged using a JEOL JSM-6060 Scanning Electron Microscope. Average fiber diameter was determined by measuring 40 to 60 individual fibers on both sides of the electrospun mat. Surface area measurements were performed by BET (Micromeritics, ASAP 2020), and verified using both nitrogen and krypton as the adsorbent gas.

Permeation Testing: Treated mats were mounted in a stainless steel permeation cell and subjected to a saturated vapor of CEES (Aldrich) evolving from a 3 μL drop[31]. Meanwhile a stream of ultrapure compressed air (AirGas) was passed at 50 SCCM beneath the sample and analyzed using a Total Hydrocarbon Analyzer (Gow-MAC Instruments, Series 23-550) equipped with a flame ionization detector. During UV testing the photocatalytic side of the material was also exposed to a UV spot source (Dymax, Blue Wave 200) filtered to 50 mW/cm$^2$ intensity. Note, although CEES is a less toxic simulant for HD mustard gas extreme caution should still be exercised when working with it. Water vapor permeation tests were conducted using the Dynamic Moisture Permeation Cell[161] shown schematically in Figure 51, by passing air at two different relative humidity values over opposite sides of the treated mat and measuring the change in water vapor in each stream. To best approximate the $\Delta P = 0$ condition (i.e. no pressure gradient between streams, thus no convection driving water vapor mass transport) several data points are collected at $\Delta P$ near zero, as shown in Figure 52, and interpolated.

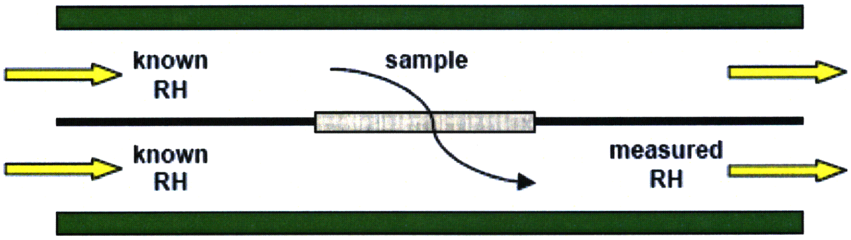

**Figure 51. Dynamic Moisture Permeation Cell**

Water vapor permeation test operating in parallel flow. A sample of known cross-sectional area is mounted between two aluminum plates, while two streams of known relative humidity and flow rate are passed across either side of the sample. Since it is difficult to maintain exactly zero pressure gradient (i.e. to guarantee no convective flow) across a highly porous sample, a range of $\Delta P$ values very near zero are used and the zero $\Delta P$ condition is interpolated.

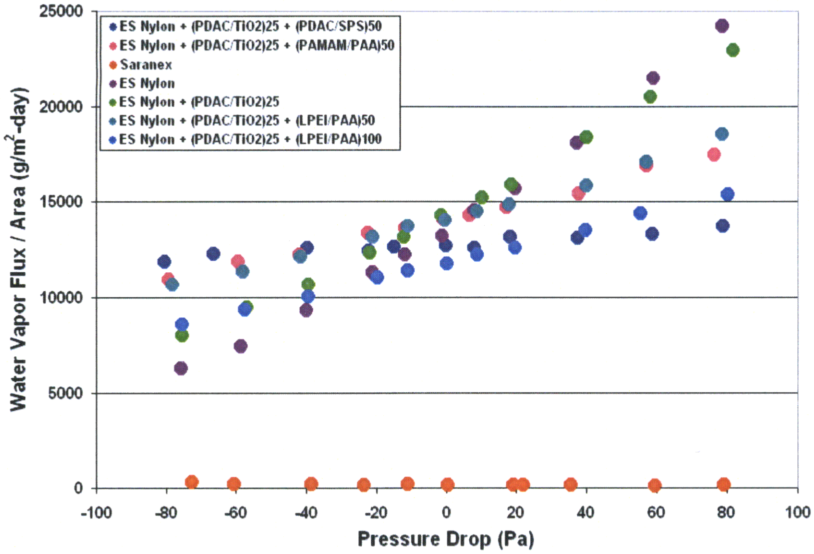

**Figure 52. DMPC water permeation test data**

Actual data collected from Dynamic Moisture Permeation test, prior to interpolation. Pressure gradients from ΔP = -80 to 80 Pa were tested to develop a linear relationship which can be fitted to the ΔP = 0 conditions which were reported in Table 6.

# Conclusion and Future Recommendations

The validity and versatility of the spray-assisted LbL (Spray-LbL) technology has been demonstrated by depositing both weak and strong polyelectrolyte films, hydrogen bonded films, dendritic compounds and nanoparticles, broadening its range of future applications. Most importantly, the Spray-LbL technique presents a method by which laboratory-scale LbL solutions can be applied in quantities that are commercially viable. This platform technology is then applied to generate three novel electrostatically assembled coatings for protection against a range of acutely toxic compounds including several chemical warfare agents and toxic industrial compounds.

First, Spray-LbL is used to create photocatalytic coatings capable of degrading chemical warfare agents, which also exhibit much greater water vapor transport rates as compared to an inert rubber barrier material. Second, metal-ion doped polymeric coatings are deposited which are shown to be effective treatments for air filtration, functionalizing existing filters with the ability to strongly bind toxic industrial compounds such as ammonia or cyanide gases, as well as chemical warfare agent simulants such as chloroethyl ethyl sulfide. Finally, the Spray-LbL technique is used to asymmetrically functionalize electrospun materials with multiple coatings. By simply varying the flow rate of charged species passing through an electrospun material during Spray-LbL deposition, individual fibers within the matrix can be conformally functionalized for ultra-high surface area catalysis, or bridged to form a networked sublayer with complimentary properties. Selectively-reactive gas purification membranes have been created and modeled, suggesting several future applications of this technology such as self-cleaning fabrics, water purification, and protein functionalization of scaffolds for tissue engineering.

In the 92 years since the first battlefield deployment of chemical warfare agents, scientists have been able to focus on primarily two categories of threats grouped by their similar routes of toxicity within the body. The future of chemical protection will likely be significantly more challenging, due to the ease of acquisition both of chemical precursors and information, as the number and quantities of acutely toxic agents increase. Protective measures will be required to incorporate more chemical functionalities to target more compounds, and as complexity increases, the selectivity of chem-protective measures will necessarily increase if the solutions are to be viable in the real world. Platform technologies, such as the electrostatic assembly techniques described here, which are able to simultaneously incorporate multiple functionalities and are as rapidly adaptable as the enemies generating the threat will be essential. Ideally, the number of targeting moieties that can be introduced into LbL films will continue to grow, developing the library of acutely toxic compounds that can be safely degraded or bound. As threats emerge, this library can be used to generate custom tuned air and water filters, as well as treated textiles that can protect soldiers and HAZMAT workers from a broad range of compounds without interfering with their primary functions. The small range of protection demonstrated here is only the beginning of the necessary capabilities, but serves as solid base on which to build.

# References

1 Langmuir, I., *J. Am. Chem. Soc.* 41 (6), 868-934 (1919).
2 Blodgett, K.B., *J. Am. Chem. Soc.* 56 (2), 495-495 (1934).
3 Iler, R.K., *Journal of Colloid and Interface Science* 21 (6), 569-594 (1966).
4 Haller, I., *J. Am. Chem. Soc.* 100 (26), 8050-8055 (1978).
5 Decher, G., *Science* 277 (5330), 1232-1237 (1997).
6 Decher, G., Hong, J.D., & Schmitt, J., *Thin Solid Films* 210-211 (Part 2), 831-835 (1992).
7 Shiratori, S.S. & Rubner, M.F., *Macromolecules* 33 (11), 4213-4219 (2000).
8 Yoo, D., Shiratori, S.S., & Rubner, M.F., *Macromolecules* 31 (13), 4309-4318 (1998).
9 Lvov, Y., Ariga, K., Ichinose, I., & Kunitake, T., *J. Am. Chem. Soc.* 117 (22), 6117-6123 (1995).
10 Tsukruk, V.V., Rinderspacher, F., & Bliznyuk, V.N., *Langmuir* 13 (8), 2171-2176 (1997).
11 Fendler, J.H., *Chem Mater* 8 (8), 1616-1624 (1996).
12 Kotov, N.A., Dekany, I., & Fendler, J.H., *J. Phys. Chem.* 99 (35), 13065-13069 (1995).
13 Dubas, S.T. & Schlenoff, J.B., *Macromolecules* 32 (24), 8153-8160 (1999).
14 Caruso, F., Caruso, R.A., & Mohwald, H., *Science* 282 (5391), 1111-1114 (1998).
15 Bertrand, P., Jonas, A., Laschewsky, A., & Legras, R., *Macromol. Rapid Commun.* 21 (7), 319-348 (2000).
16 Philipp, B., Dautzenberg, H., Linow, K.J., Kotz, J., & Dawydoff, W., *Prog. Polym. Sci.* 14 (1), 91-172 (1989).
17 Sukhishvili, S.A. & Granick, S., *Macromolecules* 35 (1), 301-310 (2002).
18 Lutkenhaus, J.L. & Hammond, P.T., *Soft Matter* 3 (7), 804-816 (2007).
19 Tang, Z.Y., Wang, Y., Podsiadlo, P., & Kotov, N.A., *Adv. Mater.* 18 (24), 3203-3224 (2006).
20 Caruso, F., *Adv. Mater.* 13 (1), 11-+ (2001).
21 Antipov, A.A. & Sukhorukov, G.B., *Advances in Colloid and Interface Science* 111 (1-2), 49-61 (2004).
22 Hiller, J., Mendelsohn, J.D., & Rubner, M.F., *Nat Mater* 1 (1), 59-63 (2002).
23 Hammond, P.T., *Adv. Mater.* 16 (15), 1271-1293 (2004).
24 Lawson, W.E. & Reid, E.E., *J. Am. Chem. Soc.* 47 (11), 2821-2836 (1925).
25 Bismuth, C., Borron, S.W., Baud, F.J., & Barriot, P., *Toxicology Letters* 149, 11-18 (2004).
26 Munro, N.B. *et al.*, *Environ. Health Perspect.* 107 (12), 933-974 (1999).
27 Yang, Y.C., *Accounts Chem. Res.* 32 (2), 109-115 (1999).
28 Yang, Y.C., Baker, J.A., & Ward, J.R., *Chem. Rev.* 92 (8), 1729-1743 (1992).
29 Davis, W.T., Hood, C.C., & Dever, M., *Separation Science and Technology* 30 (7-9), 1309-1324 (1995).
30 Krogman, K.C., Zacharia, N.S., Schroeder, S., & Hammond, P.T., *Langmuir* 23 (6), 3137-3141 (2007).

31 Krogman, K.C., Zacharia, N.S., Grillo, D.M., & Hammond, P.T., *Chem Mater* 20 (5), 1924-1930 (2008).
32 Krogman, K.C., Lyon, K.F., & Hammond, P.T., *Journal of Physical Chemistry B* 112 (46), 14453-14460 (2008).
33 Krogman, K.C., Lowery, J.L., Zacharia, N.S., Rutledge, G.C., & Hammond, P.T., *Nature Materials* advance online publication, 19 April 2009.
34 Lowman, G.M., Tokuhisa, H., Lutkenhaus, J.L., & Hammond, P.T., *Langmuir* 20 (22), 9791-9795 (2004).
35 Decher, G., Hong, J.D., & Schmitt, J., *Thin Solid Films* 210 (1-2), 831-835 (1992).
36 Borukhov, I., Andelman, D., & Orland, H., *Macromolecules* 31 (5), 1665-1671 (1998).
37 DeLongchamp, D.M. & Hammond, P.T., *Chem Mater* 15 (5), 1165-1173 (2003).
38 Park, S.Y., Barrett, C.J., Rubner, M.F., & Mayes, A.M., *Macromolecules* 34 (10), 3384-3388 (2001).
39 Jang, W.S. & Grunlan, J.C., *Rev. Sci. Instrum.* 76 (10), 4 (2005).
40 Schlenoff, J.B., Dubas, S.T., & Farhat, T., *Langmuir* 16 (26), 9968-9969 (2000).
41 Izquierdo, A., Ono, S.S., Voegel, J.C., Schaaff, P., & Decher, G., *Langmuir* 21 (16), 7558-7567 (2005).
42 Porcel, C.H. *et al.*, *Langmuir* 21 (2), 800-802 (2005).
43 Ladam, G. *et al.*, *Langmuir* 16 (3), 1249-1255 (2000).
44 Park, S.Y., Rubner, M.F., & Mayes, A.M., *Langmuir* 18 (24), 9600-9604 (2002).
45 Schmitt, J. *et al.*, *Macromolecules* 26 (25), 7058-7063 (1993).
46 Choi, J. & Rubner, M.F., *Macromolecules* 38 (1), 116-124 (2005).
47 Zacharia, N.S., DeLongchamp, D.M., Modestino, M., & Hammond, P.T., *Macromolecules* 40 (5), 1598-1603 (2007).
48 Lutkenhaus, J.L., Hrabak, K.D., McEnnis, K., & Hammond, P.T., *J. Am. Chem. Soc.* 127 (49), 17228-17234 (2005).
49 Chen, W. & McCarthy, T.J., *Macromolecules* 30 (1), 78-86 (1997).
50 Ma, M.L., Mao, Y., Gupta, M., Gleason, K.K., & Rutledge, G.C., *Macromolecules* 38 (23), 9742-9748 (2005).
51 Sabne, M.B. *et al.*, *Journal of Applied Polymer Science* 58 (8), 1275-1278 (1995).
52 Felix, O., Zheng, Z.Q., Cousin, F., & Decher, G., *C. R. Chim.* 12 (1-2), 225-234 (2009).
53 Kolasinska, M., Krastev, R., Gutberlet, T., & Warszynski, P., *Langmuir* 25 (2), 1224-1232 (2009).
54 Ladhari, N. *et al.*, *Colloid Surf. A-Physicochem. Eng. Asp.* 322 (1-3), 142-147 (2008).
55 Lu, C.H., Donch, I., Nolte, M., & Fery, A., *Chem Mater* 18 (26), 6204-6210 (2006).
56 Laugel, N. *et al.*, *Journal of Colloid and Interface Science* 324 (1-2), 127-133 (2008).
57 Porcel, C. *et al.*, *Langmuir* 22 (9), 4376-4383 (2006).
58 Porcel, C. *et al.*, *Langmuir* 23 (4), 1898-1904 (2007).
59 Merrill, M.H. & Sun, C.T., *Nanotechnology* 20 (7), 7 (2009).
60 Vozar, S. *et al.*, *Rev. Sci. Instrum.* 80 (2), 5 (2009).

61 Michel, A. *et al.*, *Langmuir* 21 (17), 7854-7859 (2005).
62 Kleinhammes, A. *et al.*, *Chem. Phys. Lett.* 411 (1-3), 81-85 (2005).
63 Martyanov, I.N. & Klabunde, K.J., *Environ. Sci. Technol.* 37 (15), 3448-3453 (2003).
64 Thompson, T.L., Panayotov, D.A., Yates, J.T., Martyanov, I., & Klabunde, K., *Journal of Physical Chemistry B* 108 (46), 17857-17865 (2004).
65 Vorontsov, A.V., Lion, C., Savinov, E.N., & Smirniotis, P.G., *J. Catal.* 220 (2), 414-423 (2003).
66 Panayotov, D., Kondratyuk, P., & Yates, J.T., *Langmuir* 20 (9), 3674-3678 (2004).
67 Rodrigues, S., Ums, S., Martyanov, I., & Klabunde, K., *Chem. Commun.* (21), 2476-2477 (2004).
68 Madhugiri, S., Sun, B., Smirniotis, P.G., Ferraris, J.P., & Balkus, K.J., *Microporous Mesoporous Mat.* 69 (1-2), 77-83 (2004).
69 Yusuf, M.M., Imai, H., & Hirashima, H., *J. Sol-Gel Sci. Technol.* 25 (1), 65-74 (2002).
70 Sasaki, T. *et al.*, *Chem Mater* 14 (8), 3524-3530 (2002).
71 Sasaki, T., Ebina, Y., Watanabe, M., & Decher, G., *Chem. Commun.* (21), 2163-2164 (2000).
72 Shibata, T., Sakai, N., Fukuda, K., Ebina, Y., & Sasaki, T., *Phys. Chem. Chem. Phys.* 9 (19), 2413-2420 (2007).
73 Lvov, Y., Ariga, K., Onda, M., Ichinose, I., & Kunitake, T., *Langmuir* 13 (23), 6195-6203 (1997).
74 Lee, D., Rubner, M.F., & Cohen, R.E., *Nano Lett* 6 (10), 2305-2312 (2006).
75 Fick, A., *The London, Edinburgh and Dublin Philosophical Magazine and Journal of Science* 10, 30-39 (1855).
76 Fick, A., *Journal of Membrane Science* 100 (1), 33-38 (1995).
77 Wijmans, J.G. & Baker, R.W., *Journal of Membrane Science* 107 (1-2), 1-21 (1995).
78 Klare, M., Scheen, J., Vogelsang, K., Jacobs, H., & Broekaert, J.A.C., *Chemosphere* 41 (3), 353-362 (2000).
79 VPL Molecular Spectroscopic Database.
80 Benvenutti, E.V. & Gushikem, Y., *J. Braz. Chem. Soc.* 9 (5), 469-472 (1998).
81 Baldwin, K.G.H. & Watts, R.O., *Journal of Chemical Physics* 87 (2), 873-879 (1987).
82 Evans, C.S., Hunneman, R., Seeley, J.S., & Whatley, A., *Appl. Optics* 15 (11), 2736-2745 (1976).
83 Caruso, F., Lichtenfeld, H., Donath, E., & Mohwald, H., *Macromolecules* 32 (7), 2317-2328 (1999).
84 Hoogeveen, N.G., Cohen Stuart, M.A., Fleer, G.J., & Bohmer, M.R., *Langmuir* 12 (15), 3675-3681 (1996).
85 Kellogg, G.J. *et al.*, *Langmuir* 12 (21), 5109-5113 (1996).
86 Losche, M., Schmitt, J., Decher, G., Bouwman, W.G., & Kjaer, K., *Macromolecules* 31 (25), 8893-8906 (1998).
87 Mermut, O. & Barrett, C.J., *Journal of Physical Chemistry B* 107 (11), 2525-2530 (2003).

88 Riegler, H. & Essler, F., *Langmuir* 18 (17), 6694-6698 (2002).
89 Salomaki, M. & Kankare, J., *Langmuir* 20 (18), 7794-7801 (2004).
90 Dubas, S.T. & Schlenoff, J.B., *Macromolecules* 34 (11), 3736-3740 (2001).
91 Farhat, T.R. & Schlenoff, J.B., *Langmuir* 17 (4), 1184-1192 (2001).
92 Hsieh, M.C., Farris, R.J., & McCarthy, T.J., *Macromolecules* 30 (26), 8453-8458 (1997).
93 Laurent, D. & Schlenoff, J.B., *Langmuir* 13 (6), 1552-1557 (1997).
94 Levasalmi, J. & McCarthy, T.J., *Macromolecules* 30 (6), 1752-1757 (1997).
95 Schlenoff, J.B. & Dubas, S.T., *Macromolecules* 34 (3), 592-598 (2001).
96 Schlenoff, J.B., Ly, H., & Li, M., *J. Am. Chem. Soc.* 120 (30), 7626-7634 (1998).
97 Balachandra, A.M., Dai, J.H., & Bruening, M.L., *Macromolecules* 35 (8), 3171-3178 (2002).
98 Schuetz, P. & Caruso, F., *Adv Funct Mater* 13 (12), 929-937 (2003).
99 Joly, S. *et al.*, *Langmuir* 16 (3), 1354-1359 (2000).
100 Morrison, R.W., Report No. ECBC-TR-135, 2001.
101 Rossin, J.A. & Morrison, R.W., *Carbon* 29 (7), 887-892 (1991).
102 Rossin, J.A. & Morrison, R.W., *Carbon* 31 (4), 657-659 (1993).
103 McDowall, L., Report No. DSTO-GD-0446, 2005.
104 Dong, H. & Bell, T., *Surf Coat Tech* 111 (1), 29-40 (1999).
105 Rao, G.R., Monar, K., Lee, E.H., & Treglio, J.R., *Surf Coat Tech* 64 (2), 69-74 (1994).
106 Rivas, B.L., Schiappacasse, L.N., Pereira, U.E., & Moreno-Villoslada, I., *Polymer* 45 (6), 1771-1775 (2004).
107 Roma-Luciow, R., Sarraf, L., & Morcellet, M., *Eur Polym J* 37 (9), 1741-1745 (2001).
108 Miyajima, T., Mori, M., & Ishiguro, S., *J Colloid Interf Sci* 187 (1), 259-266 (1997).
109 Sebastian, N., George, B., & Mathew, B., *Polym Degrad Stabil* 60 (2-3), 371-375 (1998).
110 De Stefano, C., Gianguzza, A., Piazzese, D., & Sammartano, S., *Mar Chem* 86 (1-2), 33-44 (2004).
111 Pearson, R.G., *J. Amer. Chem. Soc.* 85 (22), 3533 (1963).
112 Pearson, R.G., *Science* 151 (3707), 172 (1966).
113 Morlay, C., Cromer, M., Mouginot, Y., & Vittori, O., *Talanta* 45 (6), 1177-1188 (1998).
114 Gregor, H.P., Luttinger, L.B., & Loebl, E.M., *J. Phys. Chem.* 59, 34 (1954).
115 Koide, M., Tsuchida, E., & Kurimura, Y., *Macromol Chem Phys* 182 (2), 359-365 (1981).
116 test note
117 Ma, Y., Sun, J., & Shen, J., *Chem. Mater.* 19, 5058 (2007).
118 Deacon, G.B. & Phillips, R.J., *Coord. Chem. Rev.* 33, 227 (1980).
119 Jobson, E., Baiker, A., & Wokaun, A., *J Mol Catal* 60 (3), 399-416 (1990).
120 Allen, E.C. & Beers, K.J., *Polymer* 46 (2), 569-573 (2005).
121 Oku, M. & Hirokawa, K., *J Appl Phys* 50 (10), 6303-6308 (1979).
122 Tilley, R.I., *Aust. J. Chem.* 43, 1573 (1990).
123 Megson, F.H. & Beacham, M.T., USA Patent No. 3,464,847 (1970).

124 O'Brien, S.J. & Beacham, M.T., USA Patent No. 3,482,927 (1970).
125 Bearden, J.A. & Burr, A.F., *Rev. Mod. Phys.* 39, 125 (1967).
126 Fuggle, J.C. & Martensson, N., *Electron Spectrosc. Relat. Phenom.* 21, 275 (1980).
127 Bretsche, M.S., *Science* 181 (4100), 622-629 (1973).
128 Rothman, J.E. & Lenard, J., *Science* 195 (4280), 743-753 (1977).
129 Sridhar, S., Smitha, B., & Aminabhavi, T.M., *Sep. Purif. Rev.* 36 (2), 113-174 (2007).
130 Yoo, P.J. *et al.*, *Nat Mater* 5 (3), 234-240 (2006).
131 Fridrikh, S.V., Yu, J.H., Brenner, M.P., & Rutledge, G.C., *Phys Rev Lett* 90 (14), 144502 (2003).
132 Lee, J.A. *et al.*, *Adv. Mater.* 21 (12), 1252-1256 (2009).
133 Chen, L., Bromberg, L., Hatton, T.A., & Rutledge, G.C., *Polymer* 49 (5), 1266-1275 (2008).
134 Chen, L. *et al.*, *Journal of Materials Chemistry* in press (2009).
135 Blossey, R., *Nat Mater* 2 (5), 301-306 (2003).
136 Daoud, W.A. *et al.*, *Chem Mater* 20 (4), 1242-1244 (2008).
137 Peercy, P.S., *Nature* 406 (6799), 1023-1026 (2000).
138 Simon, P. & Gogotsi, Y., *Nat Mater* 7 (11), 845-854 (2008).
139 Tarascon, J.M. & Armand, M., *Nature* 414 (6861), 359-367 (2001).
140 Yoon, J. *et al.*, *Nat Mater* 7 (11), 907-915 (2008).
141 Shin, Y.M., Hohman, M.M., Brenner, M.P., & Rutledge, G.C., *Polymer* 42 (25), 9955-9967 (2001).
142 Deen, W.M., *Analysis of Transport Phenomena*, 6th ed. (Oxford University Press, New York, NY, 1998).
143 Crank, J., *The Mathematics of Diffusion*, 2nd ed. (Oxford University Press, New York, 1975).
144 Frisch, H.L., *Journal of Chemical Physics* 36 (2), 510-516 (1962).
145 Siegel, R.A. & Cussler, E.L., *Journal of Membrane Science* 229 (1-2), 33-41 (2004).
146 Stern, S.A., *Journal of Polymer Science* 6, 1933-1934 (1968).
147 Peinemann, K., Abetz, V., & Simon, P.F.W., *Nat Mater* 6 (12), 992-996 (2007).
148 Mi, F. *et al.*, *Biomaterials* 22 (2), 165-173 (2001).
149 Fogler, H.S., *Elements of Chemical Reaction Engineering*. (Prentice Hall PTR, Upper Saddle River, NJ, 1999).
150 Shannon, M.A. *et al.*, *Nature* 452 (7185), 301-310 (2008).
151 Corry, B., *J. Phys. Chem. B* 112 (5), 1427-1434 (2008).
152 Ma, M.L. *et al.*, *Adv. Mater.* 19 (2), 255-259 (2007).
153 Cao, Q. *et al.*, *Nature* 454 (7203), 495-U494 (2008).
154 Hall, L.J. *et al.*, *Science* 320 (5875), 504-507 (2008).
155 Barnes, C.P., Sell, S.A., Boland, E.D., Simpson, D.G., & Bowlin, G.L., *Advanced Drug Delivery Reviews* 59 (14), 1413-1433 (2007).
156 Dankers, P.Y.W., Harmsen, M.C., Brouwer, L.A., Van Luyn, M.J.A., & Meijer, E.W., *Nat Mater* 4 (7), 568-574 (2005).
157 Grafahrend, D. *et al.*, *Biotechnology and Bioengineering* 101 (3), 609-621 (2008).

158 Heydarkhan-Hagvall, S., Schenke-Layland, K., & Dhanasopon, A.P., *Biomaterials* 29 (19), 2907-2914 (2008).

159 Zhang, X.H., Baughman, C.B., & Kaplan, D.L., *Biomaterials* 29 (14), 2217-2227 (2008).

160 Park, J.H., Kim, B.S., Yoo, Y.C., Khil, M.S., & Kim, H.Y., *Journal of Applied Polymer Science* 107 (4), 2211-2216 (2008).

161 Gibson, P.W., Kendrick, C.E., & Rivin, D., United States Patent No. 6,119,506 (1999).

# Appendix

A ladder logic program written using the ZelioSoft software to control the micro-relay logic of the Spray-LbL system can be found on the following pages. This particular recipe accomplishes the following spray sequence

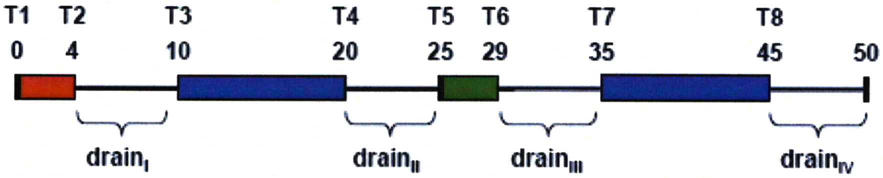

where the cationic solution (represented in red) is sprayed for 4 seconds and allowed to drain for 6 seconds, after which rinse water is sprayed for 10 seconds and allowed to drain for 5 seconds. The second half of the cycle proceeds with the anionic solution spraying for 4 seconds and draining for 6 seconds, followed by a second rinse for 10 seconds and 5 seconds of drain time to complete the cycle. The cycle can be repeated n times to create (cation/anion)$_n$ spray-LbL coatings. Ladder logic operates just like it sounds, as a ladder made of rungs. When the top rung is powered from the left of the diagram the current progresses logically to the right, then on to the next rung down. As long as the top rung remains powered the rest of the system progresses through the logic. If the top rung is de-powered the system halts, forming a simple yet effective E-stop.

The following table explains the various timers used by this recipe as well as the mathematical constraints placed on timers T9 and TA to ensure electrical continuity of the looped ladder logic. T1, T3, T5 and T7 refer to absolute times in the spray cycle at which sprays begin, while T2, T4, T6 and T8 refer to relative times and define how long each spray lasts.

| **Timer** | **Explanation** | **Mathematical Constraints** |
|---|---|---|
| T1 | Cation Start Time | |
| T2 | Cation Spray Length | |
| T3 | First Rinse Start Time | |
| T4 | First Rinse Spray Length | |
| T5 | Anion Start Time | |
| T6 | Anion Spray Length | |
| T7 | Second Rinse Start Time | |
| T8 | Second Rinse Spray Length | |
| T9 | Electrical Delay | T8 – 1 sec. |
| TA | Reset Cycle | $\text{drain}_{IV}$ + 1 sec. |

## Program diagram

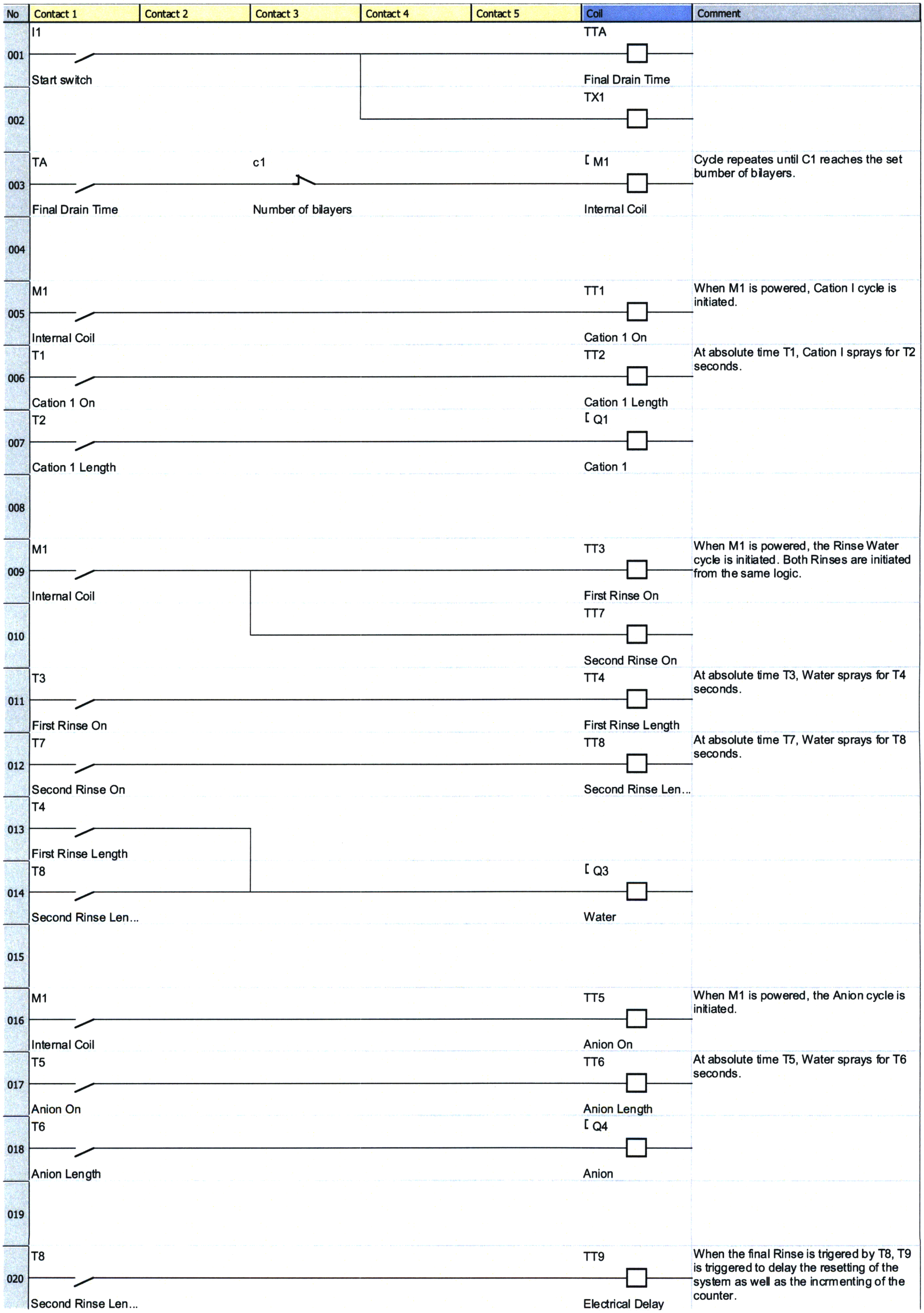

| No | Contact 1 | Contact 2 | Contact 3 | Contact 4 | Contact 5 | Coil | Comment |
|---|---|---|---|---|---|---|---|
| 001 | I1<br>Start switch | | | | | TTA<br>Final Drain Time | |
| 002 | | | | | | TX1 | |
| 003 | TA<br>Final Drain Time | | c1<br>Number of bilayers | | | [ M1<br>Internal Coil | Cycle repeates until C1 reaches the set bumber of bilayers. |
| 004 | | | | | | | |
| 005 | M1<br>Internal Coil | | | | | TT1<br>Cation 1 On | When M1 is powered, Cation I cycle is initiated. |
| 006 | T1<br>Cation 1 On | | | | | TT2<br>Cation 1 Length | At absolute time T1, Cation I sprays for T2 seconds. |
| 007 | T2<br>Cation 1 Length | | | | | [ Q1<br>Cation 1 | |
| 008 | | | | | | | |
| 009 | M1<br>Internal Coil | | | | | TT3<br>First Rinse On | When M1 is powered, the Rinse Water cycle is initiated. Both Rinses are initiated from the same logic. |
| 010 | | | | | | TT7<br>Second Rinse On | |
| 011 | T3<br>First Rinse On | | | | | TT4<br>First Rinse Length | At absolute time T3, Water sprays for T4 seconds. |
| 012 | T7<br>Second Rinse On | | | | | TT8<br>Second Rinse Len... | At absolute time T7, Water sprays for T8 seconds. |
| 013 | T4<br>First Rinse Length | | | | | | |
| 014 | T8<br>Second Rinse Len... | | | | | [ Q3<br>Water | |
| 015 | | | | | | | |
| 016 | M1<br>Internal Coil | | | | | TT5<br>Anion On | When M1 is powered, the Anion cycle is initiated. |
| 017 | T5<br>Anion On | | | | | TT6<br>Anion Length | At absolute time T5, Water sprays for T6 seconds. |
| 018 | T6<br>Anion Length | | | | | [ Q4<br>Anion | |
| 019 | | | | | | | |
| 020 | T8<br>Second Rinse Len... | | | | | TT9<br>Electrical Delay | When the final Rinse is trigered by T8, T9 is triggered to delay the resetting of the system as well as the incrmenting of the counter. |

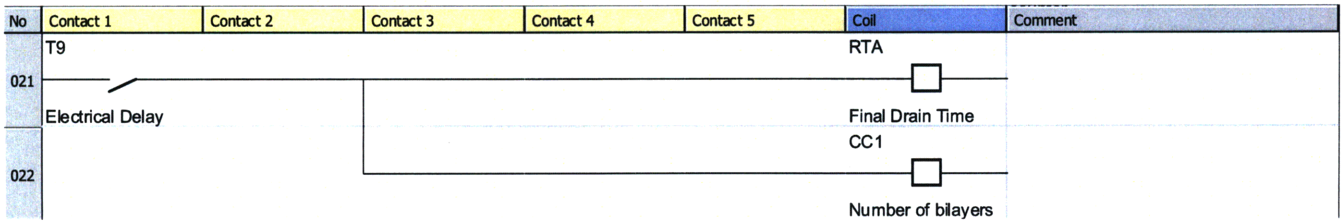

| No | Contact 1 | Contact 2 | Contact 3 | Contact 4 | Contact 5 | Coil | Comment |
|---|---|---|---|---|---|---|---|
| 021 | T9<br>Electrical Delay | | | | | RTA<br>Final Drain Time | |
| 022 | | | | | | CC1<br>Number of bilayers | |

| Quantity | Item | Supplier | Part # | Cost | |
|---|---|---|---|---|---|
| 1 | Zelio Logic Relay Package | Applied Industrial Technologies | SR2PACKFU | $ 300.99 | each |
| 4 | Airbrush - Medium | MyAtomic.com | bad200-1 | $ 56.39 | each |
| 4 | Braided Airbrush Hose - 10' | MyAtomic.com | bad50-2011 | $ 12.00 | each |
| 1 | 1/4" Female Tee | McMaster-Carr | 50785K72 | $ 2.85 | each |
| 2 | 1/4" Male Tee | McMaster-Carr | 4860K442 | $ 11.65 | each |
| 4 | Linear Solenoid | McMaster-Carr | 70155K66 | $ 13.02 | each |
| 1 | Electrical Box | McMaster-Carr | 75065K12 | $ 16.90 | each |
| 16 | quick disconnect terminals | McMaster-Carr | 7243K112 | $ 7.16 | 25 pack |
| 1 | metal fabrication | MIT Machine Shop | | varies | |
| 25 ft. | 18 gauge wire | Radio Shack | 278-567 | $ 6.59 | spool |
| 4 | push on-push off switches | Radio Shack | 275-1565 | $ 2.79 | each |
| 1 | lighted rocker switch | Radio Shack | 275-692 | $ 3.99 | each |
| 2 | fuse holders | Radio Shack | 270-739 | $ 1.99 | 2 pack |
| 1 | 1 amp slow blow fuse | Radio Shack | 270-1021 | $ 2.99 | 4 pack |
| 1 | 1/2 amp fast blow fuse | Radio Shack | 270-1003 | $ 1.99 | 4 pack |
| 1 | 8 x 2 terminal strip | Radio Shack | 274-678 | $ 2.89 | each |

| | | Consumables | | | |
|---|---|---|---|---|---|
| | Jar and Cover 2 oz | MyAtomic.com | bad50-0053 | $ 1.49 | each |
| | Teflon PFA tubing | McMaster-Carr | 51805K32 | $ 1.64 | per foot |

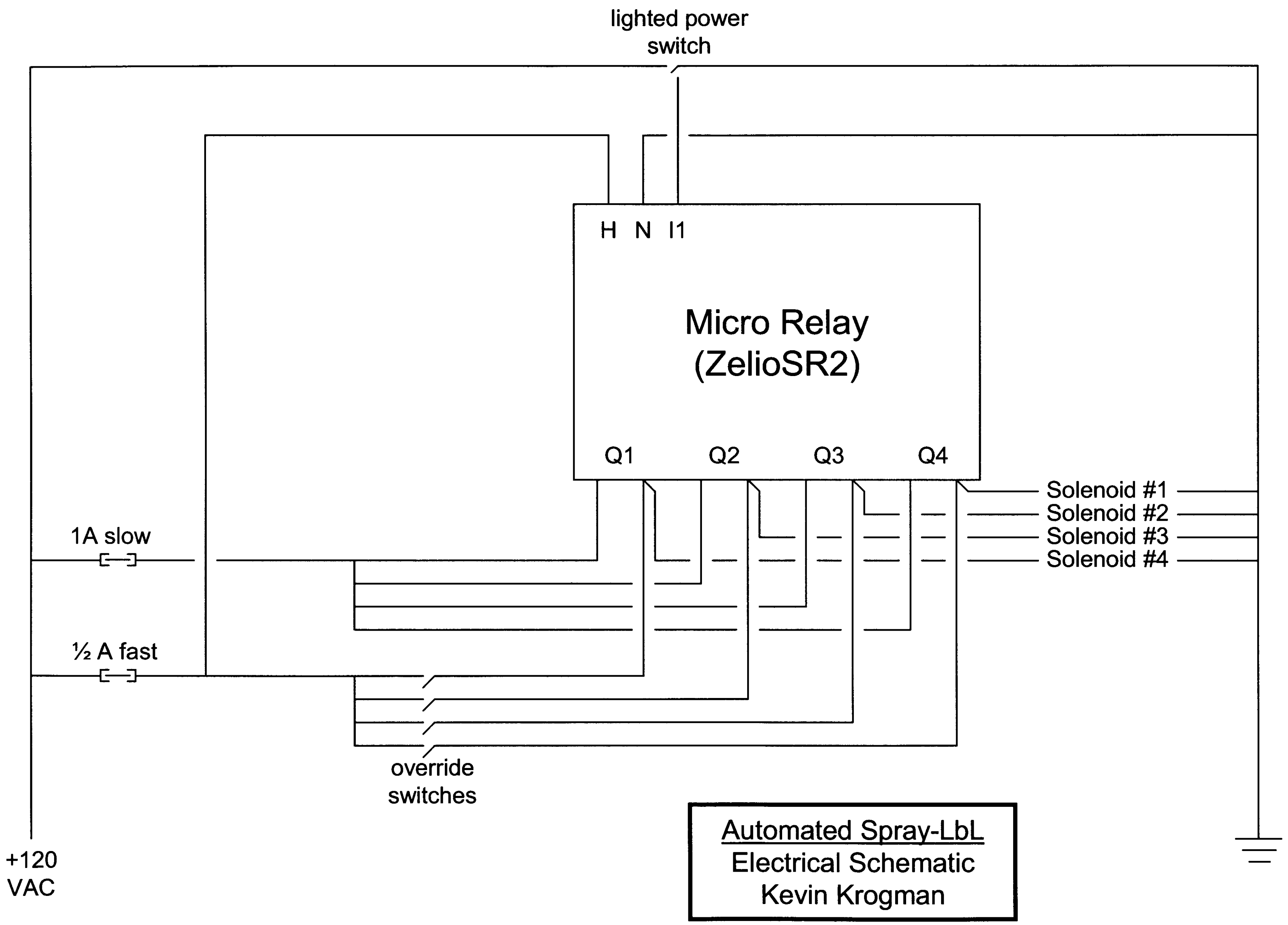

<u>Automated Spray-LbL</u>
Electrical Schematic
Kevin Krogman

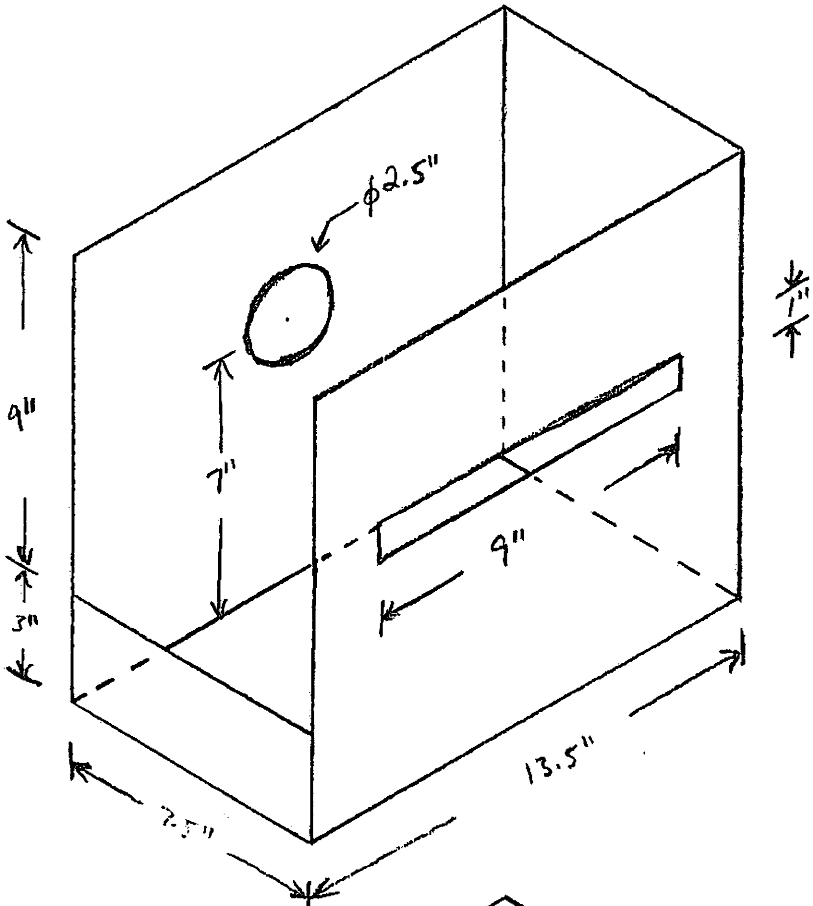

**Part A**

(1/8" aluminum)

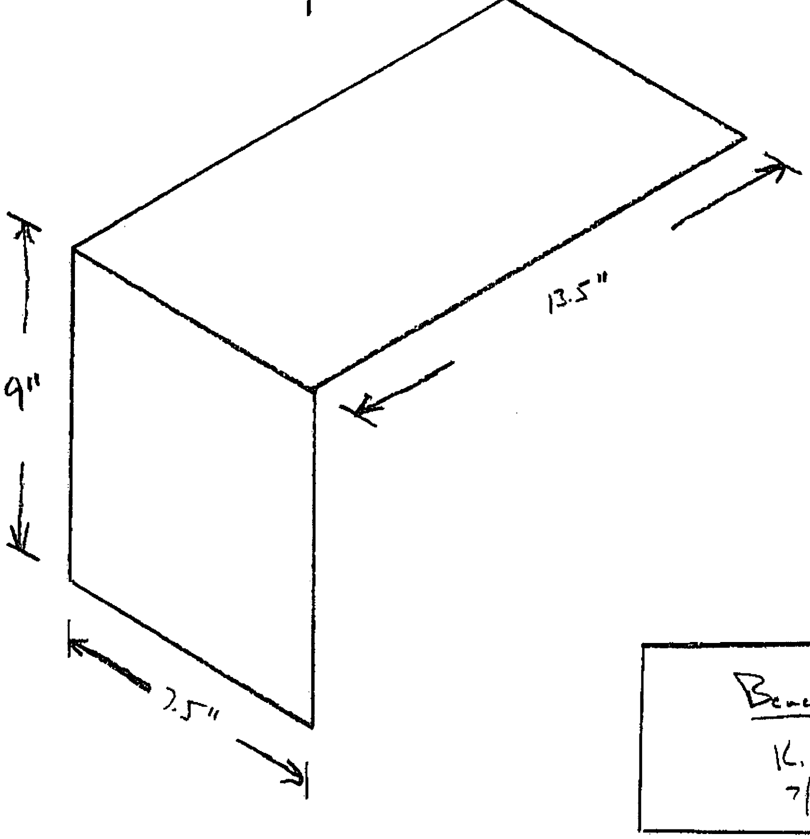

**Part B**

(1/4" plexiglass)

Benchtop Mister

K. Krogman
7/23/08

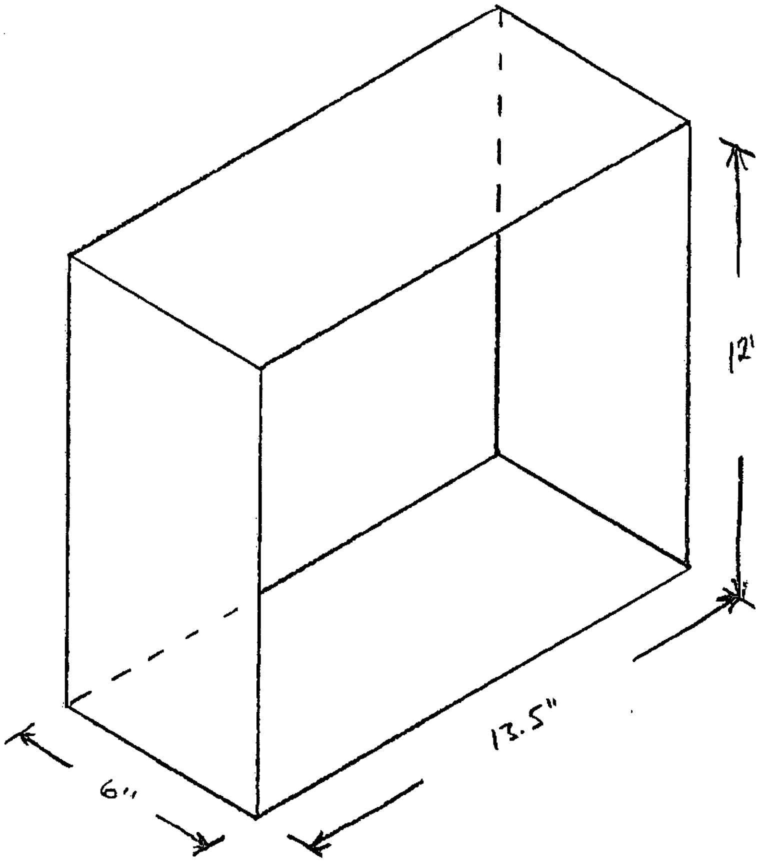

**Part C**

(1/8" aluminum)

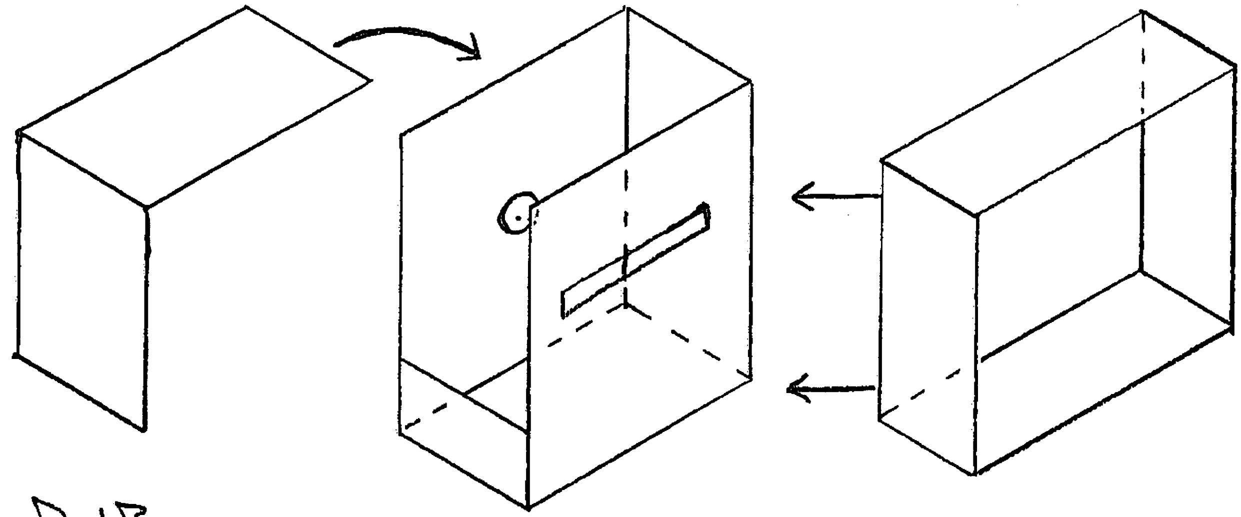

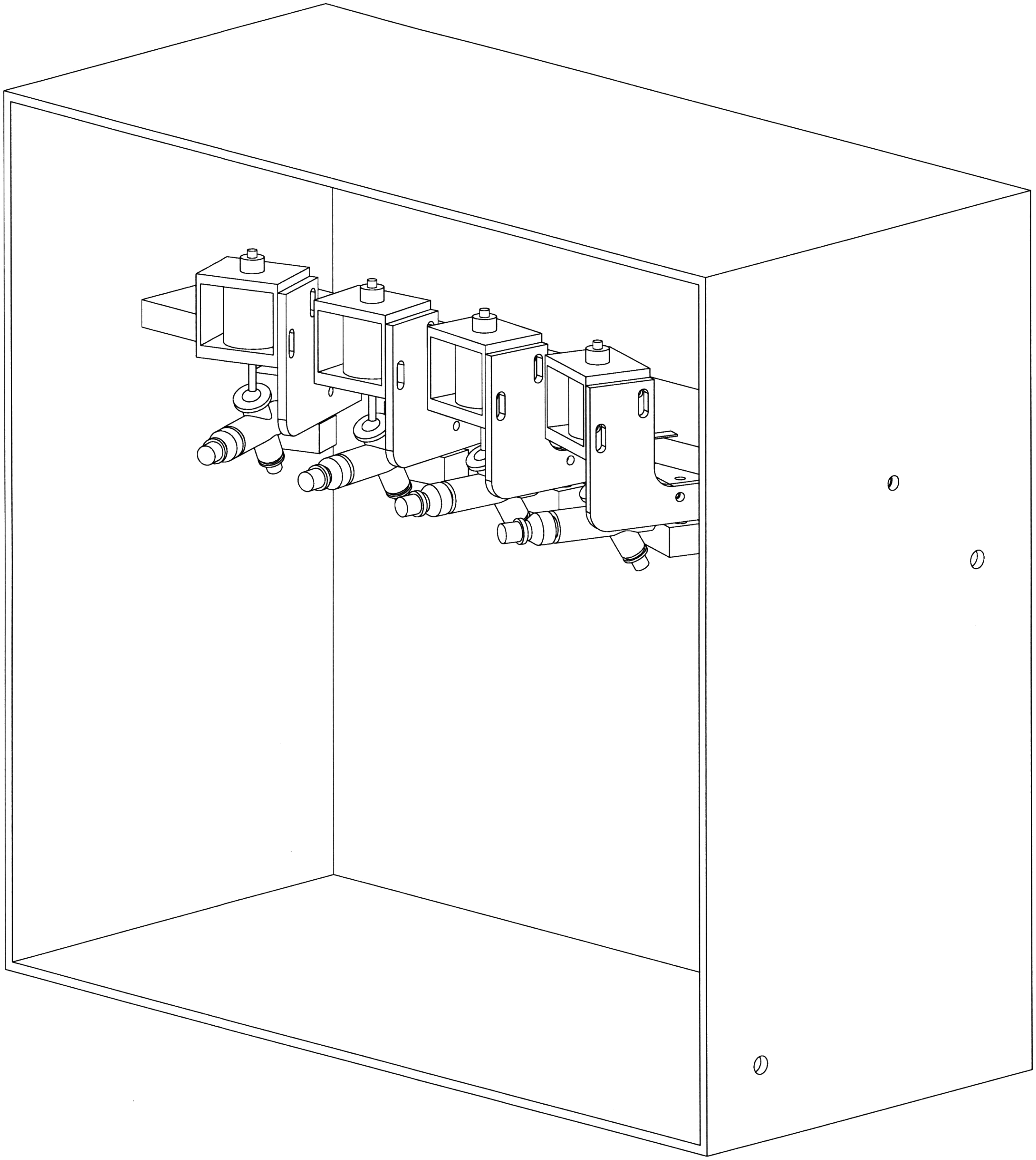

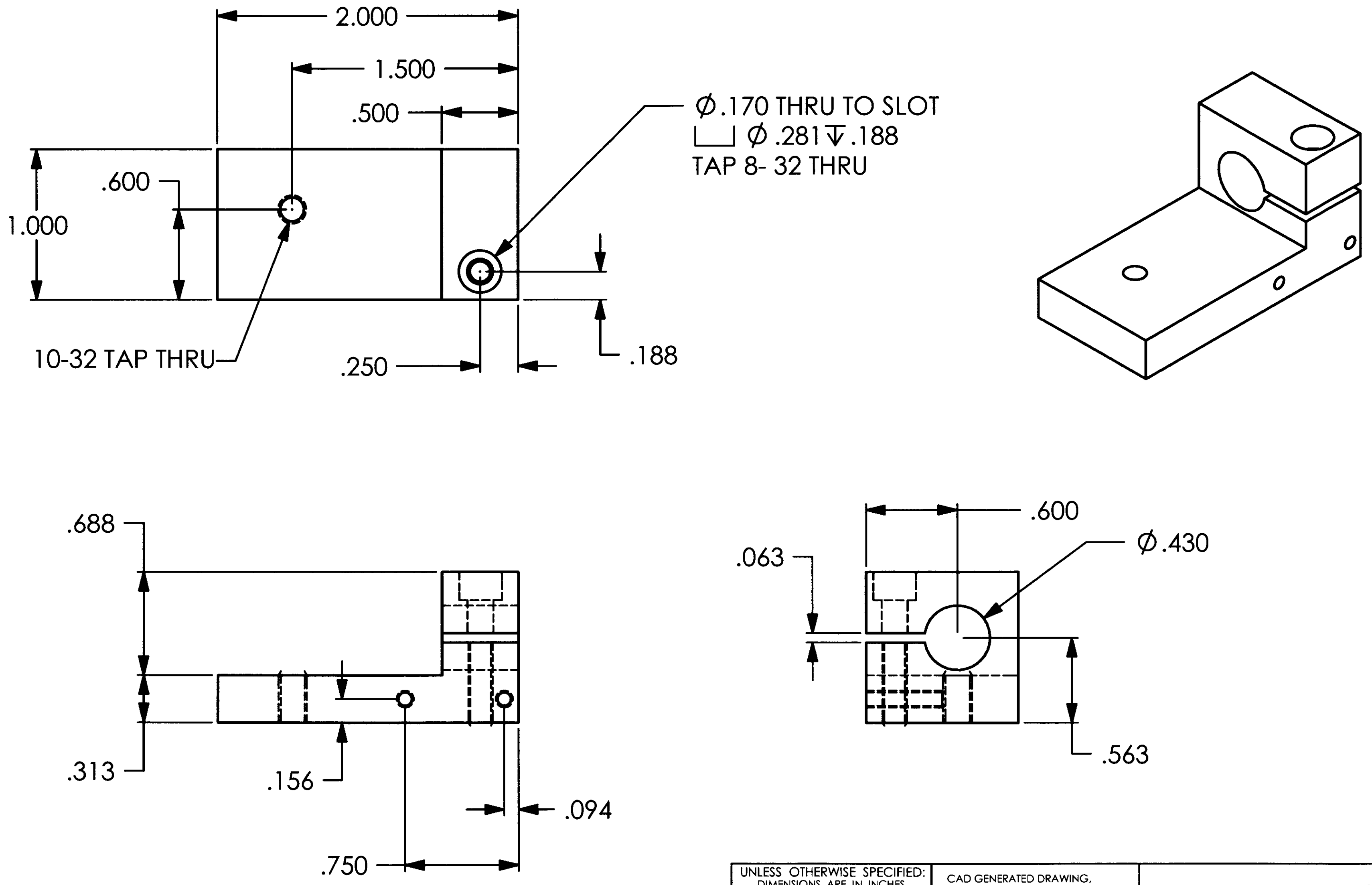

UNLESS OTHERWISE SPECIFIED:
DIMENSIONS ARE IN INCHES
TOLERANCES ARE:

| FRACTIONS | DECIMALS | ANGLES |
|---|---|---|
| ±1/64 | .X±.015<br>.XX±.010<br>.XXX±.005 | ±1° |

ALL MACHINED SURFACES $\overset{32}{\surd}$
CONCENTRICITY .005 TIR
DEBURR AND BREAK SHARP EDGES

MATERIAL ALUMINUM

FINISH ☒

DO NOT SCALE DRAWING

CAD GENERATED DRAWING,
DO NOT MANUALLY UPDATE

| APPROVALS | DATE |
|---|---|
| DRAWN A. GALLANT | 3/19/2009 |
| CHECKED | |
| RESP ENG | |
| MFG ENG | |
| QUAL ENG | |

Massachusetts Institute of Technology

# AIR BRUSH MOUNT

SIZE A | DWG. NO. | REV.

SCALE 1:1 | CAD FILE: | SHEET 1 OF 1

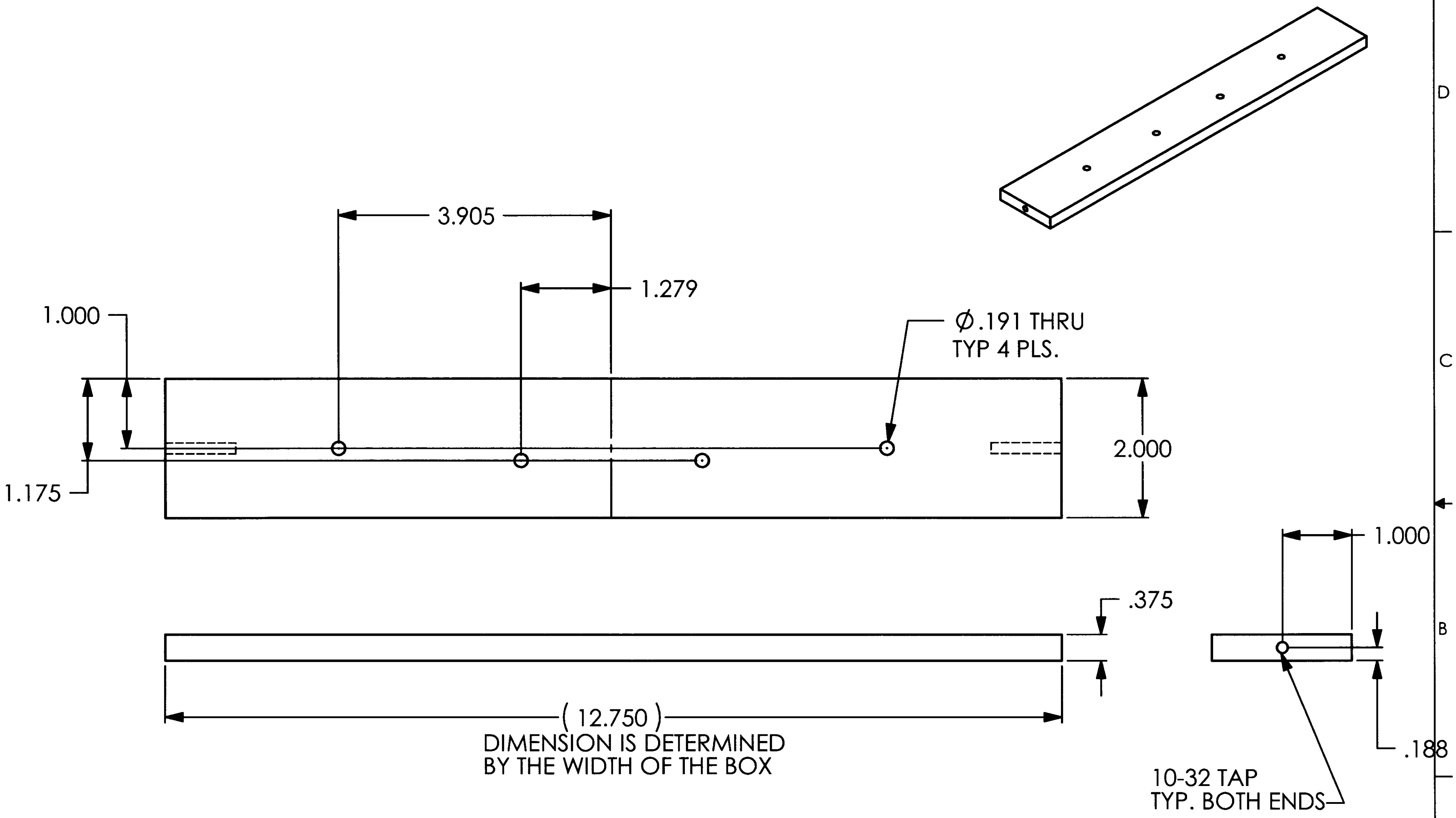

UNLESS OTHERWISE SPECIFIED:
DIMENSIONS ARE IN INCHES
TOLERANCES ARE:

| FRACTIONS | DECIMALS | ANGLES |
|---|---|---|
| ±1/64 | .X±.015<br>.XX±.010<br>.XXX±.005 | ±1° |

ALL MACHINED SURFACES 32√
CONCENTRICITY .005 TIR
DEBURR AND BREAK SHARP EDGES

MATERIAL ALUMINUM
FINISH ☒
DO NOT SCALE DRAWING

CAD GENERATED DRAWING,
DO NOT MANUALLY UPDATE

| APPROVALS | DATE |
|---|---|
| DRAWN A. GALLANT | 3/19/2009 |
| CHECKED | |
| RESP ENG | |
| MFG ENG | |
| QUAL ENG | |

Massachusetts Institute of Technology

BAR

SIZE A
DWG. NO.
REV.
SCALE 1:2
CAD FILE:
SHEET 1 OF 1

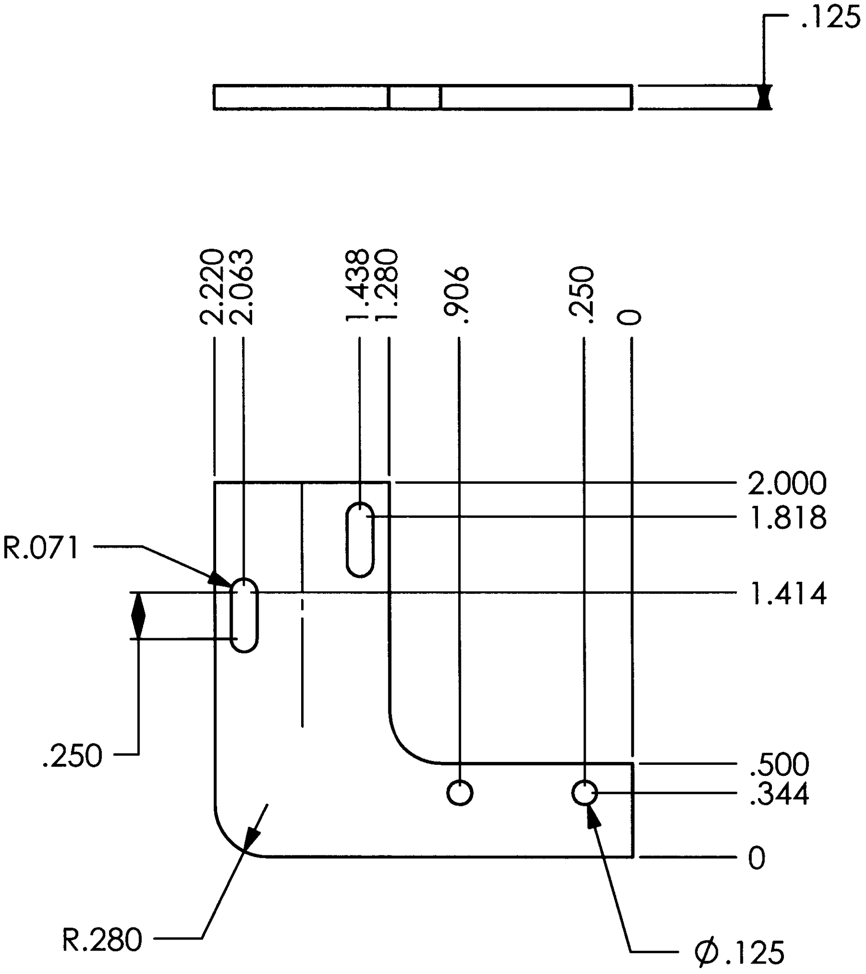

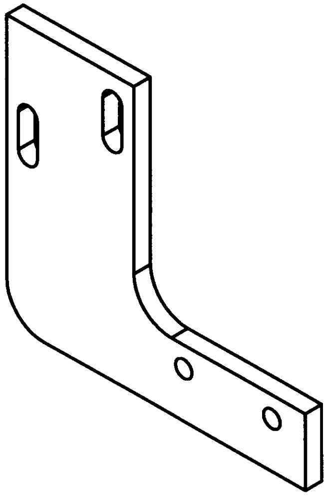

| | | | |
|---|---|---|---|
| UNLESS OTHERWISE SPECIFIED:<br>DIMENSIONS ARE IN INCHES<br>TOLERANCES ARE:<br>FRACTIONS ±1/64 DECIMALS .X±.015 .XX±.010 .XXX±.005 ANGLES ±1°<br>ALL MACHINED SURFACES 32√<br>CONCENTRICITY .005 TIR<br>DEBURR AND BREAK SHARP EDGES | CAD GENERATED DRAWING,<br>DO NOT MANUALLY UPDATE | | Massachusetts Institute of Technology |
| | APPROVALS | DATE | |
| | DRAWN A. GALLANT | 3/19/2009 | SOLENOID MOUNT |
| | CHECKED | | |
| MATERIAL ALUMINUM | RESP ENG | | |
| FINISH ☒ | MFG ENG | | SIZE A DWG. NO. REV. |
| DO NOT SCALE DRAWING | QUAL ENG | | SCALE 1:1 CAD FILE: SHEET 1 OF 1 |